

PERMEABILITIES OF SUBDUCTION ZONE SEDIMENTS AND THEIR EFFECT
ON PORE PRESSURE GENERATION

By

KUSALI R. GAMAGE

A DISSERTATION PRESENTED TO THE GRADUATE SCHOOL
OF THE UNIVERSITY OF FLORIDA IN PARTIAL FULFILLMENT
OF THE REQUIREMENTS FOR THE DEGREE OF
DOCTOR OF PHILOSOPHY

UNIVERSITY OF FLORIDA

2005

Copyright 2005

by

Kusali R. Gamage

To my parents and all my teachers.

ACKNOWLEDGMENTS

I would like to express my sincere gratitude to my advisor, Dr. Elizabeth Screamton, for her continuous support and encouragement throughout my graduate studies. She guided me through the dissertation process, never accepting less than my best efforts. Her technical and editorial advice was essential to the completion of this dissertation and has taught me innumerable lessons and insights on the workings of academic research in general. I cannot thank her enough for bearing my complaints and procrastination with unbelievable patience. My thanks also go to the members of my committee, Drs. David Foster, Jonathan Martin, Louis Motz, and Douglas Smith, who have patiently sat through committee meetings and taken time to understand my work. I also thank them for reading previous drafts of this dissertation and providing many valuable comments that improved the presentation and contents of this dissertation.

Many thanks go to Dr. Barbara Bekins of the USGS, Menlo Park, California, for providing core samples and suggesting working on the Peru permeability measurements and Dr. Ivano Aiello of the Moss Landing Marine Laboratories, California, for providing me with grain size data relating to this research. I am also very grateful to Kevin Hartl for his invaluable technical support, Dr. John Jaeger and William Vienne for helping me with grain size analyses and Dr. Jason Curtis for carbon analyses. My special thanks go to my colleagues Troy Hays, George Kamenov, Jennifer Martin, Victoria Mejia and many friends out in the real world for all their support and encouragement throughout my graduate studies.

Last, but not least, I would like to thank my husband, Sanjaya, for his understanding and love during the past few years. His encouragement was in the end what made this dissertation possible. My parents, Punyasena and Kalyani Gamage, and my brother, Rachita Gamage, receive my deepest gratitude and love for their dedication and the many years of support during my undergraduate studies that provided the foundation for this work.

TABLE OF CONTENTS

	<u>page</u>
ACKNOWLEDGMENTS	iv
LIST OF TABLES	ix
LIST OF FIGURES	x
ABSTRACT	xii
CHAPTER	
1 GENERAL INTRODUCTION	1
Deformation Processes of Subduction Zones.....	2
Role of the Décollement Zone.....	3
Critical Taper Theory	4
Role of Fluid Flow at Convergent Margins.....	6
Evidence for Fluid Flow and Pressures.....	6
Basics of Fluid Flow Related to Subduction Zone	10
Permeability.....	11
Hydrogeologic Modeling.....	12
Statement of Problem	13
2 A COMPARATIVE STUDY OF PERMEABILITY MEASUREMENTS FROM THE SUBDUCTION ZONES OF NORTHERN BARBADOS, COSTA RICA, NANKAI, AND PERU.....	16
Introduction.....	16
Background.....	18
Barbados	18
Costa Rica.....	19
Nankai.....	20
Peru.....	22
Laboratory Permeability Data.....	23
Barbados	24
Nankai and Peru	25
Costa Rica.....	26
Permeability-Porosity Relationship	27
Description of Statistical Methods.....	27

Results.....	28
Effects of Depositional Environment	29
Effects of Grain Size	34
Effects of Structural Domain.....	38
Discussion.....	40
Conclusions.....	42
3 CHARACTERIZATION OF EXCESS PORE PRESSURES AT THE TOE OF THE NANKAI ACCRETIONARY COMPLEX, OCEAN DRILLING PROGRAM SITES 1173, 1174, AND 808: RESULTS OF ONE- DIMENSIONAL MODELING	44
Introduction.....	44
Background.....	45
Geologic Setting	45
Previous Hydrologic Studies	48
Laboratory Permeability Measurements.....	52
Modeling Methods.....	55
Theoretical Background	55
Model Implementation	58
Model Dimensions, Boundary Conditions, and Initial Conditions	59
Sedimentation and Prism Thickening Rates.....	61
Results.....	62
Model Results.....	62
Sensitivity to Bulk Permeability.....	65
Sensitivity to Lateral Stress	67
Sensitivity to a Low-Permeability Barrier.....	70
Implications	73
Conclusions.....	74
4 EVOLUTION OF HIGH PORE PRESSURES AND IMPLICATIONS FOR EPISODIC FLUID FLOW AT THE NORTHERN BARBADOS ACCRETIONARY COMPLEX.....	76
Introduction.....	76
Background.....	79
Fluid Flow and Pore Pressures	82
Hydrofractures	85
Modeling Methods.....	86
Model Implementation	86
Model Equations.....	87
Model Dimensions, Boundary Conditions, and Initial Conditions.....	88
Sedimentation and Loading Rates	91
Results and Discussion	93
Conclusions.....	102
5 SUMMARY AND CONCLUSIONS	104

APPENDIX: LISTING OF PERMEABILITY, POROSITY, GRAIN SIZE DATA WITH REFERENCES USED IN THIS STUDY	107
LIST OF REFERENCES	121
BIOGRAPHICAL SKETCH	133

LIST OF TABLES

<u>Table</u>	<u>page</u>
2-1 Log linear permeability-porosity relationships predicted for varying lithologies at Barbados, Costa Rica, Nankai and Peru.....	33
2-1 Permeability-porosity relationships based on grain size analyses.	35
3-1 A summary of laboratory measured permeabilities for samples from ODP Leg 190 Sites 1173 and 1174.	53
3-2 Fluid and solid matrix properties used for numerical simulations.	61
3-3 Summary of sedimentation rates calculated from biostratigraphy at Sites 1173, 1174 and 808 and prism thickening rates calculated from prism geometry and convergence rate.....	62
3-4 Summary of simulation runs at Site 1174 and 808.	64
4-1 Fluid and solid matrix properties used for numerical simulations.	91
4-2 Summary of sedimentation rates calculated from biostratigraphy at Sites 1173, 1174 and 808.	92
4-3 Summary of simulation runs with the estimated values of maximum λ^*	99
A-1 Listing of permeability, porosity, grain size data with references used in this study.	108

LIST OF FIGURES

<u>Figure</u>	<u>page</u>
1-1 Diagram of accretionary prism and the processes of frontal accretion and underplating.	3
1-2 Schematic of an ideal coulomb wedge.....	5
2-1 Map of large-scale regional setting location of the drill sites at the Barbados accretionary complex.	18
2-2 Map showing location of ODP drilling along the Costa Rica subduction zone.	20
2-3 Location map of ODP Leg 190 and previous ODP/DSDP drill sites in the Nankai Trough.	21
2-4 Map showing general locations of drill sites occupied during ODP Legs 138 and 112 at Peru subduction zone.	23
2-5 Plot of laboratory derived permeability measurements from Barbados, Costa Rica, Nankai, and Peru subduction zones.	29
2-6 Permeabilities classified based on depositional environment and location.	33
2-7 Permeabilities classified based on grain size distribution.	37
2-8 Permeabilities classified based on structural domain.	39
3-1 Location map of the study area in the Nankai accretionary complex and sites used for this study.	46
3-2 Schematic interpretation of the Muroto Transect showing tectonic domains and location of Leg 190 drill sites used in this study.....	47
3-3 Porosity profiles of Sites 808, 1174, and 1173.	50
3-4 Permeability data measured for samples from ODP Leg 190.	54
3-5 Simulated porosity and λ^* profiles for base run at Site 1173.....	65
3-6 Simulated porosity and λ^* profiles with varying bulk permeability at Sites 1174 and 808.	66

3-7	Simulated porosity and λ^* profiles with added lateral stress at Sites 1174 and 808.	68
3-8	Simulated porosity and λ^* profiles with added low-permeability barrier at Sites 1174 and 808.	71
4-1	Location map and cross-section of the Barbados accretionary complex.	80
4-2	Grid and boundary conditions for the prism growth/flow model.....	90
4-3	Simulated λ^* values for base run at 0.6, 1.3, 2.0, and 2.7 million years.	97
4-4	Estimated λ^* values in the décollement at 0.6, 1.3, 2.0 and 2.7 million years of prism growth for all simulations.	101

Abstract of Dissertation Presented to the Graduate School
of the University of Florida in Partial Fulfillment of the
Requirements for the Degree of Doctor of Philosophy

**PERMEABILITIES OF SUBDUCTION ZONE SEDIMENTS AND THEIR EFFECT
ON PORE PRESSURE GENERATION**

By

Kusali R. Gamage

December 2005

Chair: Elizabeth Screamton
Major Department: Geological Sciences

Permeability is a fundamental sediment property influencing fluid flow, hence fluid pressures in the subsurface. Because elevated fluid pore pressures play a critical role in the development of accretionary complexes, including the development of the décollement zone, it is important to simulate pore pressures based on a systematic relationship of permeability and porosity. Based on laboratory permeability measurements of Northern Barbados, Costa Rica, Nankai and Peru subduction zones sediments, a high correlation between permeability and porosity was found for argillaceous sediments while little correlation was found for carbonate dominant sediments. Classification based on location and grain size distribution provided greater correlation between permeability and porosity than the depositional environment of the sediment alone. In the second part of the research, a one-dimensional loading and fluid flow model near the toe of the Nankai subduction zone was used to examine the effects of lower bulk permeability (sensitivity to a permeability-porosity relationship), lateral stress

in the prism, and addition of a low-permeability barrier to the décollement. The results predicted significant increase in pore pressures below the décollement zone with lower bulk permeability, or when a low-permeability barrier is added at the décollement. Both simulations with lateral stress and a low-permeability barrier at the décollement resulted in sharp increases in porosity at the décollement, similar to that observed in measured porosities. In addition, these two scenarios predict maximum excess pore pressure ratios at the décollement suggesting that either of these factors would contribute to stable sliding along the décollement. In the third part of the research, results from a two-dimensional prism growth and flow model indicate pore pressures close to lithostatic pressures at the décollement when décollement was given the same permeability as the surrounding sediments. However, these pore pressures were unable to reach lithostatic pressures thus not allowing horizontal hydrofracture in the décollement zone. Addition of vertical hydrofractures in the underthrust sediments did not increase pore pressures to lithostatic pressures in the décollement. When a bulk permeability-vertical stress relationship was assigned to the décollement, pore pressures reach values close to lithostatic pressures, suggesting that high pore pressures can be sustained at the base of the prism while fluid is expelled at the toe of the complex.

CHAPTER 1 GENERAL INTRODUCTION

Examining the fluid flow of the deep hydrosphere is extremely important because fluid flow alters the physical and chemical properties of the Earth's crust, which in turn affects the ocean and the atmospheric chemistry that is vital for human existence (COMPLEX, 1999). At active plate margins, fluid flow can influence movement along faults and thus the nature of the earthquake cycle. Several research projects have recently been focused on studying fluid flow along active plate margins. The Ocean Drilling Program (ODP) has contributed valuable information on fluid behavior by sampling the sediments and oceanic crust at shallow ends of the subduction zones.

At convergent margins, the incoming sediments and lithosphere are fed into the subduction factory where processes such as compaction and dewatering, diagenesis, dehydration, metamorphism, melting, melt migration and mantle convection result in hazardous seismicity, explosive volcanism as well as the formation of ore deposits and new continental crust (Moore, 1998). A large number of the world's greatest earthquakes are associated with subduction zones. A small portion of the plate contact, known as the seismogenic zone, is responsible for generating these large earthquakes. Understanding the processes of the seismogenic zone provides valuable information on earthquake generation, but requires studying many aspects of geology.

Shallowly dipping subduction zones provide a large fault surface that is accessible to study by allowing sampling of the incoming sediments. In such localities, accretionary complexes are formed if sediments are scraped off the subducting oceanic plate and

accreted on the upper plate. Many accretionary complexes grow above sea level and even until they form mountain belts. One such example of a partially exposed accretionary complex is the Barbados Island located in the Caribbean. Examples of ancient complexes include the Shimanto Belt of southwest Japan, the Franciscan complex of California, and the Kodiak accretionary complex of Alaska.

Even though more than half of the world's convergent plate boundaries are forming accretionary prisms (von Huene and Scholl, 1991) there are margins where all of the sediments riding on the oceanic plate are underthrust beneath the upper plate of the subduction zone (e.g., Costa Rica). Particularly in the western Pacific, trenches lack accretionary sediments because the terrigenous sediment supply reaching the trench floor is insufficient to accrete (von Huene and Scholl, 1991). Thus, typically non-accreting margins are bordered by sediment-starved trenches such as the Mariana and Tonga.

Deformation Processes of Subduction Zones

At convergent boundaries, sediments can be either offscraped as a series of thrust sheets at the frontal edge of the accretionary prism or underthrust with the subduction plate to great depths (Moore, 1989). Accreted sediments form a series of imbricate thrust sheets that extend from the surface to the basal detachment fault or the décollement. Accretionary prisms grow volumetrically by two main processes (Figure 1-1). On the surface, accretionary prisms grow by frontal accretion while on the subsurface they grow by underplating (von Huene and Scholl, 1991). According to von Huene and Scholl (1991) the division of these two processes refers to the seaward position of the margin's resistive rock structure (backstop), which also acts as the mechanical backstop of the seaward part of the margin. Frontal accretion takes place in front of the backstop by offscraping the upper part of the oceanic sediment while the lower parts of the oceanic

sediment are underthrust. Sediment subducted beneath the backstop is subsequently accreted by underplating or transported to greater depths (von Huene and Scholl, 1991). During frontal accretion, thrust slices will detach the upper part of the incoming sediments. When sediments move from the oceanic plate to the accretionary prism, the state of stress changes from gravitational to that of a thrust belt (Moore, 1989). On the oceanic plate the maximum principal stress is oriented vertically and as sediments get accreted the maximum principal stress gradually inclines (Davis et al., 1983). With the stacking and upward rotation of these thrust slices, the accreted material will thicken and shorten (von Huene and Scholl, 1991).

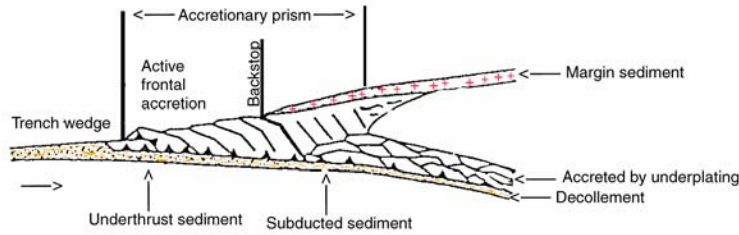


Figure 1-1. Diagram of accretionary prism and the processes of frontal accretion and underplating (modified from von Huene and Scholl, 1991).

Role of the Décollement Zone

The décollement zone is the principal boundary that separates the upper and lower converging plates (von Huene and Scholl, 1991). The sediments above the décollement are highly deformed while the sediments below remain coherent (Moore et al., 1982). Change in structural style across the décollement suggests that this zone marks a major shift in the orientation of the stresses (Moore, 1989). This has been supported by the presence of extensional veins observed in the underplated sediments that are interpreted as hydrofractures with near vertical orientation of the maximum principal stress (Fisher and Byrne, 1987). An important question that has not yet been answered is how the

décollement initiates. It has been proposed by many studies that elevated fluid pressures are necessary for the initiation and sliding of the décollement (Davis et al., 1983; Westbrook and Smith, 1983). If the décollement steps down within a packet of subducted sediments, then the material of the lower plate can be transferred to the upper plate, effecting underplating and volumetric growth of the prism (von Huene and Scholl, 1991). Furthermore, if the décollement moves upward, accreted material will be transferred to the lower plate promoting subduction erosion (Charlton, 1988).

At some accretionary prisms such as Cascadia, southern Chile and eastern Alaska, the décollement lies at the base of the incoming sedimentary section suggesting that all incoming sediments are frontally accreted (von Huene and Scholl, 1991). Furthermore, Davis and Hyndman (1989) inferred that large accretionary prisms such as Barbados or the Makran prism of southern Pakistan have achieved their exceptional size due to efficient offscraping favored by slow convergence and thick incoming sediments, although the décollement is located well above the igneous basement.

Critical Taper Theory

The critical taper theory has been widely used to explain the shape of accretionary prisms as well as to estimate excess pore pressures. Davis et al. (1983) used Coulomb failure theory to demonstrate that homogeneous wedges reach a stable critical taper that remains constant as long as the controlling parameters do not change. Once it reaches the maximum thickening and shortening, the accretionary prism will maintain its taper by adding material either by underplating or by new thrust faults that cut the accretionary prism at shallow angles, which are known as the out of sequence thrusts (von Huene and Scholl, 1991). The critical taper is defined by $\alpha + \beta$, where α and β are the topographic

slope and the décollement dip respectively (Figure 1-2). The parameters that control the taper angle are the internal (ϕ) and basal friction angles (ϕ_b) and the pore fluid pressure ratios of the wedge (λ) and the base (λ_b). The λ is given by

$$\lambda = \frac{P_f - P_{seafloor}}{P_{litho} - P_{seafloor}}$$

where P_f is the pore pressure in the sediments, $P_{seafloor}$ is that pressure in the water column above the seafloor, and P_{litho} is the total pressure of the overlying water column and sediments. The internal (μ) and basal friction (μ_b) coefficients are given by

$$\mu = \tan\phi \text{ and } \mu_b = \tan\phi_b$$

According to critical wedge theory (Davis et al., 1983; Dahlen, 1984) the wedge taper gives an indication of either the material properties of the wedge or the friction at the base of the wedge. A large critical angle indicates either a weak material, which needs to deform before stable sliding could occur, or high basal friction (Davis et al., 1983). In contrast a small critical angle indicates either a strong material, which need not deform for stable sliding to occur, or very little basal friction (Davis et al., 1983).

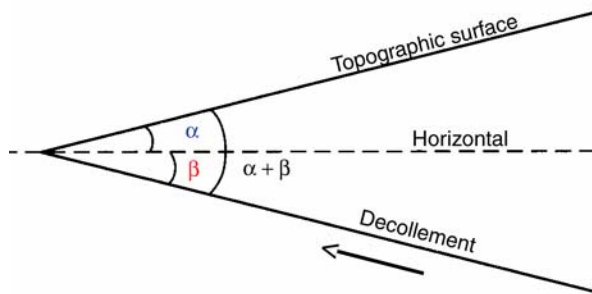


Figure 1-2. Schematic of an ideal coulomb wedge (modified from Hatcher, 1995).

Using the concepts presented by Davis et al. (1983), Bernstein-Taylor et al. (1992) interpreted that a large change in basal friction could result from a change in fluid

pressure from an overpressured décollement zone to hydrostatic fluid pressure beneath the toe. If the material is different from the toe to arcward, then the material at the toe can be relatively weak and can deform until a large critical taper is achieved. Arcward of the toe, stronger material need not deform internally for stable sliding and thus, will have a small critical angle (Davis et al., 1983).

Role of Fluid Flow at Convergent Margins

Approximately 40% of the sediment section entering the world's subduction zones is composed of water in pore spaces (Moore et al., 2001). Fluid flow at accretionary complexes is due to a number of different driving forces, including gravitational loading, tectonic compression, fluid density gradients, and dehydration reactions. During both gravitational loading and tectonic compression, sediments will generally compact. However, if the rate of loading or compression is sufficiently high, then fluids cannot escape fast enough, which causes pore pressures to rise. These localized excess pore pressures generate a pressure gradient and hence fluid flow. Density variations can result from differences in solute concentrations or due to the introduction of heat sources. Mineral dehydration is another method where fluids are released during the reaction, hence increasing the fluid pore pressures. A common example of a dehydration reaction found in accretionary complexes is the smectite to illite transition.

Evidence for Fluid Flow and Pressures

At many active accretionary prisms (e.g., Japan, Barbados, Oregon-Washington, Marianas) evidence for fluid expulsion has been observed, including the presence of biological communities, heat flow and geochemical anomalies, and mud volcanoes and diapirs (Peacock, 1990). Each of the evidence types is summarized in the following paragraphs.

One of the most interesting indicators of fluid expulsion from accretionary prisms is the presence of biological communities (Le Pichon et al., 1987). Studies have shown that the range of biomass found in colonies is related to the fluid chemistry and flow rate (Sibuet et al., 1990). Thus, studying the nature and distribution of the colonies provide valuable information on qualitative fluid flow. Such examples of ancient seep communities have been identified in accretionary prisms. These biological communities were formed as concentrations of macrofossils in deepwater rocks (Moore and Vrolijk, 1992). If flow continues at seeps for a longer time the biomass can grow beyond the limits of the calcite compensation depth (depth below which calcite is dissolved in the deep-sea) developing into reef like structures that eventually could transform into hydrocarbon reservoirs (Hovland, 1990).

Fluid transport has been inferred from fluid inclusions from veins that show anomalously high temperatures at shallow depths in ancient accretionary complexes (Vrolijk et al., 1988). At modern accretionary complexes, the age of the oceanic crust can be used to predict conductive heat flux and therefore, anomalies from the conductive heat flux that might be due to fluid flow can be identified. The best evidence for deeply derived warm fluids comes from the Northern Barbados accretionary prism (Davis and Hussong, 1984). It is interpreted that the observed heat flow anomalies were caused by advection of heat during channelized fluid flow along faults (Moore and Vrolijk, 1992). At the Barbados accretionary complex, both borehole temperatures and marine heat flow measurements demonstrate thermal gradients approximately twice that expected for the age of the subducting crust (Fisher and Hounslow, 1990). Heat flow values that are lower than predicted by conductive cooling of the oceanic crust have been reported

offshore of Peru (Langseth and Silver, 1996). One possible explanation for this low heat flow is the rapid sedimentation at Peru, which may prevent equilibrium (Moore and Silver, 2004). Similarly, heat flow measurements at Cocos Plate off the Nicoya Peninsula have revealed significantly low heat flow values (Langseth and Silver, 1996). It has been suggested that hydrothermal cooling of the oceanic basement occurs from the flow of seawater into the upper crust of the subducting plate (Langseth and Silver, 1996).

Furthermore, evidence for possible fluid migration comes from observed low chloride anomalies (concentrations less than seawater), found in many modern prism sediments (Kastner et al., 1991). One of the widely used explanations for the observed low chloride anomalies is the dehydration reaction of smectite to illite. Smectite is a common and abundant type of clay found in subduction zones (Moore and Vrolijk, 1992). The dehydration of smectite to illite is a kinetic reaction that depends on temperature and time (Elliott et al., 1991). The reaction takes place in temperatures above 60°C and the amount of water released during the reaction is estimated to be 20% by weight (Bekins et al., 1995). Smectite is replaced by fluid plus illite, which has greater volume than smectite, thus resulting in an increase in pore pressures (Bekins et al., 1995). At Barbados, low-chloride anomalies were observed along the décollement (Kastner et al., 1993) and it is inferred that pore fluids generated from smectite dehydration migrate toward the toe of the prism mainly through faults or fractures lowering the chloride concentration at the toe of the prism (Bekins et al., 1995). A broad low chloride anomaly was also observed above and below the décollement at the Nankai accretionary complex. Because the smectite contents at the Nankai sites are low, it has been inferred that freshening of pore fluids may be related to the in situ dehydration

caused by high temperature regimes (Brown et al., 2001). The high temperature regimes are believed to be related to the fossil spreading ridge (Kinan Seamount) that ceased spreading ~ 15 Ma ago located on the Philippine Sea Plate (Shipboard Scientific Party, 2001).

Mud volcanoes and diapirs are also common features found in accretionary complexes. They form due to increased pressure at depth and transport overpressured mud to the surface. In areas where serpentine diapirs or volcanoes are present, it requires fluids to hydrate basalt in order to form serpentine and these structures become conduits of fluid flow from depth (Fryer et al., 1990). During diapirism and mud volcanism rock sequences are disrupted and mélanges are formed (Brown and Westbrook, 1988). Mud diapirs and mud volcanoes are often observed along thrust faults, suggesting thrusting as a mechanism that triggers mud diapirism (Behrmann, 1992).

All the evidence for fluid flow from accretionary complexes implies fluid pressure gradients in excess of hydrostatic because pressures gradients drive fluid flow. Indirect evidence for elevated fluid pressures includes the presence of extensional veins (Moore and Vrolijk, 1992). Crack-seal textures in veins indicate repeated pulses of high fluid pressure (Vrolijk, 1987; Fisher and Byrne, 1990). Repeated events of vein growth suggest that fluid pressure evolve throughout the growth of the accretionary complex (Labaume et al., 1997). Fluid pressure in accretionary prisms can vary from hydrostatic (equivalent to the weight of the overlying column of water) to nearly lithostatic (equivalent to the weight of the overlying column of sediments). Variation in fluid pressures from hydrostatic to lithostatic has been observed in wells at the eastern Aleutian Trench where the fluid pressures are at hydrostatic at 2-3 km from the surface

and increasing to more than 80% of lithostatic pressures at total depth (Moore and Vrolijk, 1992).

Basics of Fluid Flow Related to Subduction Zone

Although sediments found in accretionary prisms are highly deformed during subduction, it is assumed that the high density and interconnectedness of the fractures in accretionary prisms approximate Darcian flow (Moore and Vrolijk, 1992). The fluid produced during the accretionary process can be evaluated using the two principles that govern fluid flow in the subsurface. They are the principle of conservation of mass and Darcy's law. The principle of conservation of mass states that for an arbitrary control volume, the rate of mass accumulation within the volume plus the net mass flux out of the volume must equal the rate of mass generation within the volume (Bird et. al., 1960). If we consider a very small volume of the aquifer known as a control volume, we can approximate the flow through the matrix using Darcy's law. The most basic form of Darcy's law states

$$Q/A = -K \frac{dh}{dl}$$

where Q/A is flow per area or linear velocity [LT^{-1}], K is hydraulic conductivity [LT^{-1}], and dh/dl is hydraulic gradient. The hydraulic conductivity (K), which is a proportionality constant, represents both properties of the fluid and the porous media. It is given by

$$K = k\rho g / \mu$$

where k is intrinsic permeability [L^2], which is representative of the properties of the porous medium, ρ is the fluid density [ML^{-3}], μ is the fluid viscosity [$L^{-1} T^{-1}$] and g is the gravitational constant [$L T^{-2}$]. Intrinsic permeability depends on variables such as grain

size, sorting, and roundness of the sediment through which fluid flowing. Hereafter, intrinsic permeability will be referred to as permeability.

Permeability

Sediment permeability is the most important factor that controls pore pressures as permeability can vary by many orders of magnitude (e.g., Bruckmann et al., 1997; Saffer and Bekins, 1998). Therefore, the use of a systematic relationship between porosity and permeability is valuable for approximating the permeability structure in an accretionary wedge fluid flow model (Saffer and Bekins, 1998). Processes in subduction zones such as loading, compaction and cementation of sediments lead to reductions in permeability. When permeability is reduced and reaches some critical value, rocks can no longer transmit significant amounts of fluid, but new permeability can be created in the form of a fracture or a fault. If fractures are formed then they can significantly affect the permeability of the accretionary complex and, thus, large-scale field measurements of permeability would be more appropriate than core scale permeability measurements to determine large-scale fluid flow (Moore and Vrolijk, 1992). Unfortunately only a few large-scale field measurements of permeability have been made in accretionary settings. These include shipboard packer tests and submersible-based tests conducted at a sealed borehole at the Oregon accretionary complex (Screaton et al., 1995) and shipboard packer tests (Fisher and Zwart, 1996) and submersible slug tests and discharge tests (Screaton et al., 1997) in the décollement of the Barbados accretionary complex. Because of difficulties in conducting large-scale field measurements, permeability measurements are primarily from core samples that are retrieved from the frontal part or shallow depths of the accretionary complex. Even though these core sample measurements do not represent the large-scale variations in permeability due to faults, they provide valuable estimates

for the matrix permeability that is critical in approximating permeability structures in the accretionary complex for modeling studies.

Hydrogeologic Modeling

Mathematical models used in hydrologic modeling are derived from the governing principles of fluid flow and specifications such as formation geometry, boundary conditions and initial conditions. These models help quantify conceptual models of sub-seafloor hydrogeologic flow system. These models can be extremely useful and cost effective in providing possible explanations for known or hypothesized conditions. They can also be used to assess whether or not a conceptual model is feasible. As a starting point, with limited data it is best to use one or two-dimensional analytical solutions derived from simple well-defined boundary problems (Anderson and Woessner, 1992). However, in sub-seafloor settings, numerical models are often necessary in order to account for parameters such as complex geometry, variable density fluid flow, and variations in heat flow.

Due to limited access to convergent margins, models are essential for integrating the field observations with laboratory results. It has also been recognized that numerical models are required in order to extend observations made at shallow parts of the subduction system to greater depths such to the seismogenic zone (COMPLEX, 1999). Most previous modeling studies have focused on coupled compaction-fluid flow and diffusion-advection models of pore fluid chemistry and heat for Barbados, Nankai and Cascadia accretionary prisms (e.g., Bekins et al., 1995; Saffer and Bekins, 2002; Screamton and Ge, 1997). However, recent data collection allows significantly improved characterization of permeability, which is a major component that affects modeled fluid pressures in accretionary complexes. Furthermore, previous modeling studies at Nankai

have largely focused on estimating pore pressures with little focus on examining the causes of excess pore pressures (Le Pichon and Henry, 1992; Screamton et al., 2002; Saffer, 2003). At Barbados, modeling studies were focused on pore pressure generation either at the toe of prism (Henry and Wang, 1991; Shi and Wang, 1994; Stauffer and Bekins, 2001) or in a steady-state approach instead of examining pore pressure generation through the subduction process.

Statement of Problem

The objective of this investigation was to expand the knowledge of fluid flow and the development of pore pressures based on both laboratory measured permeability values and numerical models at selected accretionary complexes. This study benefits our current understanding of fluid flow in accretionary complexes in several ways. One of the primary benefits of this research is the contribution and synthesis of permeability measurement of subduction zone sediments, which provides new insight to flow simulations in convergent margins. This study also provides valuable information on fluid flow paths, areas of excess pore pressures, degree of importance of lithology and sediment thickness in fluid flow, the initiation of décollement, and factors that contribute to the initiation of the décollement. These results further provide valuable information for future drilling projects such as the Seismogenic Zone Experiment (SEIZE) that is focused on understanding the relationship between earthquakes, deformation, and fluid flow. The following were the specific objectives of this study:

- To synthesize permeability data and predict permeability-porosity relationships at four major convergent margins. The four locations are the Northern Barbados, Costa Rica, Nankai and Peru subduction zones, which represent a variety of marine sediments.
- To investigate the effects and magnitudes of parameters such as bulk permeability, lateral stress, and the presence of a low-permeability barrier at the décollement on

the generation of excess pore pressures at the toe of the Nankai accretionary complex.

- To investigate the evolution of pore pressures and implications for episodic fluid flow at the Barbados accretionary complex using a two-dimensional growth and flow model.

The following chapters include detailed methodology and discussions of the results of the proposed research. Chapter 2 is titled “A comparative study of permeability measurements from the subduction zones of northern Barbados, Costa Rica, Nankai and Peru” and a modified version of this chapter will be submitted for publication to Marine Geology. This chapter is a contribution to the permeability data of marine sediments at subduction zones. The major results of this chapter include relationships among permeability and porosity for different types of marine sediments. The constraints provided by these relationships will allow realistic estimation of fluid flow and pore pressures in marine settings. Furthermore, the laboratory measured permeability data from Nankai and Peru contributes to the general knowledge of marine sediments. The permeability data of this work has been published as two data reports (Gamage and Screamton, 2003; Gamage et al., 2005). A modified version of Chapter 3, titled “Characterization of excess pore pressures at the toe of the Nankai accretionary complex, Ocean Drilling Program sites 1173, 1174, and 808: Results of one-dimensional modeling” has been accepted for publication by the Journal of Geophysical Research, authored by Gamage and Screamton. This chapter contributes to the understanding of the development of pore pressure at the toe of the Nankai accretionary complex. This study was based a one-dimensional model and uses the permeability-porosity relationship developed for Nankai hemipelagic sediments in the previous study. The sensitivity of pore pressures to bulk-permeability, lateral stresses within the prism, and a low-

permeability barrier at the décollement was also tested. The results of this simplified model assess parameters that significantly affect pore pressures in subduction zones. Furthermore, the results of this study provide insight on the initiation of the décollement zone. Chapter 4 contributes to the understanding of the development of pore pressures through space and time at the Barbados accretionary complex. This study is based on a two-dimensional model that allows tracing the development of pore pressures as sediments subduct beneath the prism. The model allows examination of the effect of hydrofracture and a décollement with varying permeability based on a relationship of bulk permeability -vertical effective stress. Results indicate the spatial and temporal variations of excess pore pressures and provide insight to possible mechanics for episodic fluid flow. This chapter will be adapted for submittal to the Earth Planetary Science Letters. Chapter 5 summarizes the principal findings of chapters 2 through 4.

CHAPTER 2

A COMPARATIVE STUDY OF PERMEABILITY MEASUREMENTS FROM THE SUBDUCTION ZONES OF NORTHERN BARBADOS, COSTA RICA, NANKAI, AND PERU

Introduction

Marine sediments have been widely studied for their physical properties both in academic and industrial research. With the introduction of the Deep Sea Drilling Project (DSDP) and the Ocean Drilling Program (ODP), a new level of understanding has been added to the knowledge of marine sediments during the past few decades. Physical properties of submarine sediments have been studied largely through recovered cores, down-hole logging, and also by in situ instrumentation. Permeability is one such physical property that has been closely studied for its importance in fluid flow and pore pressures in the subsurface. Previous studies based on permeability measurements of marine sediments have suggested that correlation between permeability and porosity could provide insight to a large range of sediments in nature (Bryant, 2002).

Investigations based on numerical modeling have shown that permeability is a crucial parameter in accretionary complex hydrology (e.g., Bekins et al., 1995; Bruckmann et al., 1997; Saffer and Bekins, 1998). According to Saffer and Bekins (1998) sediment permeability is the most important factor that controls modeled pore pressures because it can vary by several orders of magnitude. Thus, using a systematic relationship between porosity and permeability is a powerful way to approximate the permeability structure in an accretionary wedge model (Saffer and Bekins, 1998). Results from modeling studies have shown that pore pressures are highly sensitive to the

permeability-porosity relationship (e.g., Gamage and Screateon, 2006). Prior to the availability of core samples of marine sediments, many studies extrapolated permeabilities from fine-grained terrigenous sediments found on-shore and in many cases these values produced ambiguous results (Bryant et al., 1981). With the availability of more samples, the quantity of permeability data has significantly increased. However, difficulties in laboratory measurements and finding undisturbed cores have limited the amount of permeability measurements representative of different lithologies and structural domains at subduction zones.

The focus of this study is to synthesize available permeability data from four different subduction zones with the aim of predicting permeability-porosity relationships for a number of sediment types found in modern accretionary complexes and to examine what parameters affect the relationship between permeability and porosity. The samples used in this study represent sediments from Northern Barbados, Costa Rica, Nankai, and Peru. Samples representative of the Northern Barbados and Nankai subduction zones mainly consist of fine-grained clays and silts that are commonly grouped as hemipelagics. Samples from Costa Rica consist of both hemipelagics and calcareous oozes while samples from Peru consisted of calcareous oozes and siliceous oozes. Using existing permeability data, permeability-porosity relationships were developed based on depositional environment, grain size distribution and structural domain. These relationships were compared and examined to evaluate the relative importance of each variable.

Background

Barbados

The Barbados accretionary complex is located in the Caribbean where the north American Plate (Figure 2-1) is being subducted beneath the Caribbean Plate at a rate of about 2 cm/yr in an east-west direction (DeMets et al., 1990). Active accretion of sediments at the Barbados accretionary complex takes place at the eastward end of the complex. The complex is partially exposed above sea level at Barbados Island (Figure 2-1). At the location of DSDP and ODP drilling, the incoming sediments are predominantly clay and claystones.

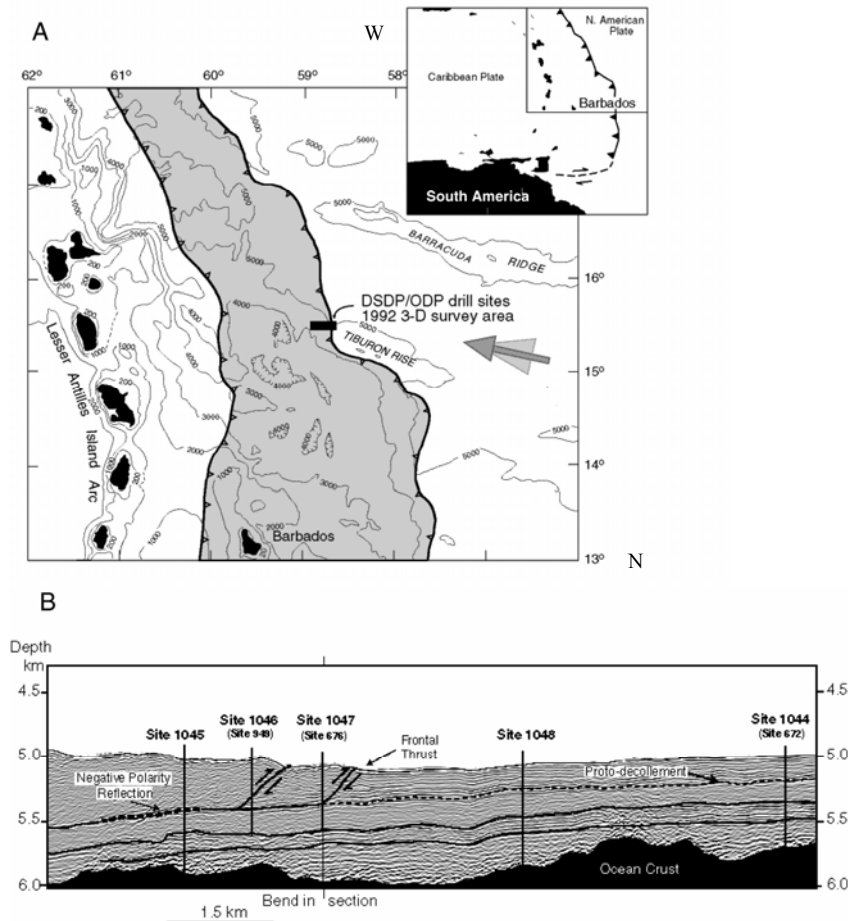


Figure 2-1. A) Map of large-scale regional setting location of the drill sites at the Barbados accretionary complex. B) Cross section from the seismic depth

section extending from west of Site 949 (ODP Leg 156) to Site 672 (ODP Leg 110), (Shipboard Scientific Party, 1998).

This study used core permeability measurements from ODP Leg 156 Sites 948 and 949 and ODP Leg 110 Sites 671, 672 and 676. Site 948 is located 4.5 km west of the deformation front and coincides with the location of Site 671 while Site 949 is located 2 km northeast of Site 948 (Shipley et al., 1997). Site 676 was drilled 0.25 km arcward of the deformation front and Site 672 was drilled 6 km east of the deformation front to provide an undeformed reference site (Masle et al., 1988).

Costa Rica

The Middle American Trench (MAT) is formed by the eastward subduction of the Cocos Plate beneath the Caribbean Plate (Figure 2-2) at a rate of about 8.8 cm/yr (Silver et al., 2000). At Costa Rica the incoming sedimentary sequence is about 380 m thick and consists of approximately 160 m of siliceous hemipelagic sediments overlying about 220 m of pelagic carbonates (Silver et al., 2000). As indicated by drilling on DSDP Legs 67 and 84, this stratigraphy is regionally continuous between the Leg 170 transect and offshore Guatemala (Aubouin and von Huene, 1985; Coulbourn, 1982). During ODP Leg 170, two locations penetrated the décollement zone. Site 1043 is located 0.5 km landward of the trench and Site 1040 is located 1.6 km seaward of the trench. The incoming sediments at Site 1039, which is located at 1.5 km seaward of the deformation front, were also drilled during ODP Leg 170. In a more recent visit to the MAT, ODP Leg 205 drilled Sites 1253, 1254 and 1255 (Figure 2-2). Site 1253 is located 0.2 km seaward of the deformation front while Sites 1254 and 1255 are located coincident with Sites 1040 and 1043, respectively.

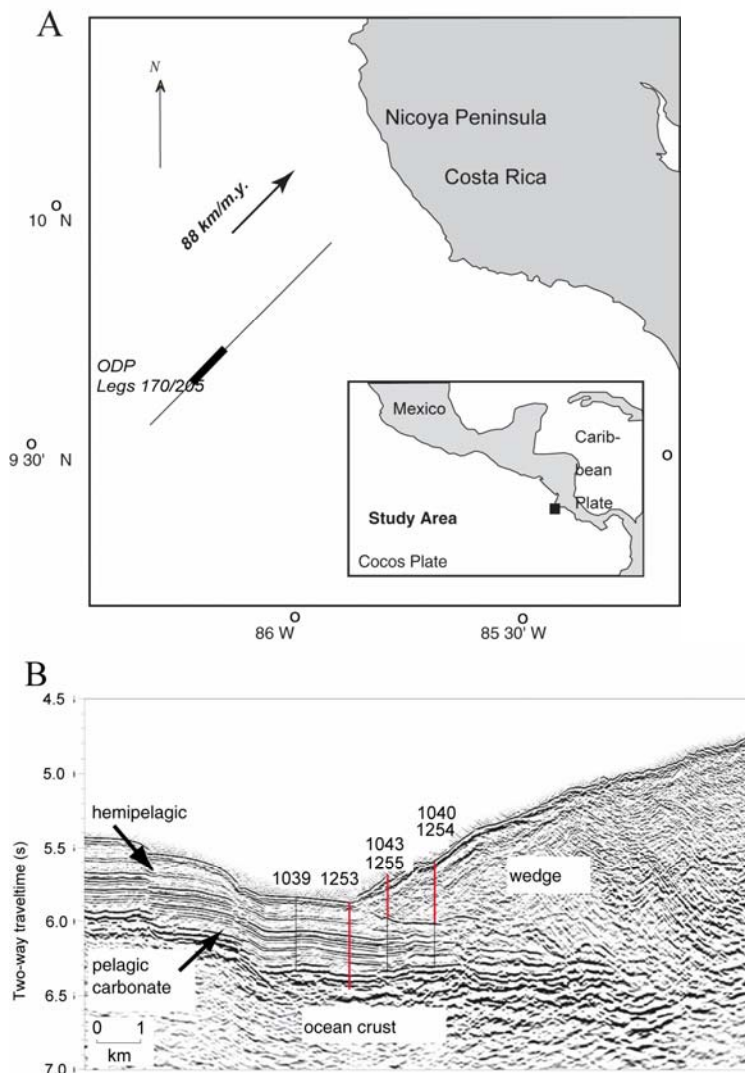


Figure 2-2. A) Map showing location of ODP drilling along the Costa Rica subduction zone. B) Cross-section indicating ODP Leg 170 and 205 drilling sites used for this study (Silver et al., 2000).

Nankai

The Nankai accretionary complex is formed by the subduction of the Shikoku Basin on the Philippine Sea Plate beneath the southwest Japan arc on the Eurasian plate (Figure 2-3) at a rate of about 4 cm/yr (Seno et al., 1993).

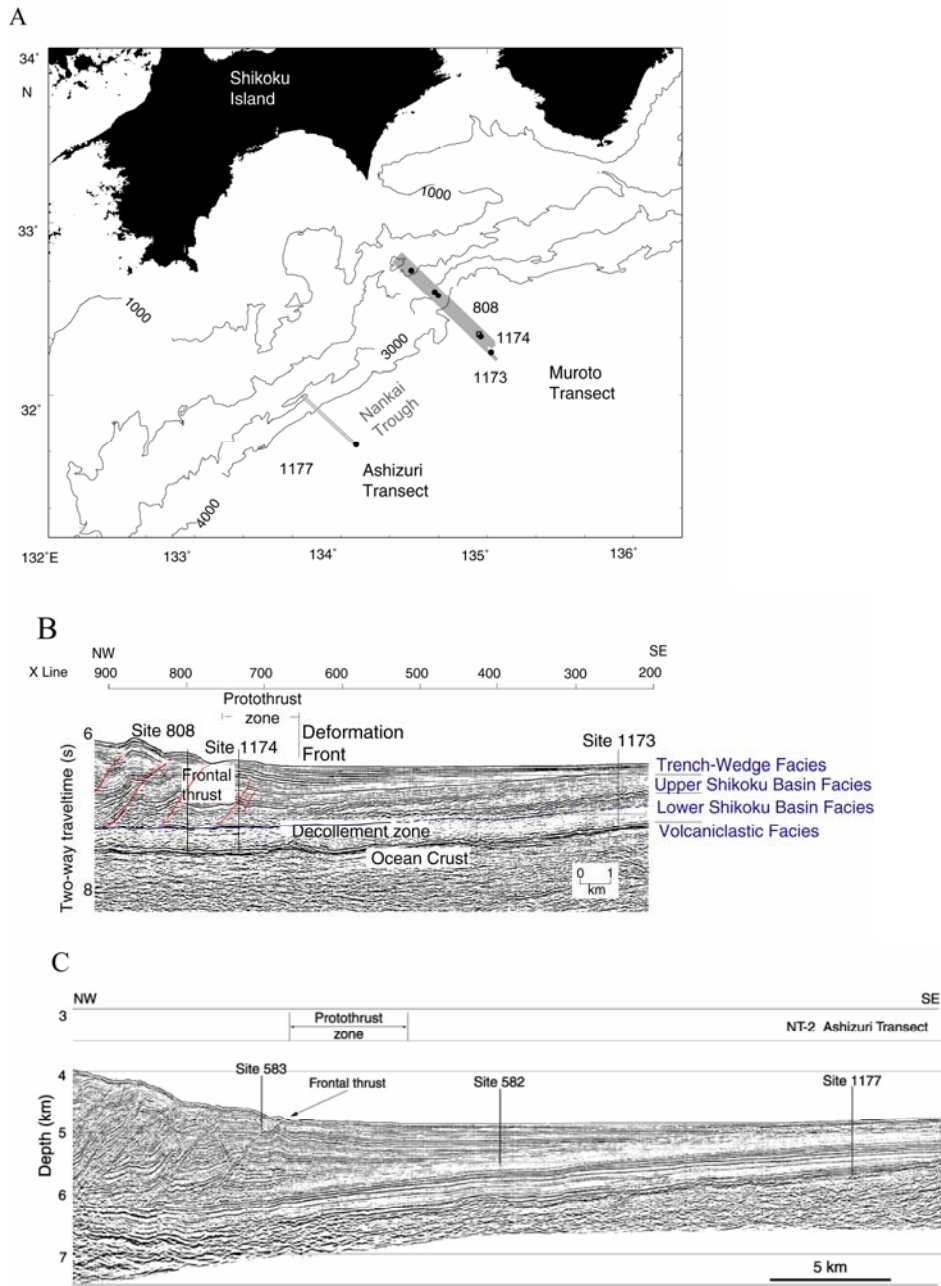


Figure 2-3. A) Location map of ODP Leg 190 (solid circles) and previous ODP/DSDP drill sites (solid squares) in the Nankai Trough. B) Seismic reflection profile through the Muroto Transect reference (Site 1173) and prism toe sites (Site 1174 and 808). C) Seismic reflection profile through Ashizuri Transect showing the reference Site 1177 (Shipboard Scientific Party, 2001).

During ODP Leg 190, Sites 1173 and 1174 were drilled along the Muroto Transect while Site 1177 was drilled approximately 100 km west of Muroto along the Ashizuri Transect (Figure 2-3). Site 1173 was drilled 11 km seaward of the deformation front and

provides an undeformed reference site of the incoming sedimentary sequence (Shipboard Scientific Party, 2001). Site 1174 is located about 1.8 km landward of the deformation front and penetrates the décollement within the proto-thrust zone (Figure 2-3). Site 1177 was drilled approximately 18 km seaward of the deformation front as the reference site for the Ashizuri Transect (Shipboard Scientific Party, 2001). At both Sites 1173 and 1174, the hemipelagic sediments of the upper and lower Shikoku Basin are overlain by the turbidite-rich trench-wedge facies, which was not tested for permeability. At Site 1177, the trench-wedge facies was not cored.

Peru

The Peru accretionary complex is formed by the northeastward subduction at approximately 6.1 cm/yr of the Nazca plate (Hampel, 2002) below the Andean continental margin along the Peru Trench (Figure 2-4). During ODP Leg 201, seven sites were drilled into a wide range of subsurface environments in both open-ocean (Sites 1225, 1226 and 1231) and ocean-margin provinces (Sites 1227 and 1230) of the eastern tropical Pacific Ocean. These subsurface environments include carbonates and siliceous oozes typical of the equatorial Pacific, clays and nannofossil-rich oozes of the Peru Basin, biogenic and terrigenous-rich sediments of the shallow Peru shelf, and clay-rich deepwater sequences of the Peru slope (Shipboard Scientific Party, 2003).

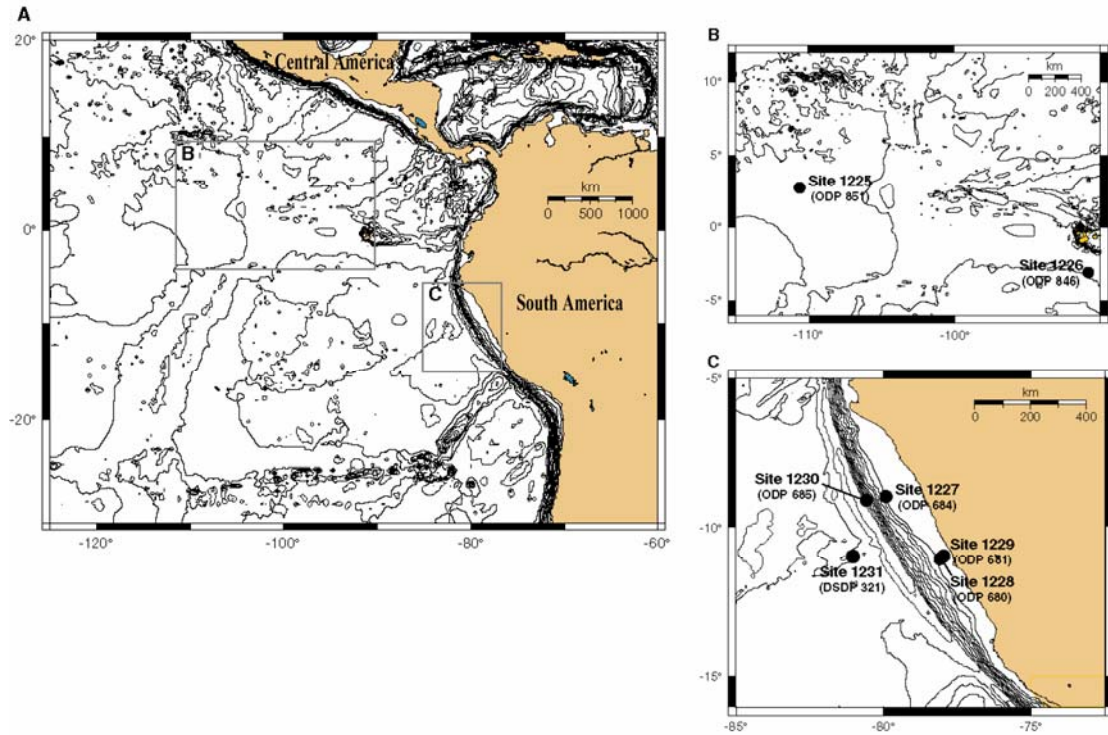


Figure 2-4. A) Map showing general locations of drill sites occupied during ODP Legs 138 (rectangle B) and 112 (rectangle C) at Peru subduction zone. B) Location map of equatorial Pacific primary sites. ODP site designations are in parentheses. C) Location map of Peru margin primary sites. Previous DSDP/ODP site designations are in parentheses (Shipboard Scientific Party, 2003).

Laboratory Permeability Data

Laboratory measured permeability data were provided by several sources for each of the four subduction zones. Two widely used methods for permeability measurements are through direct flow tests (e.g., falling or constant head, constant flow) and consolidation tests. Bryant et al. (1981) cited that results of calculated permeability from consolidation tests are one order of magnitude less than from direct measurements using direct flow methods. Because Bryant et al. (1981) observation was based on an individual direct flow method, it cannot be confirmed that all direct flow methods are incompatible with consolidation tests. However, to be consistent, I limited the permeability data only to those obtained from direct flow methods and excluded data

obtained from consolidation tests. Permeability data that were reported without porosity or void ratio information were also excluded from this study, which examines permeability as a function of porosity. Methods of permeability measurements used in this study are briefly discussed in the following section. Where only hydraulic conductivity was provided, permeability was calculated using (Fetter, 1994)

$$k = K \mu / \rho g \quad (1)$$

where k is intrinsic permeability [L^2], K is hydraulic conductivity [$L T^{-1}$], ρ is fluid density [$M L^{-3}$], g is the gravitational constant [$L T^{-2}$] and μ is the kinematic viscosity [$M L^{-1} T^{-1}$]. Values of fluid density and viscosity were determined based on temperature values reported for the experiment and the salinity of the permeant used. In cases where temperature and/or permeant used were not reported, I assumed a temperature of 25° C and a salinity (for permeant) of 35 kg/m³.

Barbados

Vrolijk et al. (unpubl. data, cited in Zwart et al., 1997) used a sample from ODP Leg 156 Site 948 to measure permeability using a constant-head permeameter at an effective stress of 241 kPa. A sample with 2.5 cm in diameter and about 5 cm high was contained in a triaxial cell. The sample was backpressured at 350 kPa to dissolve any trapped air in the system. The permeant was saline whereas the confining fluid was oil. Bruckmann et al. (1997) measured permeability using three whole round core samples of size 6.2 cm in diameter and about 2 cm high from Leg 156, Site 949. Permeability was measured at individual load steps using low gradient flow tests as described in Olsen et al. (1985). Fresh water was used as both the permeant and the confining fluid. Maltman and others (presented in Zwart et al., 1997) measured permeability of a cylindrical

subsample from Leg 156, Site 949 using low gradient (~ 25 kPa), constant-rate flow tests. The sample was 3.8 cm in diameter and 7.6 cm in height. Two sets of permeability measurements were obtained. During the first set, the effective stress was varied by maintaining a constant confining pressure while varying the pore pressures within the sample. In the second set, effective stress was varied by maintaining a constant pore pressure and varying the confining pressure.

Taylor and Leonard (1990) used the falling head method to measure permeabilities of samples from Leg 110. Samples were backpressured to ensure complete saturation according to Lowe et al. (1964). Permeabilities were obtained at least 24 hr after the application of each new load, yielding a distribution of permeabilities at incremental void ratios. Although both vertical and horizontal permeabilities were measured, I only used the vertical permeability values in this study for consistency with the other samples. Permeabilities were estimated based on hydraulic conductivities reported in Taylor and Leonard (1990).

Nankai and Peru

Gamage and Sereaton (2003), Gamage et al., (2005), and Hays (unpublished data) used the constant flow method, which induces a hydraulic gradient across the sample where the measurements of the pressure difference allow determination of permeability. The samples measured by this method were from ODP Leg 190 Sites 1173, 1174 and 1177 at the Nankai margin and ODP Leg 201 Sites 1225, 1226, 1227, 1230 and 1231 at the Peru margin. Samples had a minimum diameter of 5.84 cm and a height that ranged from ~ 5.84 to 10 cm. Samples were backpressured prior to flow tests. Several consolidation steps were run with the confining fluid pressure used for the consolidation. Permeability was measured at the end of each consolidation step. An idealized solution

of seawater was used as the permeant while deionized water was used as the confining fluid in the cell. Corresponding porosities for estimated permeability were calculated using the change in volume of fluid contained in the cell after each consolidation step.

Masters and Christian (1990) used constant head tests on two Peru samples from ODP Leg 112 Sites 679 and 681. Whole-round samples of 10 cm in height were backpressured to ensure complete saturation. Constant head tests were performed at different hydraulic gradients at varying stress levels. All flow tests were performed in the upward vertical direction. De-aired, filtered seawater with a salinity of 35 kg/m³ was used as the permeant.

Permeability measurements of Nankai sediments conducted by Taylor and Fisher (1993), Byrne et al. (1993), Bourlange et al. (2004) and Adatia and Maltman (2004) were not used in this study due to insufficient data presented and/or inconsistencies found in the methodology. For example, Byrne et al. (1993), Bourlange et al. (2004) and Adatia and Maltman (2004) failed to report porosity/void ratios. Although Bourlange et al. (2004) include amounts of void ratio decrease at certain confining pressures the data did not include an initial porosity to estimate porosities at each effective stress. Taylor and Fisher (1993) used air in permeability testing and also failed to backpressure their samples prior to flow tests. According to Saffer and Bekins (1998) samples that are not reconsolidated could overestimate permeabilities due to fabric expansion, and the use of air in permeability testing would further overestimate the permeability measurements.

Costa Rica

Saffer et al., (2000) performed constant flow tests on samples measuring 6.25 cm in diameter and 1.5 to 1.6 cm in length from ODP Leg 170, Sites 1039 and 1040. Permeabilities were measured at several stages during the sample consolidation to

acquire permeability values at varying void ratios. Multiple flow tests were conducted at each void ratio. McKiernan and Saffer (2005) performed flow through permeability tests on samples that were 2cm tall and 5cm in diameter of ODP Leg Sites 1253, 1254 and 1255. During flow tests, fresh water was pumped into the top of the sample at a constant rate while pressure was maintained at the cell base. The pressure difference was determined by monitoring the pressures at the top of the cell during each flow rate. Varying flow rates were used to produce varying pressure difference across the sample. Distilled, de-aired water was used both as the permeant and confining fluid.

Screaton et al. (2005) used constant flow permeability tests and constant pressure difference tests on samples from ODP Leg 170 Sites 140 and ODP Leg Sites 1253 and 1255. Testing conditions were the same as described in Gamage and Screaton (2003) and Gamage et al. (2005). The only exception to this method was using a constant pressure difference to induce flow through the sample rather than applying a constant flow rate for several of the samples.

Permeability-Porosity Relationship

Bryant et al. (1975) and Neuzil (1994) observed that permeability of argillaceous sediments follows a log-linear relationship with porosity. The log linear relationship is given by

$$\log(k) = \log(k_0) + bn \quad (2)$$

where k_0 is the projected permeability at zero porosity, b is a parameter describing the rate of change of the logarithm of permeability with porosity, and n is the porosity.

Description of Statistical Methods

The coefficient of correlation (R^2) of the regression equation describes the variability of the estimates around the mean. However, it inherits the problem of small

sample size. Thus, in such situations the derived statistics are not necessarily the best indicator of “goodness of fit”. Examination of residuals helps to reaffirm the “goodness of fit” of the regression equation in conjunction with the R^2 value. This examination involved plotting the residuals vs. the dependent variable. If the residuals exhibit a random distribution and have a more or less even split above and below the zero line then it is possible to say that the equation describes the relationship well (Kirkup, 2002)

The other test requires formulating a null hypothesis and an alternate hypothesis, which are then tested using ANOVA and t-statistic. This test helps to access the suitability of the best-fit equation that describes the relationship between the variables (Kirkup, 2002). The hypothesis test utilized in this analysis is a one-tailed ANOVA. In this case the null and alternate hypotheses are,

H_0 : the equation has a zero slope;

H_a : the equation has non-zero slope.

Since the linear regression equation relates porosity to permeability using the slope and the intercept of the equation, the null hypothesis is that of zero slope, which yields a constant function. The hypothesis tests were performed at the 95% confidence interval.

Results

Permeability values were plotted on an outline of Neuzil's (1994) compiled range of permeabilities as a function of porosity for argillaceous sediments (Figure 2-5). The majority of permeability values were enveloped within Neuzil's (1994) plot. However, several samples from Site 1231 of Peru and Sites 1039 and 1040 of Costa Rica plotted outside Neuzil's (1994) plotted area. These include non-argillaceous sediments of calcareous oozes and few samples containing siliceous oozes.

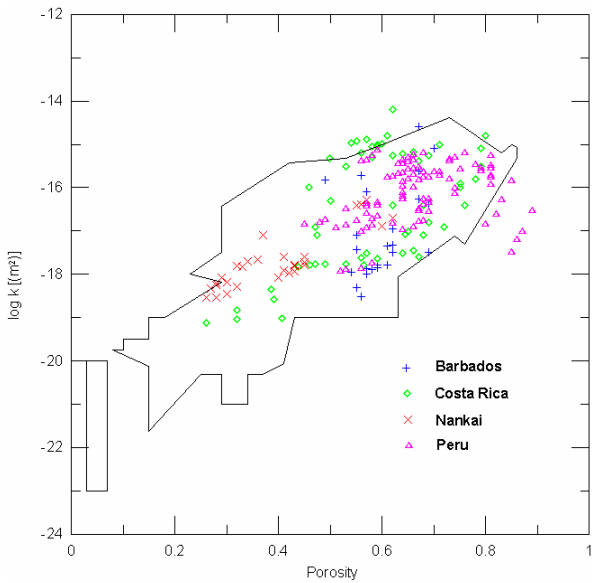


Figure 2-5. Plot of laboratory derived permeability measurements from Barbados, Costa Rica, Nankai, and Peru subduction zones superimposed on outline of Neuzil's (1994) plot for argillaceous sediments. As compared to Neuzil's (1994) paper, the axes have been transposed.

Effects of Depositional Environment

According to Boggs (2001) there is little agreement regarding the classification of deep-sea sediments and thus, suggested classifications range from those that are largely genetic to those that are largely descriptive. Unfortunately there is no single classification that take into account both genesis and descriptive properties of all kinds of deep-sea sediments (Boggs, 2001). Thus, here I used generalized descriptions used by Boggs (2001) to categorize hemipelagic and pelagic sediments. Hemipelagic muds are defined as mixtures of fine-grained terrigenous mud with biogenic remains that are deposited under very low current velocities. According to Stow and Piper (1984), hemipelagic muds contain more than 5% biogenic remains and a terrigenous component of more than 40%. The terrigenous component of the hemipelagic muds are commonly composed of fine terrigenous quartz, feldspar, micas, and clay minerals while biogenic

remains include siliceous organisms such as diatoms and calcareous organisms such as foraminifers and nannofossils (Boggs, 2001).

Following Boggs (2001), I subcategorized the pelagic sediments into two basic groups based on the abundant type of biogenic remains present in the sediment. Pelagic sediments may be composed mainly of clay-size particles of terrigenous or volcanogenic origin or it may contain significant amounts of silt to sand-size planktonic biogenic remains (Boggs, 2001). Pelagic sediments that contain significant amounts of biogenic remains are called oozes. However, little agreement exists with regards to the amount of biogenic remains required to qualify a sediment as an ooze (Boggs, 2001). Boggs (2001) suggested that oozes have more than two-thirds of biogenic components. Thus, depending on which biogenic component is dominant, a sediment can be classified either as a calcareous or a siliceous ooze. The pelagic sediments that are predominantly of calcium carbonate tests were grouped as calcareous oozes while sediments that are predominantly of diatom tests were grouped as siliceous oozes.

In situations where similar lithological descriptions based on depositional environments are used, sediments from different locations were grouped together. For example, Northern Barbados, Nankai and Costa Rica all provide samples of hemipelagic sediments. Because even slight differences in permeability-porosity relationships could affect results of fluid flow models (e.g., Gamage and Screamton, 2006), it is worthwhile comparing the permeability-porosity relationships based on depositional environment between individual locations.

Based on the depositional classification described above all samples from Northern Barbados and Nankai were grouped as hemipelagic sediments. Samples from Costa Rica

represented both hemipelagic sediments as well as calcareous oozes. Samples from Peru consisted of both calcareous and siliceous sediments. Unfortunately the only quantitative data available for the biogenic component of these sediments are from smear slide analyses. As a result it was difficult to determine a representative percentage of the biogenic component. The nannofossil rich samples were grouped as calcareous oozes. The most problematic was to classify the diatom-rich sediments. Lithological descriptions and smear slide analysis favored them in the “siliceous ooze” category, and quantitative data on the components were lacking. However, it should be noted that these samples could contain considerable amounts of biogenic and terrigenous components and may fall in between hemipelagic and pelagic sediments.

Peru samples from Site 1227 were rich in organic carbon and did not fit either of the pelagic sediment categories identified in this study. Thus they were excluded from this study. It should be noted that the samples from Sites 1225 and 1226 represents the sediments of the equatorial Pacific where the direction of plate movement carries them away from the trench. Thus, these two sites do not represent the sediments of the Peru subduction zone. However, they consist dominantly of calcareous oozes, which can be compared to the calcareous oozes of Costa Rica, and for that purpose were included in this study. The two main lithological groups of hemipelagics and pelagics were plotted separately in Figures 2-6.

Based on the calculated R^2 value for the Barbados hemipelagics, the equation explains only 20% of the correlation between permeability and porosity. Although the analysis of residuals showed randomness, the hypothesis testing did not support the existence of a statistically significant correlation between permeability and porosity for

the Barbados hemipelagics. When six of the data points, which were obtained from Taylor and Leonard (1990), were removed from the regression, the R^2 value of the remaining 19 samples increased from 0.20 to 0.50, predicting a permeability-porosity relationship of $\log(k) = -24.24 + 11.31n$. Although statistically this makes the six data points outliers, a closer look at the lithological descriptions, grain size data and CaCO_3 percentages suggest that the hemipelagics samples used by Taylor and Leonard (1990) are likely to be different from the rest of the hemipelagics sediments representative of Barbados because samples used by Taylor and Leonard (1990) represented calcareous muds whereas other samples represented claystones.

Even though many of the samples from Barbados, Nankai, and Costa Rica fall in the depositional classification of “hemipelagics”, they are not well represented by the same permeability-porosity relationship ($\log(k) = -19.91 + 4.9n$, $R^2 = 0.5$). The Barbados permeability-porosity relationship predicts similar values of permeability to Nankai and Costa Rica relationships at porosities between 0.55-0.70 (Table 2-1). However, at lower porosities the Barbados permeability relationship predicts lower values than those of Costa Rica and Nankai. Because Barbados permeabilities are constrained by a small range of porosities, one should be cautious outside the porosity range of the laboratory results. The log-linear relationships for Nankai and Costa Rica plot roughly parallel to each other with slightly lower permeabilities at Costa Rica for a given porosity than at Nankai (Figure 2-6). The R^2 value obtained for Nankai was 0.79 while for Costa Rica it was 0.70 suggesting reasonable correlation between permeability and porosity at these two locations. The R^2 value obtained for the log linear relationships for the calcareous oozes were less than 0.5 while for the siliceous oozes it is greater than 0.5 (Figure 2-6).

The calcareous oozes of Costa Rica plot approximately in the same permeability range as those from Peru, near the upper boundary of Neuzil's (1994) plot.

Table 2-1. Log linear permeability-porosity relationships predicted for varying depositional environments at Barbados, Costa Rica, Nankai and Peru.

Location and Depositional environment	Permeability-porosity relationship
Barbados hemipelagics	$\log(k) = -22.02 + 8.25n$ ($R^2 = 0.20$)
Costa Rica hemipelagics	$\log(k) = -20.84 + 6.27n$ ($R^2 = 0.70$)
Nankai hemipelagics	$\log(k) = -19.80 + 5.37n$ ($R^2 = 0.79$)
Costa Rica calcareous oozes	$\log(k) = -18.09 + 4.83n$ ($R^2 = 0.33$)
Peru calcareous oozes	$\log(k) = -20.87 + 7.79n$ ($R^2 = 0.40$)
Peru siliceous oozes	$\log(k) = -18.64 + 3.55n$ ($R^2 = 0.67$)

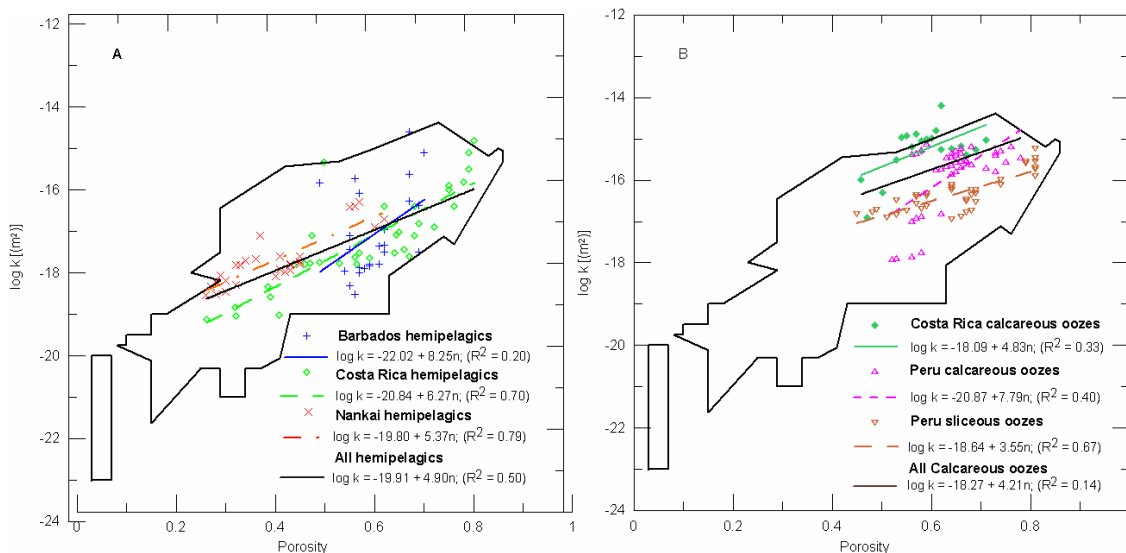


Figure 2-6. Permeabilities classified based on depositional environment and location. A) Predicted log-linear permeability-porosity relationships for hemipelagic samples. B) Permeabilities and predicted log-linear permeability-porosity relationships for pelagic samples.

Peru calcareous oozes lie at a higher porosity range (0.55-0.80) while Costa Rica calcareous oozes represent porosities between 0.45 and 0.70. The Peru siliceous oozes plot between the lower permeability values of calcareous oozes and the higher permeability values of hemipelagic sediments for porosities ranging from 0.45-0.8. Although the predicted R^2 values were fairly low for the two calcareous oozes, a linear relationship between the logarithm of permeability and porosity for those two groups was

not rejected based on the residual distribution and hypothesis testing. Relative to relationships predicted for hemipelagic sediments, the permeability-porosity relationship predicted for the siliceous oozes show similar permeabilities at porosities >0.7 and higher permeability values at porosities <0.7 .

Effects of Grain Size

Bryant et al. (1981) stated that grain size is the most important characteristic of a sediment that determines permeability as it affects the porosity of the sediment. This contention has been supported by studies such as by Koltermann and Gorelick (1995), in which grain size distribution was used to predict permeability and porosity in various sediment mixtures. Ninety percent of their predicted hydraulic conductivities matched the hydraulic conductivities estimated from field tests within one order of magnitude (Koltermann and Gorelick, 1995). Accordingly, I categorized the sediment samples in this study based on a grain size classification described by Bryant (2002). In contrast to Bryant's (2002) study, which exclusively used sediments from the Gulf of Mexico, I combined samples from all four subduction zones due to limited variation in grain size data found at any single location.

Bryant (2002) noted that fine-grained marine sediments with low amounts of carbonate did not affect the permeability-porosity relationship, but did not specify what percent of carbonate was considered. Based on our calcareous pelagic samples I used 45 CaCO₃ wt% as the limit between the high and low carbonate content. The 45 wt% was used because majority of the samples contained either distinctively high ($>> 45$ wt% CaCO₃) or low ($<< 45$ wt% CaCO₃) amounts of CaCO₃. For samples that did not have CaCO₃ wt% data, I used information from other methods such as X-ray diffraction and

inorganic carbon percentages to infer whether samples were likely to contain greater than 45 wt% of carbonates. Although grain size data were available for samples from ODP Leg 112 Sites 679 and 681 (Peru), the scale used for the particle size criteria (Masters and Christian, 1990) was different from the rest of the grain size data used in this study. Thus, I excluded grain size data from Sites 679 and 681 in this part of the study. All samples used in the grain size classification (marked with an asterisk) and values of available weight percentages of CaCO_3 are tabulated in Appendix A.

All samples were categorized into the following four groups based on their grain size distribution:

- Group 1, sediment containing more than 80% clay size material.
- Group 2, sediment containing 60-80% clay-size material.
- Group 3, sediment-containing silty-clays with less than 60% clay and less than 5% sand.
- Group 4, sediment-containing sandy-silts with less than 60% clay and more than 5% sand.

The following particle size criteria were used for classification: sand ($>63 \mu\text{m}$), silt ($63-4 \mu\text{m}$) and clay ($<4 \mu\text{m}$). The log linear relationships for each of the groups obtained by least squares regression fit are given in Table 2-2. Group 4 was excluded from the grain size classification as it only contained a total of four samples.

Table 2-2. Permeability-porosity relationships based on grain size analyses.

Group	Description	Permeability-porosity relationship	Permeability-porosity relationship for Gulf of Mexico (Bryant 2002)*
1	> 80% clay	$\log(k) = -24.28 + 11.32n$ ($R^2 = 0.53$)	$\log(k) = -20.9 + 6.54n$
2	60-80% clay	$\log(k) = -19.73 + 4.49n$ ($R^2 = 0.56$)	$\log(k) = -20.53 + 6.16n$
3	Silty-clays with <60% clay and <5% sand	$\log(k) = -19.91 + 5.45n$ ($R^2 = 0.43$)	$\log(k) = -20.59 + 6.77n$

Bryant (2002) used hydraulic conductivity instead of intrinsic permeability. Thus, the hydraulic conductivities were converted to permeability (Table 2-2) using a viscosity of 0.000966 Pa·s and density of 1023 kg/m³ at a temperature of 25°C and a salinity of 35 kg/m³.

Based on the grain size classification, Group 1 consists only of hemipelagic samples that are representative of Barbados. Group 2 consists of hemipelagic samples from Barbados, Nankai and Costa Rica while Group 3 consists of Nankai and Costa Rica hemipelagics. In general the permeability-porosity relationship obtained from grain size classification suggests an increase in permeability with a decrease in clay size particles. The R² values predicted from the permeability-porosity relationships show R² > 0.5 for Groups 1 and 2 and 0.48 for Group 3 (Figure 2-7). It should be noted that the 95% confidence intervals for the grain size groupings show an overlap, suggesting that the permeability-porosity relationships are not statistically significantly different from each other. This overlap is probably caused by the difficulties in permeability measurements, and the likelihood that sediments with slightly varying grain size percentage (e.g., 79% clay versus 81% clay) may not have distinguishable values of permeability, despite being classified in different categories. Although the R² values predicted from grain size classification were higher than the ones predicted by depositional environment only, it predicted lower R² values than those predicted from classification based on location except for Barbados. This may suggest that varying deformational processes at different locations may affect sediment properties at varying degrees.

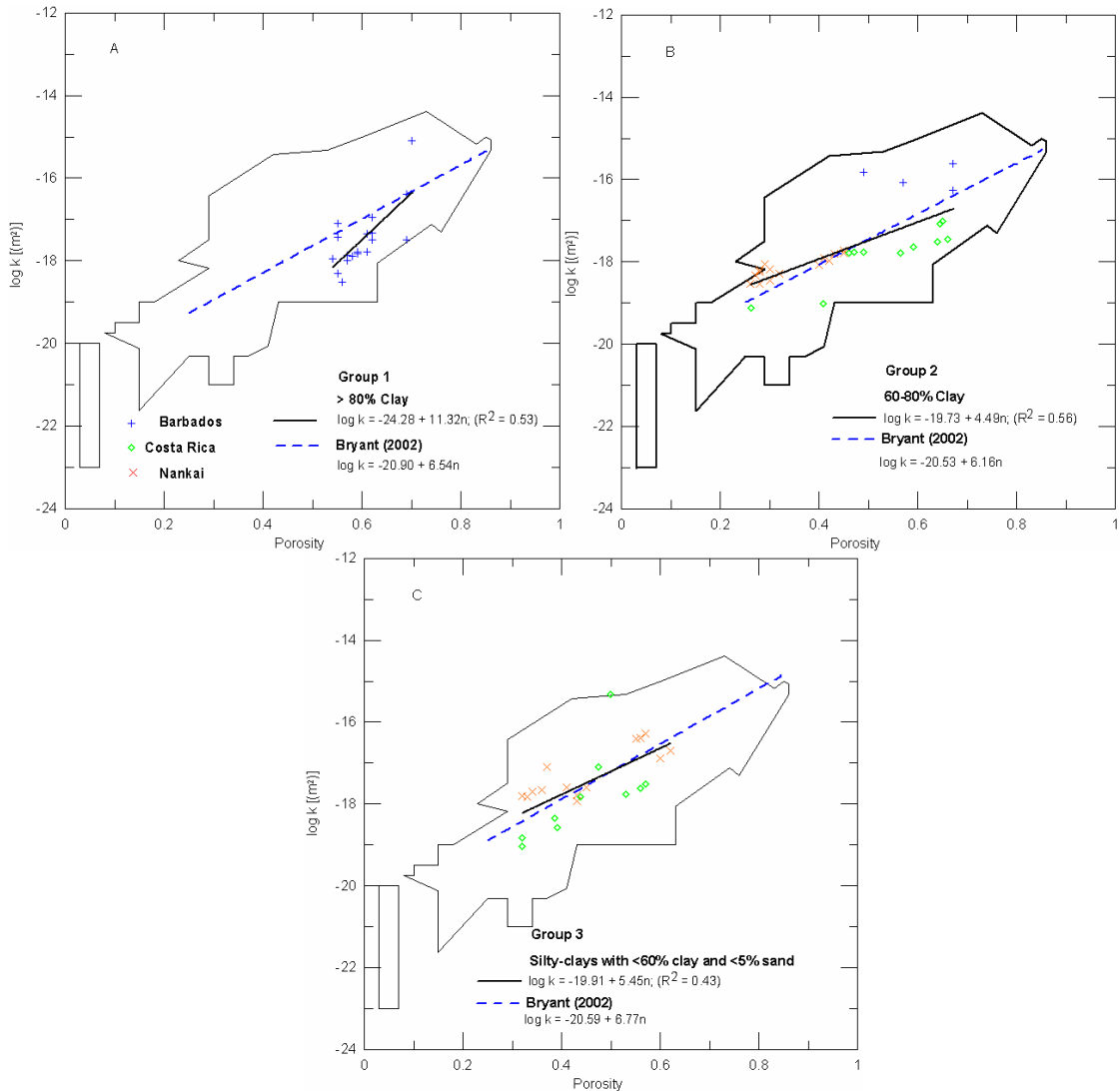


Figure 2-7. Permeabilities classified based on grain size distribution. Solid lines represent permeability-porosity relationship predicted for samples used in this study. Dashed line represents permeability-porosity relationships of Bryant (2002).

In order to understand the general trend of permeability-porosity relationships based on grain size distribution, I compared my data with that of Bryant's (2002) Gulf of Mexico data, which were obtained through consolidation tests. The dashed lines in Figure 2-7 represent the relationships of Bryant (2002) and solid lines represent predicted relationships from this study. For Group 1, the predicted permeability from this study matched the permeabilities of Bryant's (2002) at porosities around 0.6 to 0.7. As

porosities decrease our relationship for Group 1 predicted lower values of permeability than Bryant's (2002) permeability-porosity relationship. The large discrepancy between Bryant's (2002) and this study's relationship in Group 1 might be caused by the narrow range of porosities (0.50-0.70) represented by the Group 1 data. In contrast Groups 2 and 3 represent a larger range of porosities between approximately 0.25-0.70. Group 3 shows fairly similar permeability-porosity relationships to those of Bryant's (2002) while our Group 2 relationship crosses Bryant's (2002) permeability-porosity relationship at a porosity of 0.5.

Effects of Structural Domain

Samples that were used for the grain size analyses were further categorized based on the structural domains of each sample to test the effect of deformation on the permeability-porosity relationship. Samples that represented the underthrust sediments and the incoming sediments at reference sites were grouped together as they represented the undeformed or minimally deformed sediments of the subduction complex. Prism sediments and sediments that represented the décollement zone were grouped together as these samples generally are highly deformed during the accretionary process. Only grain size Group 2 of our samples had a considerable amount of samples that represent both the underthrust/incoming sediments and the prism/décollement sediments. Using the data from Group 2, I fitted linear regression lines for both the underthrust/incoming sediment and the prism/décollement sediment groups (Figure 2-8).

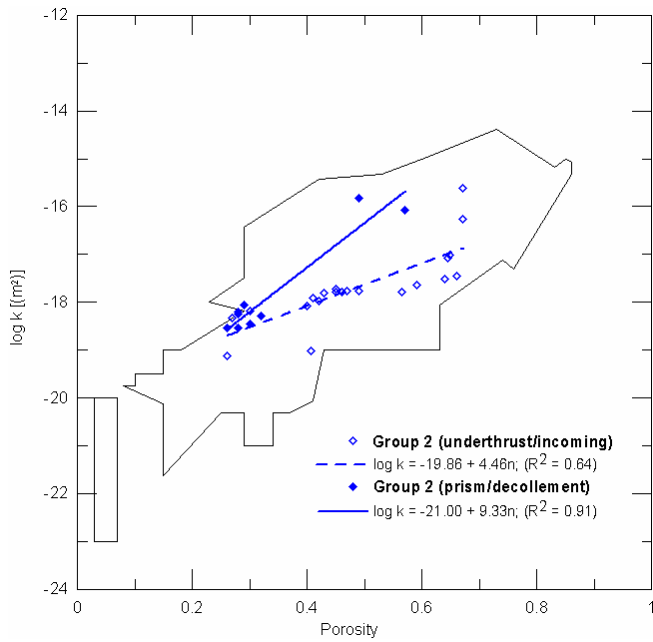


Figure 2-8. Permeabilities classified based on structural domain. Permeability-porosity relationships only shown for underthrust/incoming samples (dashed line) and prism/décollement samples (solid line) of Group 2.

The prism/décollement sediments group only contained eight samples and thus, gave a relatively high R^2 value of 0.91. The underthrust/incoming sediment group contained twenty-two samples and showed moderate correlation between permeability and porosity with a R^2 value of 0.64. Even with the limited data available, the two relationships exhibited similar permeabilities at lower porosity values (0.2-0.3). With increasing porosities the two relationships predicted permeabilities that diverge from each other. For example, the permeability-porosity relationship of prism/décollement group predicted a permeability value of $1 \times 10^{-16} \text{ m}^2$ at a porosity value of 0.50 while at the same porosity level the underthrust/incoming group predicted a lower permeability value of $1 \times 10^{-18} \text{ m}^2$. The differences exhibited in these two permeability-porosity relationships, while inconclusive, suggest that it might be useful to study more samples representing each group, particularly the prism/décollement group, to test the predicted relationships.

Discussion

The hemipelagic samples used in this study were well confined within the limits of Neuzil's (1994) plot of argillaceous sediments. Although hemipelagic samples plotted in the same region, the predicted permeability-porosity relationships varied with location. In the case of Barbados, the permeability-porosity relationship showed scatter even within an individual location due to variations found in the hemipelagic sediments. These varying relationships suggest that samples categorized as "hemipelagics" could have different permeability-porosity relationships at different locations. Thus, combined classification of both depositional environment and location may provide better correlation between permeability and porosity.

In general the observed differences in the log permeability-porosity relationship appears correlated to the amount of clay and silt size particles present in the sample. Except for Group 1, our predicted permeability-porosity relationships based on grain size distribution are in good agreement with the relationships of Bryant (2002). Groups 2 and 3 exhibited similar trends as those predicted by Bryant's (2002). This similarity suggests that even though samples were taken from different subduction zones, samples classified based on their grain size distribution exhibit similar trends between permeability and porosity compared to those samples that were taken from a single location (e.g., Bryant's (2002) samples from Gulf of Mexico). Thus, it could be concluded that the permeability-porosity relationships obtained based on grain size distribution are generally applicable to samples from marine settings. However, additional data, particularly in Group 1, would further test this conclusion.

At high porosities, the relationship predicted for the siliceous oozes suggests similar permeabilities to those predicted for hemipelagic sediments. However, there were

no samples that represent lower porosities (less than 0.45) of the siliceous oozes and therefore the predicted relationship should be used with caution at lower porosities.

The lack of correlation exhibited between permeability and porosity in calcareous oozes suggest that one should consider other variables such as depth, consolidation rates and relative age of the sediment to obtain meaningful relationships for pelagic sediments. According to Bryant et al. (1981), unlike grain size, the influence of calcium carbonate is more pronounced with increasing depth because as burial increases less reduction of porosity is observed for calcareous sediments compared to non-calcareous sediments. Mechanical compression tests conducted by Terzaghi (1940) and Robertson (1967) demonstrated that calcareous muds compact less than non-calcareous muds. A similar study by Bryant et al. (1981) demonstrated that under a similar load, carbonate sediments do not consolidate to as low a void ratio as non-carbonates. Based on this finding they speculated that the resistance towards consolidation in carbonates could be a result of the relative age of the sediment or the differences in particle shape or the structural strength of the individual particles.

Even though comparison of underthrust/incoming and prism/décollement structural domains from Group 2 suggested the possibility of different varying permeability-porosity relationships, it is recommended to further investigate these relationships using more samples; the results presented here are based on a limited number of samples especially those represented by the prism/décollement group. It would be worthwhile to further test the effects of structural domain on permeability-porosity relationship, as this information will allow future studies based on permeability-porosity relationships to more realistically represent fluid flow.

This study used a large number of data from many different sources to investigate the relationship between permeability and porosity. Assembling data for this study highlighted the importance of documenting detailed methodology including critical data such as the temperature during permeability testing and the type of permeant used in the flow test. It is also important to have porosity and grain size data available for documented permeability values, as these parameters are valuable estimating relationships between permeability and porosity. This study also identified gaps in available data. For example, only a few sediment samples were available from the structural domain representing the prism/décollement and few samples from Barbados were tested at low porosities. Thus, future data collections should focus on collecting samples representing the prism and the décollement as well as deeper parts of the underthrust sediments, where much remains to be learned.

Conclusions

I examined permeability-porosity relationships for sediments from four different subduction zones based on their depositional environment, grain size distribution, and structural domain. Greater correlation was observed between permeability and porosity for hemipelagic sediments and for siliceous oozes while relatively low correlations were predicted for calcareous oozes. Based on the hemipelagic samples used in this study, it is clear that permeability-porosity relationships vary among hemipelagics at different locations and thus, classification based on depositional environment should be used with caution when applied at different locations. Grain size predicts more meaningful correlation between permeability and porosity than depositional environment only, and these relationships are generally consistent with results from other marine settings. However, grain size classification shows less correlation between permeability and

porosity relative to the relationships predicted by location. Due to lack of data, the effect of structural domain on permeability-porosity relationship could not be evaluated. To predict meaningful relationships for permeability of carbonaceous sediments, one should consider other factors such as depth, consolidation rates, and relative age of the sediment.

CHAPTER 3
CHARACTERIZATION OF EXCESS PORE PRESSURES AT THE TOE OF THE
NANKAI ACCRETIONARY COMPLEX, OCEAN DRILLING PROGRAM SITES
1173, 1174, AND 808: RESULTS OF ONE-DIMENSIONAL MODELING

Introduction

Examining the fluid flow of the deep hydrosphere is extremely important because fluid flow alters the physical and chemical properties of the Earth's crust, affecting the ocean and the atmospheric chemistry that is vital for human existence (COMPLEX, 1999). At active plate margins, fluid pressures can influence movement along faults and thus, the nature of the earthquake cycle (Moore and Vrolijk, 1992). Pore fluid pressures build up in areas where sediment permeabilities are low enough to prevent pore fluid escape at a rate comparable to the rate of loading due to tectonic and gravitational stresses. These elevated fluid pore pressures play an important role in the development of accretionary complexes. It is speculated that high pore pressures control the formation of the décollement, which separates highly deformed overlying wedge sediments from slightly deformed underthrust sediments (Westbrook and Smith, 1983). Furthermore, pore pressures affect deformation within and the taper angle of the accretionary wedge (Davis et al., 1983).

At the Nankai accretionary complex, a thick terrigenous sequence rapidly deposits over a low-permeability hemipelagic sequence. Previous studies have used indirect estimates to document the development of pore pressures within the underthrust sediments at the toe of the Nankai accretionary complex. For example, Screamton et al. (2002) estimated depth-averaged excess pore pressures using porosity-depth profiles.

The estimated overpressures within the underthrust sediments suggest insufficient permeability for fluid escape at a rate comparable to sediment loading. Saffer (2003) used shipboard observations of porosity and laboratory measurements of consolidation to estimate pore pressures and evaluate their variations down section. His results indicate undrained conditions in the underthrust sediments that may have been caused by rapid sedimentation and loading due to underthrusting. A modeling study conducted by Le Pichon and Henry (1992) suggested that trench sedimentation and rapid accretion at the toe of the prism could generate excess pore pressures in the underthrust sediments at and even seaward of the deformation front. However, that study did not have permeability data, and used estimates based on lithologies.

In this study, I used laboratory permeability data to investigate porosity reduction and the generation of excess pore pressures at the toe of the Nankai accretionary complex. Based on measured permeabilities I developed a permeability-porosity relationship for hemipelagic sediments at the Nankai accretionary prism. I then used this permeability-porosity relationship in a one-dimensional numerical model to simulate the excess pore pressures and porosities that would result from sedimentation and loading by the prism at the toe of the accretionary complex. Finally I tested the sensitivity of excess pore pressures and porosities to bulk permeability, lateral stresses within the prism, and a hypothetical low-permeability barrier at the décollement.

Background

Geologic Setting

The Nankai accretionary complex is formed by the subduction of the Shikoku Basin on the Philippine Sea Plate beneath the southwest Japan arc on the Eurasian plate (Figure 3-1) at a rate of 4 cm/yr (Seno et al., 1993). This study focused on the Muroto

Transect (Figure 3-1) where the thickness of the complex varies from 750 m at the toe to ~4500 m at 50 km arcward. Along the Muroto Transect, the prism toe has a taper angle of 4°-5° (Shipboard Scientific Party, 2001). Based on this low taper angle, it has been inferred that the Muroto Transect has high décollement pore pressures or low intrinsic décollement strength (Saffer and Bekins, 2002).

During ODP Leg 131, Site 808 was drilled on the Muroto Transect approximately 3 km landward of the deformation front. A 560 m thick sequence of turbidites was found above the hemipelagic muds of the upper and lower Shikoku Basin facies. The décollement zone was identified by intense brittle deformation at 945 to 964 meters below seafloor (mbsf), and develops from a homogeneous interval of hemipelagic mudstones within the lower Shikoku Basin facies (Shipboard Scientific Party, 2001). During ODP Leg 190, Sites 1173 and 1174 were drilled seaward of Site 808 along the Muroto Transect (Figure 3-2).

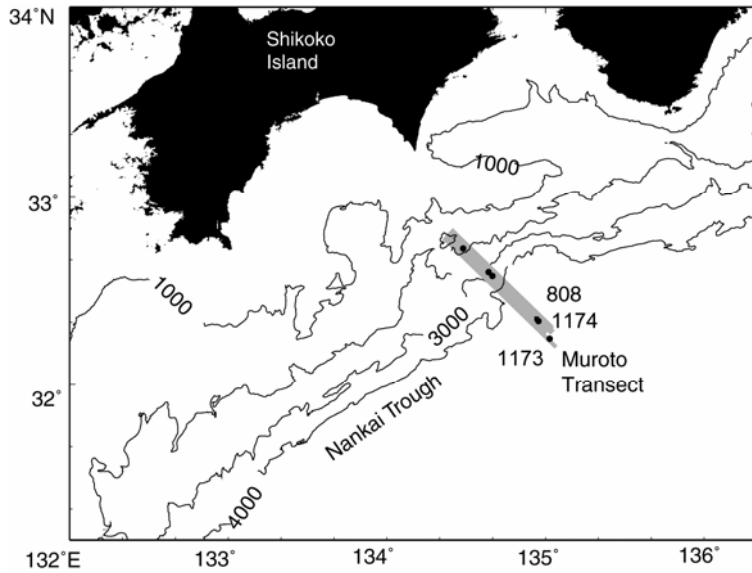


Figure 3-1. Location map of the study area in the Nankai accretionary complex and sites used for this study (modified from Moore et al., 2001).

Site 1174 penetrated the décollement within the proto-thrust zone (Figure 3-2). The décollement was observed between 808 and 840 mbsf and was marked by fractures and brecciation in the lower Shikoku Basin facies (Shipboard Scientific Party, 2001). The turbidites extended 431 m above the hemipelagic muds of the upper and lower Shikoku Basin facies (Shipboard Scientific Party, 2001).

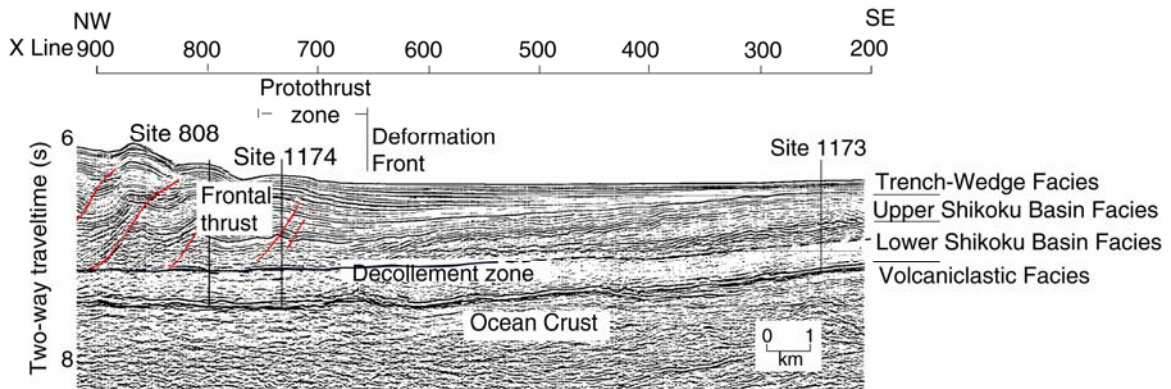


Figure 3-2. Schematic interpretation of the Muroto Transect showing tectonic domains and location of Leg 190 drill sites used in this study (modified from Moore et al., 2001).

Site 1173 was drilled 11 km seaward of the deformation front providing an undeformed reference site of the incoming sedimentary sequence (Shipboard Scientific Party, 2001). The turbidite layer at Site 1173 is much thinner (~102 m) than at Site 1174, because it is farther away from the trench. At Site 1173, the age equivalent of the Site 1174 décollement zone occurs between 390 and 420 mbsf, within the lower Shikoku Basin facies (Shipboard Scientific Party, 2001).

At the Nankai accretionary complex, heat flow values ranging from 180 mW/m² at Sites 1173 and 1174 to 130 mW/m² at Site 808 have been estimated (Shipboard Scientific Party, 2001). These measured high heat flow values are related to the fossil spreading ridge represented by the Kinan Seamount on the Philippine Sea Plate which ceased spreading ~ 15 Ma ago (Shipboard Scientific Party, 2001). Previous studies have

suggested that high temperatures at the Muroto Transect could affect in situ dehydration reactions such as the smectite to illite transition (Kastner et al., 1993) as well as observed cementation by authigenic clays (Ujiie et al., 2003).

Previous Hydrologic Studies

Previous workers have examined several aspects of fluid flow and pore pressure development at the Nankai accretionary complex. Le Pichon and Henry (1992) used a one-dimensional model of sedimentation representing the stratigraphic sequence at Site 808. Their model consisted of a coarser terrigenous sediment layer with permeability values of 10^{-16} to 10^{-17} m², rapidly depositing over a less permeable hemipelagic sequence (10^{-19} to 10^{-17} m²). Because permeability data for Nankai sediments was not available, they used permeabilities that are representative of uncompacted terrigenous and hemipelagic sediments. Their modeling results showed that this stratigraphic succession could potentially form a low mechanical resistance horizon within the upper portion of the low permeability sediments, but testing of their model requires permeability data.

Taylor and Fisher (1993) performed permeability measurements on subsamples of Site 808 cores using two methods. One method directly measured flow under known head values and the other method indirectly measured flow from the rate of consolidation due to a known applied stress. Their measured permeabilities ranged from 10^{-14} to 10^{-19} m² in horizontal and vertical directions.

Saffer and Bekins (1998) used a log-linear permeability-porosity relationship and an assumed porosity distribution in a two-dimensional numerical model to match pore pressures estimated from the critical taper theory of Davis et al. (1983). The critical taper is the shape for which the wedge is on the verge of failure under horizontal compression and to maintain a small critical taper it requires high basal pore pressures (Davis et al.

1983). For varying assumptions about permeability and porosity distribution within the underthrust sediments, Saffer and Bekins (1998) simulated λ^* values between 0.2-0.4 in the region of Sites 1174 and 808. It should be noted that these simulations assumed a constant décollement permeability of 10^{-16} m^2 .

The estimated permeability-porosity relationships of Saffer and Bekins (1998) fall within the range for argillaceous rocks defined by Neuzil (1994), but was approximately two orders of magnitude lower than the direct permeability measurements given by Taylor and Fisher (1993). Saffer and Bekins (1998) suggested that direct permeability measurements by Taylor and Fisher (1993) were overestimates due to fabric expansion, because these measurements were performed on samples that were not reconsolidated under pressure. Moreover, Saffer and Bekins (1998) argued that the use of air in the Taylor and Fisher (1993) permeability tests would tend to further overestimate permeabilities.

Screaton et al. (2002) used porosity measurements of core samples from Sites 808 (Shipboard Scientific Party, 1991), 1174, and 1173 (Shipboard Scientific Party, 2001) to estimate pore pressures in the underthrust sediments. In this study, Screaton et al. (2002) assumed that the solid volume is constant thus relating the change in volume to change in porosity. Site 1173 was assumed to provide a reasonable proxy for conditions of the Sites 1174 and 808 sediments when they were seaward of the trench. The average porosities of the underthrust (or equivalent) sediments of the lower Shikoku Basin facies decrease landward from 0.42 at Site 1173 to 0.34 and 0.33 at Sites 1174 and 808, respectively (Screaton et. al., 2002). The porosity profile from Site 1173 shows steadily decreasing porosity with increasing depth (Figure 3-3).

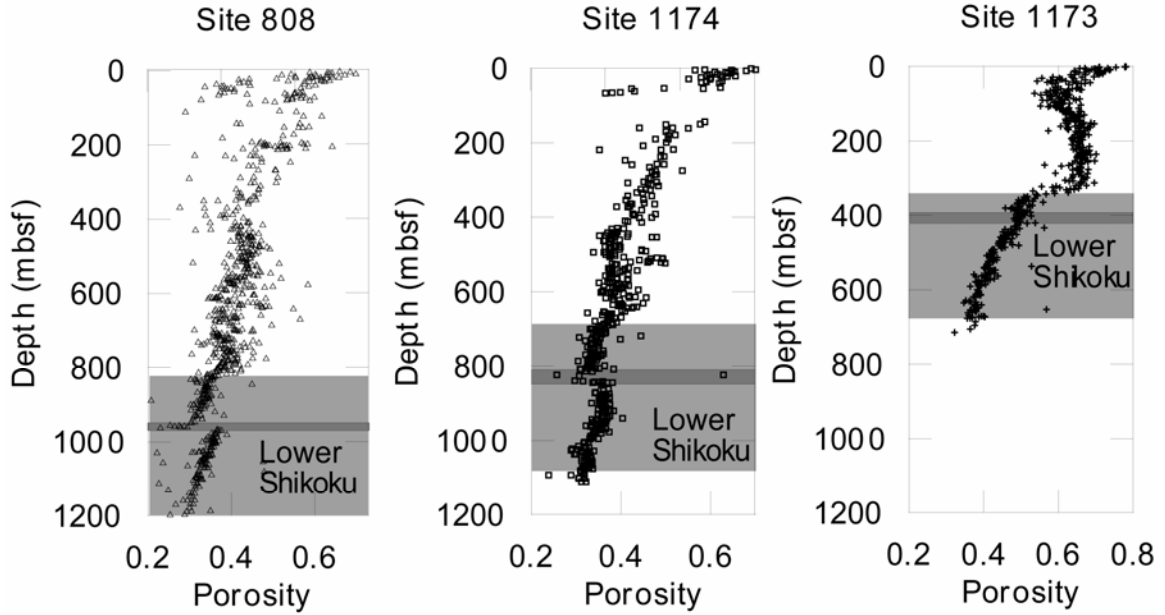


Figure 3-3. Porosity profiles of Sites 808, 1174, and 1173. Light shading shows lower Shikoku Basin facies. Darker shading represents the décollement zone at Sites 808 and 1174 and at Site 1173 the age-equivalent level of Site 1174 décollement zone.

At Sites 1174 and 808 the porosities below the décollement increase relative to the porosities above. Comparison between the porosity profiles of the underthrust sediments from Sites 1174 and 808 with the reference site (Site 1173) suggest excess pore pressure ratio (λ^*) of 0.42 at Site 1174 and 0.47 at Site 808 (Screaton et al., 2002), where λ^* represents the magnitude of excess fluid pressure relative to sediment overburden pressure and is defined as

$$\lambda^* = (P - P_h)/(P_l - P_h) \quad (1)$$

where P is pore fluid pressure [$M L^{-1} T^{-2}$], P_h is hydrostatic pressure [$M L^{-1} T^{-2}$], and P_l is lithostatic pressure [$M L^{-1} T^{-2}$]. The excess pore pressure ratio removes the effect of the overlying water column, and describes excess fluid pressures within the sedimentary sequence relative to the overburden load minus hydrostatic pressure. For lithostatic pore pressures, $\lambda^* = 1$, whereas at hydrostatic pressures, $\lambda^* = 0$.

Saffer (2003) integrated measurements of logging-while-drilling (LWD), physical properties data, and laboratory consolidation tests to compare pore pressure development and progressive dewatering in the underthrust sediments. Calculations of λ^* based on Saffer's (2003) results indicate values of 0.30 and 0.44 at 15 m below the décollement at Sites 1174 and 808, respectively. These values are slightly lower than the average values over the entire underthrust profile inferred from porosity data by Screamton et al. (2002). The estimated λ^* values calculated from results of Saffer (2003) generally decrease with depth below the décollement at both Sites 1174 and 808.

Evidence concerning possible lateral fluid flow is ambiguous. Broad low chloride anomalies were observed within the lower Shikoku Basin facies (Kastner et al., 1993; Gieskes et al., 1993; Spivack et al., 2002). Controversial ideas have been suggested as possible explanations for the observed low chloride anomalies. Kastner et al. (1993) and Underwood et al. (1993) suggested that smectite dehydration is the most likely mechanism for the observed low-chloride anomaly. On the basis of geochemical analyses, Kastner et al (1993) suggested lateral fluid flow along the décollement or along a deeper conduit within the underthrust sediments while Spivack et al. (2002) suggested continuous lateral fluid flow between Sites 808 and 1174 within the underthrust sediments. Brown et al. (2001) suggested that in situ dehydration of ~10-15 wt% of smectite could generate most of the freshening observed at Site 808 and therefore, provides a possible explanation for pore fluid freshening. However, if the initial amount of smectite is less than 10-15 wt% then the low-chloride anomaly could reflect the combined effects of both in situ and lateral flow at depth (Brown et al., 2001). This in situ dehydration hypothesis has been further supported by a recent study by Henry et al.

(2003) using cation exchange capacity. Henry et al. (2003) showed that there are sufficient amounts of smectite to explain the chlorinity anomalies by in situ reactions, and thus, lateral fluid flow is not required. Although fluid from dehydration greatly affects pore water chemistry, Saffer and Bekins (1998) suggest that fluid sources from dehydration of smectite are 10-1000 times smaller than the compaction fluid sources. Thus, dehydration fluid sources are unlikely to be significant in generating pore fluid pressures at the toe of the prism.

Laboratory Permeability Measurements

Although previous studies have provided evidence for excess pore pressures at the Nankai accretionary complex, the causes of it were not sufficiently characterized due to lack of well-constrained data in sediment properties. Because sediment permeability is the most important factor in controlling modeled pore pressures, it is important to establish a systematic relationship between permeability and porosity to approximate permeability in the accretionary complex (Saffer and Bekins, 1998). Thus, as the first step of the study I used laboratory measured permeability data from nine core samples at varying depths to establish a permeability-porosity relationship. Gamage and Screamton (2003) provide detailed information about test methods. Vertical permeability tests were performed using the constant flow method on nine core samples taken from the Shikoku Basin facies at Sites 1173 and 1174. The constant flow permeability method induces a hydraulic gradient across the sample, and measurement of the pressure difference allows determinations of permeability. To determine porosities for the permeabilities presented by Gamage and Screamton (2003), I calculated change in porosity during consolidation based on the change in volume of fluid [L^3] contained in the cell at the end of each

consolidation step, and used shipboard porosity measurements for the initial porosities (Table 3-1).

Table 3-1. A summary of laboratory measured permeabilities for samples from ODP Leg 190 Sites 1173 and 1174. Permeability values were recalculated (as compared to Gamage and Screamton, 2003) based on a viscosity value of 0.0008 kg/s.m and a density of 1020 kg/m³, based on laboratory temperatures during testing (Lide, 2000). Values for Sample 1174B-84R-3, which are included in Gamage and Screamton (2003) are not presented here due to insufficient data to calculate porosities at measured permeability values.

Sample	Effective Stress (MPa)	Porosity	Permeability (m ²)
1173A-22H-2, 199.9 mbsf, Silty clay	0.24	0.57	5.14 x 10 ⁻¹⁷
	0.42	0.56	4.02 x 10 ⁻¹⁷
	0.54	0.55	3.90 x 10 ⁻¹⁷
1173A-31X-1, 284.59 mbsf, Silty claystone to	0.27	0.62	1.98 x 10 ⁻¹⁷
	0.42	0.60	1.28 x 10 ⁻¹⁷
1173A-39X-5, 367.07 mbsf, Silty claystone,	0.26	0.41	2.46 x 10 ⁻¹⁸
	0.39	0.36	2.18 x 10 ⁻¹⁸
	0.83	0.33	1.51 x 10 ⁻¹⁸
1173A-41X-cc, 388.75 mbsf, Silty claystone,	0.29	0.45	2.48 x 10 ⁻¹⁸
	0.41	0.43	1.66 x 10 ⁻¹⁸
	0.55	0.43	1.18 x 10 ⁻¹⁸
1173A-46X-1, 428.59 mbsf, Silty claystone	0.25	0.45	1.90 x 10 ⁻¹⁸
	0.40	0.43	1.52 x 10 ⁻¹⁸
	0.51	0.41	1.24 x 10 ⁻¹⁸
1174B-42R-3, 538.23 mbsf, Silty claystone, altered	0.19	0.37	7.84 x 10 ⁻¹⁸
	0.48	0.34	2.00 x 10 ⁻¹⁸
	0.62	0.32	1.52 x 10 ⁻¹⁸
1174B-59R-5, 704.95 mbsf, Silty claystone	0.55	0.32	5.18 x 10 ⁻¹⁹
	0.69	0.30	3.53 x 10 ⁻¹⁹
	0.83	0.28	2.94 x 10 ⁻¹⁹
1174B-69R-2, 795.17 mbsf, Silty claystone,	0.55	0.29	8.48 x 10 ⁻¹⁹
	0.69	0.28	5.78 x 10 ⁻¹⁹
	0.83	0.26	2.83 x 10 ⁻¹⁹
1174B-74R-1, 842.75 mbsf, Silty claystone-	0.55	0.30	6.40 x 10 ⁻¹⁹
	0.69	0.28	6.16 x 10 ⁻¹⁹
	0.83	0.27	4.70 x 10 ⁻¹⁹

For clay-rich sediments, Bryant et al. (1975) and Neuzil (1994) established that logarithm (base 10) of permeability (k) decreases systematically with decreasing porosity (n) and thus, k can be represented as a function of porosity,

$$\log(k) = \log(k_0) + \varphi n \quad (2)$$

where k_0 is the projected permeability at zero porosity and φ is a parameter describing the rate of permeability change with porosity.

With respect to Neuzil's (1994) compilation of permeability data for argillaceous sediments, most of the Nankai core permeability values fall in the central portion of the data range (Figure 3-4), while a few permeability values with porosities between 0.2 and 0.3 fall closer to the higher-permeability margin of the data range. The measured permeability values are best fit by the following relationship:

$$\log(k) = -19.82 + 5.39n \quad (3)$$

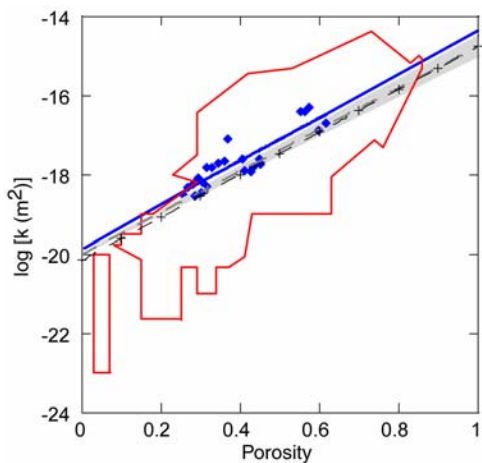


Figure 3-4. Permeability data measured for samples from ODP Leg 190 (solid diamonds) superimposed on a large-scale permeability versus porosity outline for argillaceous sediments compiled by Neuzil (1994). Solid line represents the best-fit line for the measured permeabilities. The dashed line with + mark represents the permeability-porosity relationship for the lower range of measured permeability values. The shaded area represents the range of permeability-porosity relationships established by Saffer and Bekins (1998), with the dashed line ($\log(k) = -20 + 5.25n$) indicating a mid-range value.

The permeability-porosity relationship obtained from this study has a similar slope to the relationships used by Saffer and Bekins (1998) ($\log(k) = -20 + 5.25 n$) but predicts slightly higher permeability values (Figure 3-4). The lower range of permeability values

are near the bottom of the range used by Saffer and Bekins (1998) relationship, and can be represented by a line with the relationship, $\log(k) = -20.15 + 5.39n$ (Figure 3-4).

Modeling Methods

Theoretical Background

As sediments are loaded, the sediment column beneath will compact if the pore fluid can escape at a rate comparable to the loading rate. However, if the permeability of the sediment column is low, dewatering will be inhibited, excess pore pressures will build, and compaction will be prevented. Darcy's Law expresses the relationship between pore pressures, sediment properties, and fluid velocities. For constant density saturated flow, Darcy's Law can be written in terms of the hydraulic head (Voss, 1984).

$$v = -\left(\frac{K}{n}\right)\nabla h \quad (4a)$$

$$\text{where } h = \frac{P}{\rho_f g} + h_z \quad (4b)$$

where v is pore fluid velocity [$L T^{-1}$], K is hydraulic conductivity [$L T^{-1}$], n is porosity, h is hydraulic head [L], ρ_f is fluid density [$M L^{-3}$], g is gravitational acceleration [$L T^{-2}$], and h_z is elevation head [L]. Hydraulic conductivity is defined by $K=k\rho_f g/\mu$, where k is intrinsic permeability [L^2] and μ is dynamic viscosity [$M L^{-1} T^{-1}$]. Intrinsic permeability is a function of the porous medium while fluid density and viscosity depend on the properties of the fluid and may change with temperature, salinity, and to a lesser extent with pressure.

Combining the mass conservation of fluid with Darcy's law (Eq. 4a), the following equation can be written for diffusion of head in porous media for saturated fluid flow.

$$-\nabla(K\nabla h) = S_s \frac{\partial h}{\partial t} + Q \quad (5)$$

where S_s is specific storage [L^{-1}], and t is time [T]. Specific storage is a measure of the volume of formation fluid per unit volume of media per unit head of a saturated formation that is stored or expelled from storage due to compressibility of the matrix and change in fluid pressure. Specific storage is defined as $S_s = \rho_f g(\alpha + n\beta)$ where α is matrix compressibility [$M^{-1} L T^2$], and β is the compressibility of the formation fluid [$M^{-1} L T^2$]. Matrix compressibility (α) is defined by $\alpha = [1/(V)](dV/d\sigma_e)$ where V is the bulk volume [L^3] and σ_e is the effective stress [$ML^{-1}T^{-2}$]. The second term on the right hand side is a source term representing changes to fluid volume or pressure, such as due to loading, per time per unit volume of media [T^{-1}].

During loading, the stress added from the sediment load is partitioned between the pore fluid and the matrix. The loading efficiency, γ , denotes the fraction of the stress added to the pore fluid pressure and, assuming the sediment grains are incompressible relative to the matrix, is defined as follows (after Neuzil, 1986)

$$\gamma = \alpha / (\alpha + n\beta) \quad (6)$$

For highly compressible sediments, the loading efficiency is near 1.

The increase in pore pressure caused by loading drives fluid flow. When initial conditions, boundary conditions and the controlling hydrogeologic parameters k and α are known, Equation 5 can be solved for hydraulic head at any point at any time, and thus, pore fluid velocity relative to the sediment framework can be calculated using Equation 4a.

The pore pressure is related to effective stress (σ_e) by

$$\sigma_e = \sigma_t - P \quad (7)$$

where σ_t is the total stress. As fluid escapes, pore pressure decreases and effective stress increases, causing porosity to decrease. For sediments that are normally compacting (sediments at hydrostatic pore pressure), porosity has been observed to decrease exponentially with depth, as suggested by Athy (1930)

$$n = n_0 \exp[-bz] \quad (8)$$

where n_0 is initial porosity, b is a constant [L^{-1}], and z is burial depth [L]. For hydrostatic conditions, the change in effective stress, σ_e , with depth is given by

$$(d\sigma_e / dz) = (\rho_s - \rho_f) (1-n) g \quad (9)$$

where ρ_s is grain density. Combining Equations 8 and 9 results in

$$(dn / d\sigma_e) = (-bn) / [(\rho_s - \rho_f) (1 - n) g] \quad (10)$$

Equation 10 is only applicable for sediments undergoing compaction. For this investigation, it is assumed that sediments cannot decompress or expand when the effective stress is reduced. Thus, porosities will remain constant unless the effective stress exceeds the previous maximum effective stress value. The change in volume (dV) can be related to (dn) by

$$dV / V = (dn) / (1 - n) \quad (11)$$

In one dimension, the volume change represents only the change in vertical thickness and thus the horizontal dimension of the sediment column stays constant. As porosity decreases with depth, matrix compressibility (α) is also reduced. Based on Equations 10 and 11, the matrix compressibility is calculated as

$$\alpha = (bn) / [(\rho_s - \rho_f) (1-n)^2 g] \quad (12)$$

Model Implementation

This modeling study focused on Sites 1173, 1174, and 808 to examine the development of pore pressures along the Muroto Transect during early subduction. Modeling is one-dimensional, and thus, lateral fluid flow cannot be included. However, as discussed above, evidence for lateral fluid flow at this Transect is inconclusive. A method previously described by Screamton and Ge (2000) and Kemerer and Screamton (2001) was modified for this investigation to add the permeability-porosity relationship (Eq. 2). The modeling method combines a loading program to simulate pore pressure increases due to sedimentation and initial subduction with an existing fluid flow and transport code, SUTRA (Voss, 1984).

Based on the rate of sedimentation or thickening of the overriding prism for each of the segments, the loading program calculates the additional thickness of each added sediment layer. As new sediment layers are added to the top of the model, the layers beneath were moved down one row, and their pore pressures were incremented with the additional pore fluid pressure due to the load of the new layers multiplied by γ (Eq. 6). The additional load is calculated from the thickness and bulk density of the new layer, with the hydrostatic pressure subtracted.

The updated pore pressures were used as inputs to SUTRA as initial conditions to perform transient fluid flow simulations. Once the pore pressures (P) at the end of each loading step were calculated by SUTRA, they were transferred back into the loading program, in which effective stress was calculated using Equation 7. If effective stress increased relative to the previous loading step, the porosity decrease was determined using an iterative method to solve Equation 10 for change in porosity. Vertical spacing

was reduced to maintain constant solid volume and to ensure mass balance (Eq. 11). The new porosity values were then used to calculate the matrix compressibility for the next sedimentation step (Eq. 12). SUTRA was modified to calculate specific storage for each node based on the compressibility and porosity calculated by the loading program.

Model Dimensions, Boundary Conditions, and Initial Conditions

The geometry and hydrogeology of the Nankai accretionary complex were simplified into three hydrogeologic units including the turbidites, upper Shikoku and lower Shikoku Basin hemipelagic sequences. The model domain was discretized into 200 rows. Because the model is one-dimensional, lateral flow along the décollement could not be simulated and thus, special physical properties such as higher permeabilities were not assigned to the décollement.

The upper and lower Shikoku Basin layers were assigned similar porosity and permeability parameters as the two layers were mainly composed of hemipelagic muds. The physical properties for hemipelagic units were assigned based on geological observations and laboratory measurements. The lithology of the turbidite unit at Nankai is composed of a variety of thick to thin bedded sand and silt turbidites with some hemipelagic muds (Shipboard Scientific Party, 2001). Values of n_o (0.77) and b ($1.1 \times 10^{-3} \text{ m}^{-1}$) for hemipelagic sediments were obtained from Screamton et al. (2002) while for turbidites ($n_o=0.65$, $b = 7 \times 10^{-4} \text{ m}^{-1}$), the porosity-depth relationship of Bekins and Dreiss (1992) was used. To test the sensitivity of the b coefficient for hemipelagic sediments, I used the porosity data from Site 1173 to estimate the standard deviation for the b values as $3 \times 10^{-4} \text{ m}^{-1}$. Using the standard deviation, I checked the sensitivity of b values at the minimum possible value of $1.4 \times 10^{-3} \text{ m}^{-1}$ and a maximum possible value of $8 \times 10^{-4} \text{ m}^{-1}$. For the turbidites, I used b values of $1.0 \times 10^{-3} \text{ m}^{-1}$ and $4 \times 10^{-4} \text{ m}^{-1}$ as the maximum and

minimum based on the b values used by Bekins and Dreiss (1992). The estimated λ^* values were only increased by 0.04 at the maximum b value while λ^* values decreased by the same amount at the minimum b value, suggesting the sensitivity to the b value is small.

The permeability-porosity relationship for the hemipelagic sediments was obtained from the laboratory permeability measurements (Equation 3). Generally, the sandy portions of the turbidites would be expected to have higher permeabilities than the hemipelagic sediments. However, because the lowest permeability layer generally controls vertical fluid flow (e.g., Bear and Verruijt, 1987), I used the same permeability-porosity relationship for both turbidites and hemipelagics. I examined the effects of the permeability-porosity relationship by varying the log (k_0) value for both hemipelagics and turbidites during the sensitivity analyses.

The top boundary of the model was set as hydrostatic to simulate the effect of the water column above the complex. I assume that the hydraulic connection between the sediments and the oceanic crust is low due to an ash layer that would be expected to alter to low-permeability clays (Saffer and Bekins, 1998). Thus, permeability of 10^{-23} m^2 was assigned to all elements below the lower Shikoku basin facies. The ocean crust consisted of sufficient rows at the beginning of the simulation so that only “ocean crust” rows would be dropped from the base of the model as the sediment layers are added, to maintain a constant number of elements throughout the simulation. Matrix compressibility of the ocean crust was set at $1.0 \times 10^{-11} \text{ Pa}^{-1}$.

To approximate the effects of in situ temperature on viscosity, I applied temperature and heat flow boundary conditions, and used SUTRA to calculate

temperature distribution. Both the seafloor and oceanic crust boundaries were treated as specified temperature boundaries. The seafloor boundary was set at 2°C while the heat flow at the base of the model was assigned to produce temperatures consistent with those obtained from shipboard measurements. Thermal conductivities and specific heat values for both fluid and solid matrix are given in Table 3-2. SUTRA then calculated fluid viscosity as a function of temperature using the following relationship (Voss, 1984)

$$\mu(T) \approx (239.4 * 10^{-7}) 10^{\left(\frac{248.37}{T+133.15}\right)} \quad (13)$$

where μ is pore fluid viscosity [$\text{kg m}^{-1} \text{s}^{-1}$] and T is temperature in °C.

Table 3-2. Fluid and solid matrix properties used for numerical simulations.

Parameter	Value
Fluid compressibility [Pa^{-1}]	4.40E ⁻¹⁰
Fluid density [kg m^{-3}]	1035
Fluid specific heat [$\text{J kg}^{-1} \text{°C}^{-1}$]	4180
Fluid thermal conductivity [$\text{J s}^{-1} \text{m}^{-1} \text{°C}^{-1}$]	0.7
Solid grain density [kg m^{-3}]	2650
Solid grain specific heat [$\text{J kg}^{-1} \text{°C}^{-1}$]	1000
Solid grain thermal conductivity [$\text{J s}^{-1} \text{m}^{-1} \text{°C}^{-1}$]	3.0

Sedimentation and Prism Thickening Rates

Sedimentation seaward of the deformation front and loading due to the over-riding prism were applied separately in two different phases (Table 3-3). During phase one, sedimentation rates calculated from the biostratigraphy were used to build the sediment columns at Sites 808, 1174, and 1173. At Site 808 and 1174, the sediment columns were built using 137 time steps of 100,000 years and at Site 1173, 140 time steps were used. The average initial sedimentation rate for each unit was based on the initial thickness of that unit and its corresponding deposition time as provided by the Shipboard Scientific Party (2001). The initial thickness of each unit (i.e., the thickness of the sediment layer prior to consolidation) was calculated based on an assumed initial porosity of 0.77 and

0.65 for hemipelagics and turbidites respectively, and a final porosity based on core measurements of shipboard porosity (Shipboard Scientific Party, 2001). During phase two, prism thickening rates for Sites 1174 and 808 were calculated using change in prism thickness and a convergence rate of 4 cm/yr. The convergence rate was used to calculate the time needed for the incoming sediments to underthrust to Sites 1174 and 808. In phase two, each stress step was 50,000 years, and Site 1174 was loaded for 6 stress steps while Site 808 was loaded for 7 stress steps.

Table 3-3. Summary of sedimentation rates calculated from biostratigraphy at Sites 1173, 1174 and 808 and prism thickening rates calculated from prism geometry and convergence rate.

Site	Unit	Thickness (m)	Time (Ma)	Vertical loading	
				Initial sedimentation rate (m/yr)	Prism thickening rate (m/yr)
1173	Turbidites	120	Present-0.25	5.07×10^{-4}	
	upper Shikoku	220	0.25-2.85	7.42×10^{-5}	
	lower Shikoku	50	2.85-3.75	1.21×10^{-4}	
	Proto-décollement	25	3.75-4.95	4.55×10^{-5}	
	lower Shikoku	290	4.95-14.00	8.08×10^{-5}	
1174	Turbidites	420	Present-0.30		1.9×10^{-3}
	Trench-wedge facies	50	0.3-0.90	1.91×10^{-4}	
	upper Shikoku	190	0.90-2.5	2.61×10^{-4}	
	lower Shikoku	149	2.5-6.25	1.12×10^{-4}	
	Décollement	25	6.25-7.15	7.85×10^{-5}	
	lower Shikoku	256	7.15-14.30	1.20×10^{-4}	
808	Turbidites	550	Present-0.35		3.6×10^{-3}
	Trench-wedge facies	75	0.35-0.95	4.28×10^{-4}	
	upper Shikoku	188	0.95-2.85	2.20×10^{-4}	
	lower Shikoku	125	2.85-5.35	1.46×10^{-4}	
	Décollement	25	5.35-6.35	7.30×10^{-5}	
	lower Shikoku	265	6.35-14.35	1.03×10^{-4}	

Results

Model Results

Results of the base run using the one-dimensional loading and fluid flow model are summarized in Table 3-4. For the base run, values of k_0 and ϕ were assigned according

to the permeability-porosity relationship determined from laboratory measurements (Equation 3). The simulated porosity profiles at all three sites decrease smoothly with depth in the lower Shikoku Basin facies. At Site 1173, the simulated porosity profile indicates a small overestimate of porosities compared to the observed porosity profile (Figure 3-5). This reflects that Site 1173 is slightly overpressured ($\lambda^* = 0.04$) in the simulation (Figure 3-5), whereas the porosity-depth relationship assumed hydrostatic conditions at Site 1173 (Screaton et al., 2002). This would imply that λ^* estimated based on the assigned b value would be an underestimate.

It should be noted that results of Screaton et al. (2002) and Saffer (2003) make a similar assumption of hydrostatic conditions at Site 1173. As a result, their pore pressure results may also underestimate actual pore pressure ratios. At both Sites 1174 and 808, the simulated porosities reasonably match the observed porosities above the décollement while underestimating the porosities below the décollement (Figure 3-6). The estimated λ^* values below the décollement at Site 1173 slightly increase with depth while at Sites 1174 and 808, λ^* values slightly decrease with depth below the décollement. Simulated excess pore pressure ratios, λ^* , observed at 15 meters below the décollement increase landward from 0.04 at Site 1173, to 0.14 and 0.22 at Sites 1174 and 808 respectively (Figure 3-5 and Figure 3-6), but are less than that inferred by Screaton et al. (2002) and Saffer (2003). Thus, using the permeability-porosity relationship from Equation 3, the simulations suggest that sedimentation and prism loading alone is not sufficient to generate excess pore pressures as large as predicted from previous studies.

Table 3-4. Summary of simulation runs at Site 1174 and 808. Values of λ^* and porosity for each simulation are given at 15 m below the décollement (855 mbsf at Site 1174 and 979 mbsf at Site 808). At these depths, shipboard measurements indicate porosities of 0.37 at Site 1174 and 0.36 at Site 808 (Shipboard Scientific Party, 1991; 2001). Italics indicate parameters that were changed from the base run.

Run	Unit	$\log(k_0)$	φ	Lat- eral Stress Ratio	10-m Low k Barrier (m^2)	Site 1174 λ^*	Site 1174 n	Site 808 λ^*	Site 808 n
Base run	Turbidites Hemipelagics	-19.82 -19.82	5.39 5.39	0	NA	0.14	0.31	0.20	0.28
Saffer and Bekins (1998)	Turbidites Hemipelagics	-20.00 -20.00	5.25 5.25	0	NA	0.20	0.33	0.31	0.33
Raise turbidite k	Turbidites Hemipelagics	<i>-16.82</i> -19.82	5.39 5.39	0	NA	0.10	0.30	0.15	0.28
Raise bulk k	Turbidites Hemipelagics	<i>-18.82</i> -18.82	5.39 5.39	0	NA	0.06	0.29	0.10	0.25
Lower bulk k	Turbidites Hemipelagics	-20.82 <i>-20.82</i>	5.39 5.39	0	NA	0.47	0.45	0.47	0.42
Lower bulk k	Turbidites Hemipelagics	<i>-20.15</i> -20.15	5.39 5.39	0	NA	0.23	0.34	0.29	0.32
Vary lat.stress	Turbidites Hemipelagics	-19.82 19.82	5.39 5.39	<i>0.1</i>	NA	0.13	0.31	0.20	0.29
Vary lat.stress	Turbidites Hemipelagics	-19.82 19.82	5.39 5.39	<i>0.3</i>	NA	0.15	0.31	0.21	0.29
Vary lat.stress	Turbidites Hemipelagics	-19.82 -19.82	5.39 5.39	<i>0.5</i>	NA	0.18	0.32	0.23	0.30
Vary lat.stress	Turbidites Hemipelagics	-19.82 -19.82	5.39 5.39	<i>0.7</i>	NA	0.21	0.32	0.26	0.30
Vary lat.stress	Turbidites Hemipelagics	-19.82 -19.82	5.39 5.39	<i>0.9</i>	NA	0.24	0.32	0.29	0.31
Lower bulk k + lat stress	Turbidites Hemipelagics	<i>-20.15</i> -20.15	5.39 5.39	<i>0.3</i>	NA	0.26	0.35	0.32	0.34
Low k barrier	Turbidites Hemipelagics	-19.82 -19.82	5.39 5.39	0	10^{-19}	0.15	0.31	0.21	0.29
Low k barrier	Turbidites Hemipelagics	-19.82 -19.82	5.39 5.39	0	10^{-20}	0.28	0.35	0.34	0.32
Low k barrier	Turbidites Hemipelagics	-19.82 -19.82	5.39 5.39	0	10^{-21}	0.45	0.40	0.52	0.39

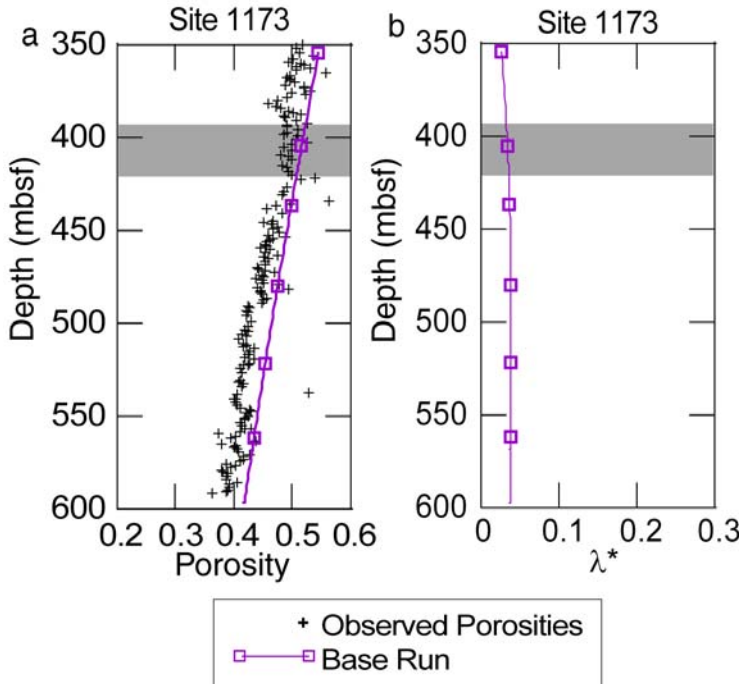


Figure 3-5. Simulated porosity and λ^* profiles for base run at Site 1173. A) Comparison of observed porosity to simulated porosity at Site 1173. B) Simulated λ^* profile at Site 1173. Shading represents the age-equivalent level of Site 1174 décollement zone.

Sensitivity to Bulk Permeability

Because sediment permeability is the most important factor that controls modeled pore pressures (Saffer and Bekins, 1998), here I conducted a sensitivity analysis to test its effects on porosities and excess pore pressures. Bulk permeabilities of hemipelagics and turbidites were changed separately. Results indicate that simulated λ^* values were not very sensitive to an increase in turbidite permeability. For example, when turbidite permeability was increased 3 orders of magnitude by changing $\log(k_0)$ from -19.82 to -16.82, the simulated λ^* decreased by only 0.05 at Site 808 and by 0.04 at Sites 1174 (Figure 3-6).

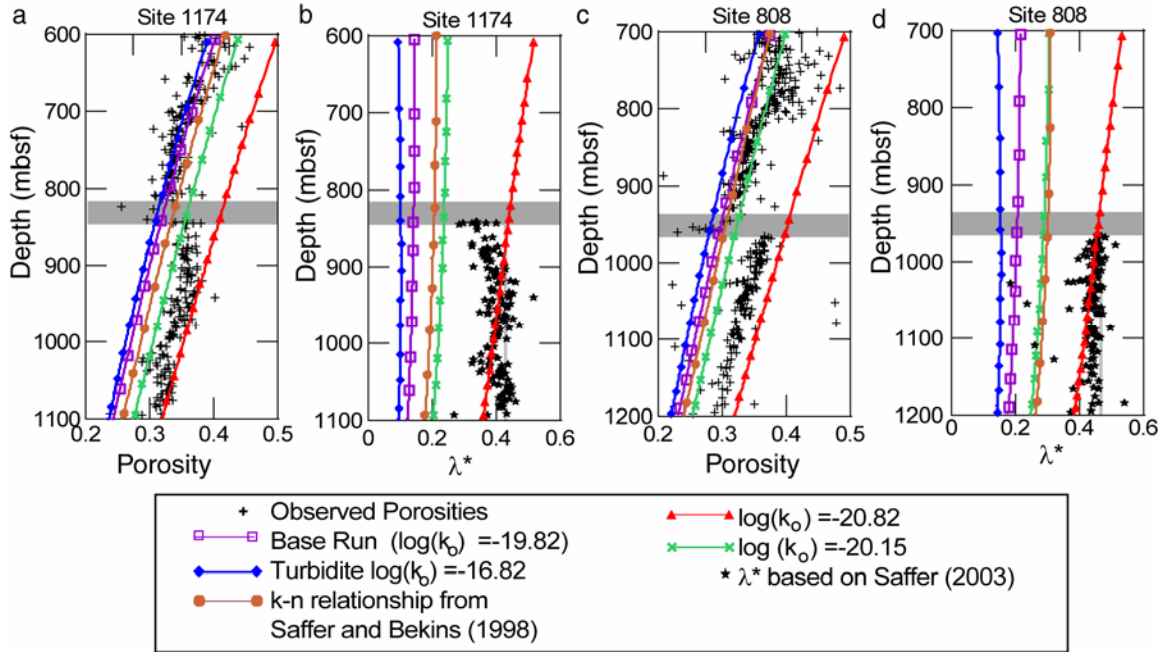


Figure 3-6. Simulated porosity and λ^* profiles with varying bulk permeability at Sites 1174 and 808. A & C) Comparison of observed porosity to simulated porosity at Sites 1174 and 808. B & D) Simulated λ^* profiles at Sites 1174 and 808. Shading represents the décollement zone. The λ^* values estimated by Saffer (2003) were based on LWD (Site 1174) and Shipboard data (Site 808). Vertical lines represents estimate by Scream et al. (2002).

When the bulk permeability of both turbidites and hemipelagics was lowered by an order of magnitude (from $\log(k_0) = -19.82$ to -20.82) the pore pressures below the décollement significantly increased compared to the base run (Table 3-4, Figure 3-6). The simulated λ^* values reached above 0.45 at both Sites 808 and 1174 and the simulated porosities above and below the décollement were overestimated compared to the observed porosity values (Figures 3-6). As bulk permeability was lowered, the steepness of the slope of the λ^* profile gradually increased (Figure 3-6).

The λ^* profile for $\log(k_0) = -20.15$ represents the relationship shown in Figure 3-4 for the lower range of permeability values. The λ^* profile of this simulation shows higher values for λ^* compared to the results obtained for the base run. The estimated porosities

below the décollement at both sites were less than observed values. The simulated porosities above the décollement were higher at Site 1174 than observed, while at Site 808 they reasonably matched the observed porosities.

I also examined the sensitivity of porosity and λ^* to a permeability relationship ($k=20+5.25n$) in the range used by Saffer and Bekins (1998) (Table 3-4, Figure 3-6). The simulated λ^* values using this relationship predicts greater λ^* values than those predicted from the base run suggesting that simulated λ^* values are very sensitive to even slight changes in the log-linear permeability-porosity relationship (Eq. 2). The predicted λ^* using this relationship were greater by 0.06 (Site 1174) and 0.11 (Site 808) compared to the λ^* values predicted from the base run (Table 3-4).

In comparison to the λ^* profile of Saffer (2003), the values of λ^* predicted for $\log(k_0) = -20.82$ is in the same range as the λ^* values predicted by Saffer (2003). The general trend of the λ^* profile matches values predicted by Saffer (2003) best in the upper (Site 808) and mid (Site 1174) portions of the underthrust and with depth the λ^* profile gradually deviates to lower values than predicted by Saffer (2003).

Sensitivity to Lateral Stress

In reality, the prism sediments are structurally deformed by lateral stresses caused by tectonic compression. To examine the effects of tectonic compression on excess pore pressures and porosities, I included lateral stress within the prism sediments as an additional fraction of the vertical loading (Jaeger and Cook, 1969). Following Domenico and Schwartz (1998) the ratio of horizontal to vertical stress becomes greater than one in areas of tectonic compression. I varied the lateral stress factor from 0.1 to 0.9 (i.e., the

total stress at any point in the prism was assumed to be 1.1 to 1.9 times the vertical stress, Table 3-4).

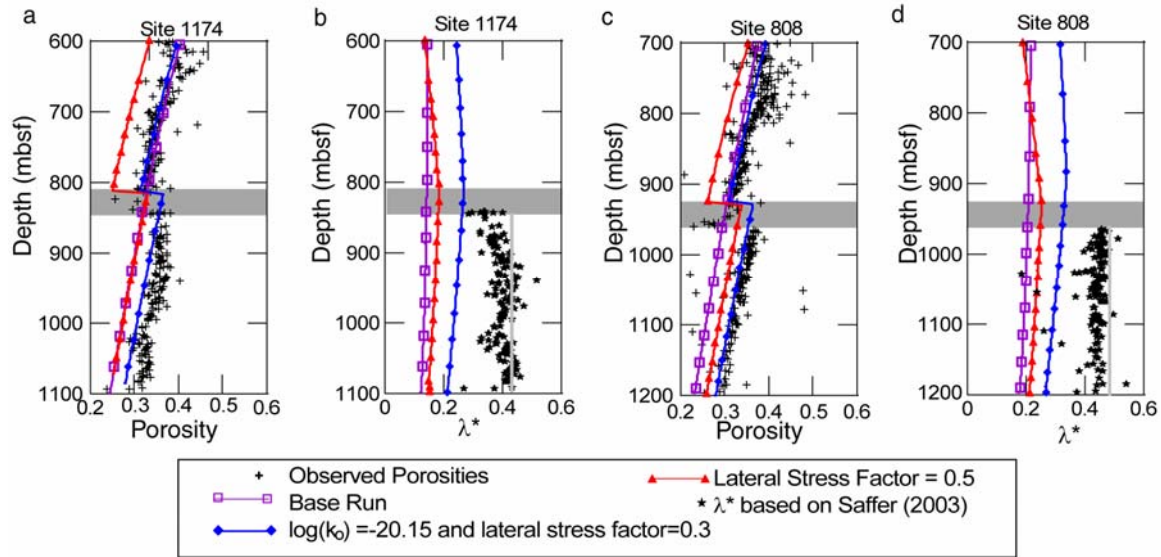


Figure 3-7. Simulated porosity and λ^* profiles with added lateral stress at Sites 1174 and 808. A & C) Comparison of observed porosity to simulated porosity at Sites 1174 and 808. B & D) Simulated λ^* profiles at Sites 1174 and 808. Shading represents the décollement zone. The λ^* values estimated by Saffer (2003) were based on LWD (Site 1174) and Shipboard data (Site 808). Vertical lines represents estimate by Scream et al. (2002).

When lateral stress was added to the prism sediments, the porosities smoothly decreased with depth above the décollement, and abruptly increased to a maximum at the décollement (Figure 3-7). Below the décollement, the porosities gradually decreased with depth. The sharp change in porosity at the décollement is due to the added lateral stress increasing effective stress and lowering porosities within the prism sediments. The simulated λ^* values with added lateral stress show a gradual increase of pore pressures above the décollement while reaching the maximum λ^* within the décollement (Figure 3-7). Below the décollement, λ^* values gradually decreased with depth.

Even though lateral stress is added only in the prism, the λ^* values beneath the prism increased because the vertical fluid flow from the underthrust is restricted by the

elevated pressures within the prism. Thus, when the lateral stress was increased, both λ^* and porosity values were slightly increased below the prism (Table 3-4). However, the effect of prism lateral stress on pore pressures in the underthrust is relatively small compared to the sensitivity to bulk permeability. Although it may be possible to have greater values of the lateral stress factor than 0.9, simulations suggest that they would have little additional affect on pore pressures in the underthrust sediments.

Increasing the lateral stress factor results in a greater offset in porosity across the décollement zone. For example, the simulated porosity profile with a lateral stress factor of 0.5 underestimated observed porosity values both above and below the décollement (Figure 3-7). Raising the lateral stress factor increases porosities in the underthrust sediments (Table 3-4), yielding a better match to observed, but decreases porosities in the prism, yielding a poorer match. Thus, by itself, changing lateral stress (with the porosity-permeability relationship obtained in this study) cannot generate porosities that matched observed porosities.

When lateral stress was combined with lower bulk permeability, the pore pressures were significantly increased with respect to lateral stress alone. For example, when the bulk permeability of the hemipelagic sediments were lowered to a log (k_0) of -20.15 (the lower boundary to permeability data in Figure 3-4) with a lateral stress factor of 0.3, the λ^* at 15 m below the décollement at Site 808 reached 0.32. The simulated porosity profile for this combination well matched the observed porosity profile above the décollement while the porosities below the décollement were very slightly underestimated at both Sites 808 and 1174 (Figure 3-7).

Sensitivity to a Low-Permeability Barrier

Previous accretionary complex studies have suggested the idea of a low-permeability barrier at the décollement as a possible cause of excess pore pressures. For example, at the Barbados accretionary prism, Bekins et al. (1995) simulated a 15-m thick low-permeability cap above the top of the décollement based on an anomalously low permeability value ($6.5 \times 10^{-21} \text{ m}^2$) measured by Taylor and Leonard (1990). In a more recent study based on inferred porosity variations obtained from inverted seismic reflection data at Nankai, Bangs and Gulick (2005) argued that consolidation of the uppermost lower Shikoku Basin strata forms a barrier blocking the fluid flow from below. Because the barrier lies just above the projected level of the décollement, they suggest that higher-porosity, underconsolidated, and overpressured sediment below forms a surface of potential décollement propagation.

To test the effects of a low-permeability barrier at the décollement at Nankai, I ran simulations with a 10-m thick low-permeability barrier above the top of the décollement zone. This barrier was implemented after the initial sedimentation steps and prior to the loading by the prism (Table 3-4). As expected, when the low-permeability was added, the λ^* values below the barrier abruptly increased to a maximum because the fluids in the underthrust could not migrate through the barrier fast enough to keep pace with loading. The simulated λ^* values at both Sites 1174 and 808 gradually decrease with depth below the décollement (Figure 3-8).

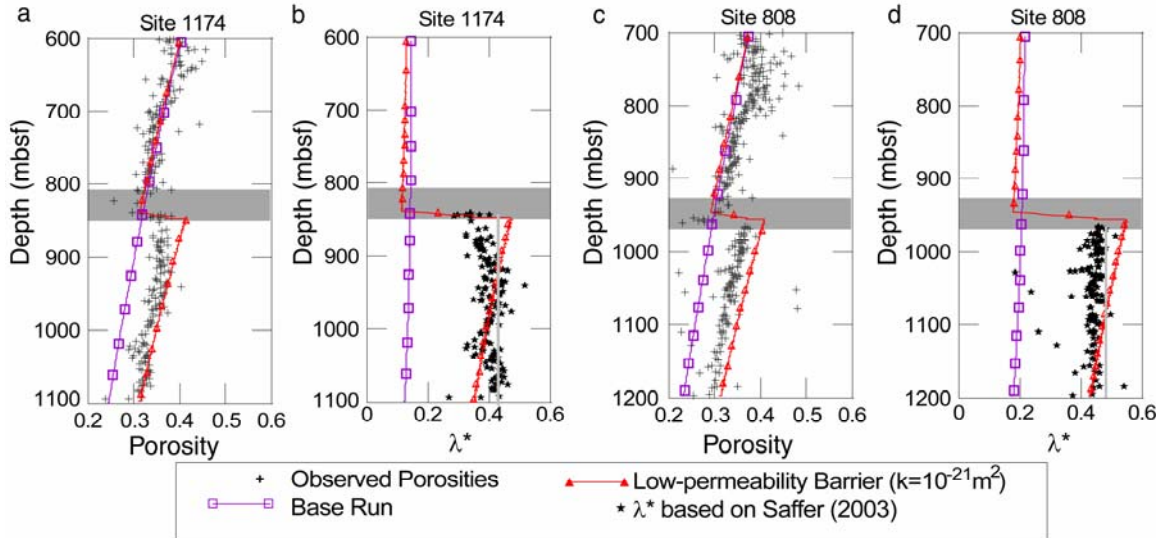


Figure 3-8. Simulated porosity and λ^* profiles with added low-permeability barrier at Sites 1174 and 808. A & C) Comparison of observed porosity to simulated porosity at Sites 1174 and 808. B & D) Simulated λ^* profiles at Sites 1174 and 808. Shading represents the décollement zone. The λ^* values estimated by Saffer (2003) were based on LWD (Site 1174) and Shipboard data (Site 808). Vertical lines represents estimate by Screamton et al. (2002).

The simulated porosities smoothly decrease both above and below the décollement while reaching a maximum at the décollement (Figure 3-8). The porosity profiles generated by the low-permeability barrier with a permeability of $1 \times 10^{-21} \text{ m}^2$ were slightly higher below the décollement at both Sites 808 and 1174 than the observed porosities. Above the décollement, the porosities closely matched the observed values at Site 1174 while slightly underestimating the observed values at Site 808. The simulated λ^* values at both sites were similar to the values presented by Screamton et al. (2002). In comparison to the λ^* profile of Saffer (2003), the values of λ^* predicted for the low-permeability barrier is roughly in the same range as those predicted by Saffer (2003). However, the general trend of the λ^* profile of the low-permeability barrier is different from that of Saffer (2003). The low-permeability barrier predicts a sharp decrease in

λ^* with increasing depth while the profile of Saffer (2003) predicts a gradual decrease of λ^* with increasing depth.

Although modeling results indicate high λ^* values at and below the décollement due to the added low-permeability barrier, core samples immediately above the décollement are not available for laboratory-measurements to assess the presence of a low-permeability barrier. Although I do not have any independent evidence suggesting that the permeability is low in the direction perpendicular to the plane of décollement, previous studies have suggested the formation of a low-permeability barrier during the accretionary process due to shearing of sediments below the wedge as it moves above the underthrust sediments. For example, Maltman et al., (1992) suggested that at the Nankai accretionary complex, high stresses at the depth of the décollement could seal fractures lowering its permeability despite the presence of highly brecciated and fractured material. This idea is further strengthened by lack of evidence for fluid flow such as veins, mineralized surfaces or clastic dykes at the décollement (Maltman et al., 1992). If a low-permeability barrier does exist, then it is more likely to form at the base of the wedge where the high shearing is present increasing the pore pressures below the barrier. The presence of a low-permeability barrier is likely to generate excess pore pressures below the barrier, as shown in Figure 3-8.

The affects of lateral fluid flow on pore pressures are difficult to predict. Lateral fluid flow could allow pore pressures to be lowered, if fluids can escape to the seafloor near the toe of the prism. However, if the décollement transmits fluids to near the toe of the prism, and these fluids cannot escape, pore pressures will be increased at the updip end of the lateral flow path. Lateral fluid flow within the décollement could decrease the

significance of the low-permeability barrier, if fluid could escape along the décollement zone. Similarly, lateral fluid escape along the décollement may decrease the impact of lateral stresses within the prism on λ^* values within the underthrust sediments. Because the décollement has been speculated as a possible, yet controversial, pathway for lateral flow it will be valuable to address in future investigations.

Implications

Both simulations using the added lateral stress and low-permeability barrier show a sharp increase in λ^* near the décollement zone at both Sites 1174 and 808 (Figure 3-7 and Figure 3-8). However, each scenario generated a distinct λ^* profile. The λ^* profile generated by the added lateral stress demonstrate a gradual increase in pore pressures both above and below the décollement, and the λ^* value peak at the décollement. The maximum λ^* corresponds to the maximum simulated porosity found near the top of the décollement zone (Figure 3-7). In contrast, the λ^* profile generated by the low-permeability barrier shows an abrupt increase of pore pressures at the lower part of the décollement. Above the décollement, the λ^* profile shows a very slight decrease with depth while below the décollement λ^* decreases more gradually. As observed in both scenarios, the maximum λ^* is located near the décollement, consistent with previous inferences (e.g., Hubbert and Rubey, 1959) that pore fluid pressures play a major role in the mechanics of thrust faulting.

The excess pore pressures observed near the décollement can also be related to the sliding of the décollement as proposed by the critical wedge theory (Davis et al., 1983). Critical wedge theory predicts that pore pressures significantly greater than hydrostatic are needed to maintain small taper angles such as at the Muroto Transect of Nankai.

Generally a small critical taper is an indication of very little basal friction, due either to low intrinsic strength or elevated pore pressures, or that the wedge consists of a strong material, which need not deform for stable sliding to occur (Davis et al., 1983). Thus, it can be speculated the maximum λ^* values observed in the profiles at the décollement could represent the level of least mechanical resistant that promotes stable sliding. It is possible that a permeability barrier would also affect fault zone initiation, if elevated pore pressures are transmitted seaward of the deformation front. A two-dimensional model would be needed to fully examine this possibility.

Many previous studies based on the critical taper theory have assumed the pore pressure ratios (pore fluid pressure/lithostatic pressure) at the base of the wedge and within the wedge to be equal. The results from simulations with the low-permeability barrier demonstrate a mechanism for basal pore pressure ratios to be significantly greater than those in the wedge which could increase taper angle for a given basal pore pressure. Lateral stresses in the prism may also result in basal pore pressure ratios to be higher than in the wedge, but the difference is not as great as with the low-permeability barrier.

Conclusions

I examined the effects of different parameters on excess pore pressures at the toe of the Nankai accretionary complex. Using a permeability-porosity relationship based on a best fit to laboratory data, simulations suggest that sedimentation and prism thickening generate excess pore pressures, but not as high as predicted from previous studies. Results from this study demonstrated significant increase in pore pressures at the décollement with lower bulk permeability, such as obtained by using the lower boundary of permeability-porosity data. Because the lowest permeabilities generally control

vertical flow, this relationship may be more appropriate for the simulations than the best fit equation. However, if the high excess pore pressures suggested by Screamton et al. (2002) or Saffer (2003) are correct, permeabilities must be even lower, requiring either a bulk permeability represented by $\log(k_0) = -20.82$, a low permeability ($<10^{-20} \text{ m}^2$) barrier above the décollement, or a combination of lower bulk permeability and permeability barrier. Alternatively, other factors must contribute, such as recent prism growth rates greater than the time-averaged rates simulated here.

The magnitude of pore pressures in the underthrust sediments demonstrated only slight sensitivity to added lateral stresses in the prism, although the profile of the pore pressure ratio is affected. Results further illustrated that the simulations with low-permeability barrier and lateral stress both produced a sharp increase in porosities below the décollement zone, as is observed in the measured values. Furthermore, in both scenarios, maximum excess pore pressure ratios were found at the décollement, which could contribute to stable sliding of the décollement zone.

CHAPTER 4

EVOLUTION OF HIGH PORE PRESSURES AND IMPLICATIONS FOR EPISODIC FLUID FLOW AT THE NORTHERN BARBADOS ACCRETIONARY COMPLEX

Introduction

Variations in fluid flow pressures and its distribution within subduction zones regulate the mode of deformation, affecting the evolution of the accretionary complex. It has been speculated that excess pore pressures play a major role in the mechanics of thrust faulting (Hubbert and Rubey, 1959), thus, allowing the weak semilithified sediments in accretionary complexes to glide over the subducting plate along a low-angle detachment surface (Davis et al., 1983). Excess pore fluid pressures are also responsible for increasing sediment permeability associated with reduction in effective stress (Yeung et al., 1993; Fisher and Zwart, 1996). In addition, pore pressure has been claimed to influence seismogenic faulting, through its control on effective stress and consolidation state (e.g., Moore and Saffer, 2001; Scholz, 1998). Thus, an understanding of the development of excess pore pressures will provide valuable insight to the evolution of accretionary complexes as well as to subduction zone processes such as fault mechanics.

The abundant evidence for excess pore pressures at Barbados accretionary complex provides an excellent opportunity for the study of evolution of pore pressure generation. The distribution of mud volcanoes (Gretener, 1976) and the overall shape of the accretionary prism (Davis et al, 1983) suggest the existence of excess pore pressures at the Barbados accretionary complex. In addition, elevated pore fluid pressures have been inferred at the Barbados accretionary complex from fluid flow modeling (e.g., Shi and

Wang, 1988; Screamton et al., 1997; Bekins et al., 1995; Henry, 2000) and direct borehole measurements along the décollement (Foucher et al., 1997; Becker et al., 1997).

Studies have speculated that fault zones play a major role in focusing fluid expulsion (e.g., Bekins et al., 1995; Moore et al., 1998; Henry, 2000). Indirect evidence for transient fluid flow along the décollement is provided by geochemical and thermal anomalies (e.g., Bekins et al., 1995; Fisher and Hounslow, 1990). A widely held hypothesis relating elevated pore pressures and evidence for fluid flow is that flow must be episodic, although the mechanisms producing the episodic fluid flow events are not fully understood. Field evidence for episodic fluid flow includes the presence of multiple episodes of fracturing and vein filling in accreted sediments (Labaume et al., 1997). However, the time scales of these events are difficult to estimate (Knipe et al., 1991).

Several mechanisms have been put forward to explain the time-variable permeability in the fault zone. One mechanism is that the permeability in the décollement is enhanced by the episodic opening of horizontal hydrofractures when pore pressures reach values above lithostatic (e.g., Behrmann, 1991; Moore and Vrolijk, 1992; Brown et al., 1994). Similarly, numerical modeling by Bekins et al. (1995) predicted results with observed chloride anomalies within the décollement of the Barbados accretionary complex by assuming an instantaneous permeability increase within the décollement. Another mechanism for episodic fluid flow is based on in situ bulk permeability measurements that were made at a variety of fluid pressure conditions. According to Fisher and Zwart (1996), this relationship between bulk permeability and effective stress may explain the dynamics of fluid-fault interactions and the transient nature of hydrologic processes at convergent margins. Additional hydrologic tests that

were conducted at a sealed borehole penetrating the décollement at the Barbados accretionary complex support the conclusion by Fisher and Zwart (1996) that significant permeability increase can occur within the décollement at pore pressures below lithostatic pressures (Screaton et al., 1997). Studies based on fluid budgets shows that fluid flux varies with both arcward distance and through time (Saffer and Bekins, 1999). In addition, fluid budget studies suggest that initiation of connected flow conduits is delayed with respect to the time of accretion and may be related to burial below a critical depth, where channelized fluid escape is more efficient than diffuse flow to the sea floor or where sediments may behave brittlely (Saffer and Bekins, 1999). Even though previous modeling studies have investigated the production of overpressures, these models did not indicate when the overpressures are generated in the evolution of the complex and thus, the connectivity between excess pore pressures and episodic fluid flow is not well understood. Models used by Henry and Wang (1991), Shi and Wang (1994), and Stauffer and Bekins (2001) focused on processes that take place at the toe of the prism during initial offscraping. Bekins et al. (1995) focused on steady-state pore pressures and transient fluid flow assuming instantaneous décollement permeability after the entire prism had grown. However, to fully understand the development of pore pressures and thus, hypothesized episodic fluid flow, one should examine the development of pore pressures both at the toe and deeper parts of the accretionary complex through both space and time. Thus, in this study I modeled 50 km of the accretionary complex as a time-dependent evolving prism. A combined prism growth and fluid flow model was used to examine the development of pore pressures. Mechanisms for episodic fluid flow were examined during the evolution of the accretionary complex by including hydrofracture or

a décollement with varying permeability based on a relationship of bulk permeability - vertical effective stress.

Background

The Barbados accretionary complex is located in the Caribbean where the Atlantic Plate (Figure 4-1) is being subducted beneath the Caribbean Plate at a rate of 2 cm/yr in an east-west direction (DeMets et al., 1990). At Barbados, active accretion of sediments takes place at the eastward end of the complex as the more stabilized portion lies westward, where the complex is partially exposed above sea level at the Barbados Island (Figure 4-1). The complex varies in thickness from 200 km south of Tiburon Rise at 14°N, to approximately 10 km north of Tiburon Rise at 16°N (Bangs and Westbrook, 1991). The variation in thickness of the complex is related to the distance from the terrigenous sediment source from South America (Underwood and Deng, 1997), as well as the affect of local barriers such as the Tiburon Rise (Figure 4-1), which slows the influx to the complex.

The northern Barbados accretionary complex is rich in hemipelagic sediments (Bekins et al., 1995), whereas the southern part is dominated by turbidites (Langseth et al., 1990). The age of the sediments at the Barbados accretionary complex varies from Late Eocene to Late Cretaceous (Underwood and Deng, 1997). Mud volcanoes and mud diapirs, which indicate excess pore pressures, are abundant in the southern part of the complex where the sediment sequence is thicker (Moore et al., 1982).

Based on seismic reflection images the décollement was estimated to be ~14 m thick at the northern Barbados accretionary complex (Shipley et al., 1994). It was inferred as a high-porosity zone with undercompacted sediments and high-fluid pressures

(Moore et al., 1995). During Deep Sea Drilling Project (DSDP), Leg 78A high pore pressures were encountered at the toe of the northern Barbados accretionary complex while attempting to drill through the décollement (Biju-Duval et al., 1984). The seismic profiles show prism sediments being subjected to high lateral strain while sediments in the underthrust remain undeformed (e.g., Westbrook et al., 1988), possibly due to the presence of excess pore pressures on the décollement.

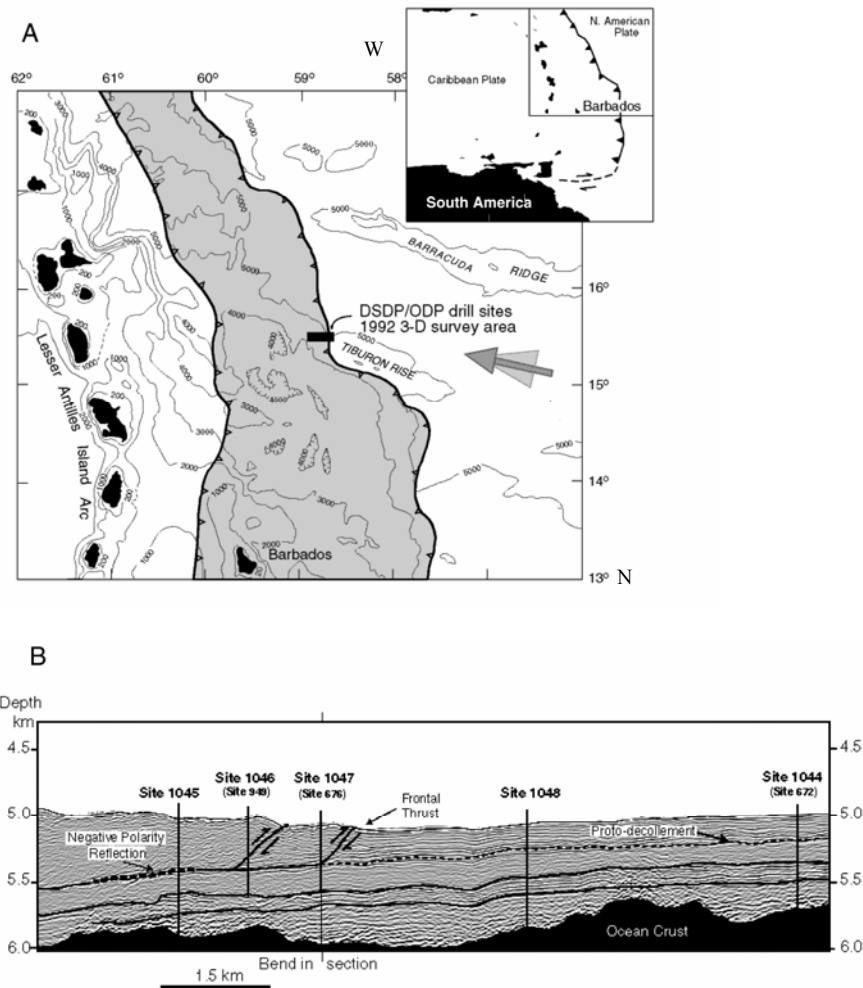


Figure 4-1. Location map and cross-section of the Barbados accretionary complex. A) Map of the eastern Caribbean showing the deformation front. B) Cross-section of the Barbados accretionary complex (Shipboard Scientific Party, 1998).

Ocean Drilling Program (ODP) Leg 110 revisited northern Barbados and three sites were drilled (Sites 671, 672 and 676). Sites 671 and 676 (Figure 4-1) were drilled arcward of the deformation front at a distance of 4.5 km and 0.25 km respectively (Masclé et al., 1988). Site 672 was drilled 6 km east of the deformation front to provide an undeformed reference site (Masclé et al., 1988). The core samples from Leg 110 were analyzed for structural features, chemical signals, permeability, consolidation behavior, and bulk composition. Taylor and Leonard (1990) inferred near-lithostatic pore pressures directly above the proto-décollement zone based on consolidation tests on core samples. In contrast several other studies (e.g., Shi and Wang, 1985; Screamton and Ge, 2000) concluded that sedimentation rates alone were not sufficient to produce excess pore pressures.

During Leg 156 Logging While Drilling (LWD) was performed at Site 948, which coincides with the location of Site 671 (Shipley et al., 1997). Site 949 was drilled 2 km northeast of Site 948 (Shipley et al., 1997). During Leg 156, a hydrologic borehole packer was successfully deployed and fluid flow experiments were conducted at Sites 948 (671) and Site 949 (Leg 171A, Site1046) (Fisher and Zwart, 1996). Results of packer experiments further supports the presence of excess pore pressures at the décollement, although perturbations from drilling and testing were difficult to separate from natural pore pressures. Estimated values for fault zone permeability from in situ packer tests vary from 10^{-12} m^2 when fluid pressure is at lithostatic to 10^{-18} m^2 when fluid pressure is at hydrostatic (Fisher and Zwart, 1996). Results of hydrogeologic tests that were performed at a sealed borehole (949C) penetrating the décollement support the idea

of significant permeability increase within the décollement with increasing pore pressure (Screaton et al., 1997).

Fluid Flow and Pore Pressures

Evidence for fluid flow at the Barbados accretionary complex comes from the presence of low-chloride anomalies observed along the décollement (Kastner et al., 1993). It has been suggested by Bekins et al. (1995) that smectite dehydration is the most likely mechanism for low-chloride anomalies. In contrast, Fitts and Brown (1999) suggested that low-chloride anomalies occur as a result of artificial squeezing of sediments released from smectite interlayers during pore water sampling. However, even after accounting for the effects of sample squeezing process, the low-chloride anomaly is still 12% fresher than seawater (Fitts and Brown, 1999) supporting the clay dehydration as a possible explanation for low-chloride anomalies. The clay dehydration reaction takes place at temperatures between 60-160° C (Perry and Hower, 1970). Based on kinetic modeling of clay dehydration in the Barbados accretionary complex, Bekins et al. (1995) estimated the peak reaction window to be at 50 km arcward of the deformation front. Thus, if the fluid released from smectite dehydration is responsible for the observed low-chloride anomalies at the toe of the prism (Site 948), then pore fluids must migrate over 46 km to reach Site 948 (Bekins et al., 1994).

Heat flow anomalies have also been observed at the Barbados accretionary complex from temperature measurements (Fisher and Hounslow, 1990) and surface heat flow surveys (Foucher et al., 1990). Seafloor heat flow values near the toe of the complex range from 96 to 192 mW m⁻² (Fisher and Hounslow, 1990) and are well above the 53-55 mW m⁻² expected for 90 Ma oceanic lithosphere (Ferguson et al., 1993). One of the possible explanations for the observed heat flow anomalies is fluid flow along the

décollement (Langseth et al., 1990). In contrast, Fisher and Hounslow (1990) and Moore et al. (1998) suggest possible lateral fluid flow along turbidites in the underthrust sequence. Muller and Smith (1993) argued that the uniformly high background heat flow in the ODP drilling area could be due to crustal thinning of the Tiburon Rise. Based on both steady state and transient state models, fluid fluxes needed to explain the observed heat flow anomaly are approximately one order of magnitude higher than the fluxes needed to explain the low-chlorinity anomaly (Henry, 2000). Similarly several other studies (Foucher et al., 1990; Saffer and Bekins 1999; Cutillo et al., 2003; Bekins and Screamton, 2006) have noted that the outflow from the underthrust necessary to create a thermal anomaly (greater than 60 mW m^{-2}) seems excessive compare to the in flow thus, suggesting that the hypothesis on crustal thinning under Tiburon Rise should be further explored.

In addition to low-chloride and heat flow anomalies, the presence of mineralized veins supports the idea of transient fluid flow along the décollement. Mineral veins were found in the upper part of the décollement (Labaume et al., 1997). The orientations of the veins suggest that pore fluids around the fault zones is at near lithostatic pressure during vein formation (Labaume et al., 1997). Veins that were formed during several growth phases reflect the episodicity of fluid flow along the décollement (Labaume et al., 1997).

Bekins et al. (1995) used low chloride anomalies as constraints on a transient model. In their model they raised permeabilities from $10^{-12} - 10^{-15} \text{ m}^2$ along the entire décollement zone to match observed low-chloride anomalies. To justify this, they hypothesized that pressures in the accretionary complex build until it reaches values that

are close to lithostatic. These high pore pressures lower the effective stress along the décollement creating fractures or dilating existing fractures, raising the permeability along the décollement. To simulate this hypothesized scenario based on a steady-state model, they assigned varying values of décollement permeability (k_d) until sublithostatic pressures were simulated. Once the appropriate k_d value was determined they assumed that the pressures estimated from this solution represent those immediately before a slip event that increases k_d and used these pressures as initial conditions in the transient simulation. When décollement permeability was suddenly raised the pore pressures along the décollement reached values that are closer to lithostatic during the first few thousand years supporting the concept of pressure build-up and release cycles or episodic fluid flow.

In another study, Henry (2000) modeled the episodicity of fluid flow in a slightly different manner. In his model he started a pressure pulse at the arcward boundary of the complex and allowed it to propagate along the décollement. The décollement was assigned a permeability that increased continuously as pore pressure increased following the relationship of Fisher and Zwart (1996). Also it is assumed that all fluid flow occurs either along the décollement or along sandy layers at 200 m below the décollement within the underthrust sequence. Thus, a bulk permeability of $3 \times 10^{-13} \text{ m}^2$ is assigned either to the décollement or to the sand layer to simulate fluid flow. According to this simulation, significant fluid flow persists for several thousands to 10,000 years and it is in agreement with a diffusion-advection model of the chlorinity anomaly (Henry, 2000).

Based on long term monitoring at Holes 948D and 949C during ODP Leg 156, the estimated λ^* values (where $\lambda^* = (P - P_h)/(P_l - P_h)$, P = pore pressure, P_h = hydrostatic

pressure and P_l = lithostatic pressure) were 0.50 (Foucher, et al., 1997) and 0.36 (Becker et al, 1997), respectively. These results were similar to those previously obtained using a steady state model with a permeability-depth relation for clay-rich sediments (Bekins et al; 1995). Moreover, the increase of λ^* by 0.15 between Sites 949 and 948 over a lateral distance of 2.2 km was also estimated by Stauffer and Bekins (2001) based on inferred consolidation state.

In addition, constraints for pore pressure distribution also follow from an analysis of the mechanical force balance in accretionary wedges presented by Davis et al. (1983). According to Davis et al. (1983), in order for the sediments of the wedge to move over the underthrust sequence along a low-angle décollement, high pore pressures ($\lambda = 0.92$ for the overall taper, where λ is the ratio of pore fluid pressures to the vertical normal traction exerted by the lithostatic overburden) must be present along the décollement. The presence of lower pressures would result in a steeper taper angle than that observed at Barbados (Bekins et al., 1995).

Hydrofractures

Behrmann (1991) suggested that hydrofracturing enhances permeability in argillaceous rock sequences. According to Behrmann (1991) the capability of rocks to hydrofracture depends on the mode of faulting and the effective mean stress. He also noted that the depth to which hydrofracture could occur is a function of both the faulting mode and the ratio of fluid and lithostatic pressures. Thus, wrench and normal faults hydrofracture even at ratios of fluid and lithostatic pressure is less than one. In contrast thrust faults always require ratio of fluid and lithostatic pressure to be greater than one to hydrofracture. Vertical fluid flow has been indicated by 3 –D seismic images at the

northern Barbados accretionary complex which shows at least 50 m offset in the turbidites along the normal faults extending upward from the basement (Zhao and Moore, 1998) suggesting that vertical hydrofracture could occur in the underthrust. According to Behrmann (1991), the criteria requires λ^* to be > 0.8 for vertical hydrofracturing in soft rocks. Vertical hydrofractures occur perpendicular to the least principle stress axis. According to Price (1975), when sediments hydrofracture, the hydraulic properties are expected to change dramatically.

Modeling Methods

Model Implementation

A model developed by Screamton and Ge (2000) was modified to simulate the effects of subduction beneath a prism. This model builds the accretionary complex in segments through time. The prism growth/flow model consists of two sub programs. The first sub program is a modified loading program (Gamage and Screamton, 2006), which builds the initial sediment column that enters the accretionary complex at the deformation front. The second sub program (prism loading) advances the accretionary complex over the subducting sediments in segments through time at a convergence rate of 2 cm/yr. It is assumed that the taper of the prism is constant. The prism-growth/flow model calculates the time necessary for prism to advance one column by dividing the horizontal dimension of the column by the convergence rate. The vertical dimension is calculated using the prism thickening rates. As the prism advances seaward the loading program adds sediments on each advanced column according to the assigned prism thickening rates. Based on the calculated increase in overburden and sediment properties, the prism-growth/flow model calculates the pore fluid pressures. These pore pressures are then input into SUTRA (Voss, 1984), a finite-element code that simulates transient two-

dimensional fluid and thermal transport. SUTRA simulates the fluid flow and the pore pressure changes with time. Once the pore pressures were calculated in SUTRA they were transferred back into the prism-growth/flow model, which calculates effective stress, porosity, and permeability before beginning the next loading step.

During hydrofracture, the model checks for regions that have reached the criteria for vertical hydrofracture after every seaward advancement of the prism. If pressures meet the vertical hydrofracture criteria, then the model increases vertical permeability from the point of lithostatic pressure up to the décollement. If pressures are less than the assigned criteria for hydrofracture the permeability values are assigned according to permeability-porosity relationship.

SUTRA uses a backwards finite-difference scheme which enhances numerical stability. The large permeability contrast during the introduction of hydrofractures into the model was challenging for the iterative solver, especially for the thermal transport simulations. However, by reducing the contrast between the highest and the lowest permeabilities and increasing upstream weighting for the transport, convergence was obtained.

Model Equations

Combining the mass conservation of fluid with Darcy's law, the following equation can be written for two-dimensional transient flow:

$$\left(K_{xx} \frac{\partial^2 h}{\partial x^2} \right) + \left(K_{yy} \frac{\partial^2 h}{\partial y^2} \right) = S_s \frac{\partial h}{\partial t} + Q \quad (1)$$

where S_s is specific storage [L^{-1}], h is hydraulic head [L], x and y are spatial coordinates, Q is a source term reflecting processes such as loading that affect fluid volume or pressure [T^{-1}]. The left hand side term accounts for fluid flow into and out of a

given element in two dimensions. The right hand side terms account for changes in storage of fluid mass due to change in hydraulic head and addition or removal of fluid or pressure. When initial conditions, boundary conditions and the controlling hydrologic parameters are known, Equation (1) can be solved for head at any point in a two-dimensional field at any given time. The equations present here are changes made to those in Chapter 3. For a complete explanation of the model equations refer to the “Model Equations” in chapter 3.

Model Dimensions, Boundary Conditions, and Initial Conditions

The cross-section model consists of four zones: the upper hemipelagics that form the wedge, the décollement, the turbidites and the underthrust hemipelagic sequence (Figure 4-2). The properties for the four hydrogeologic units were assigned based on geological observations and laboratory measurements. The model domain was discretized into finite element grid consisting 8100 nodes and 7920 quadrilateral elements (Figure 4-2). Horizontally the model extends to a maximum of 50 km arcward of the deformation front during the total simulation time. Vertically the model extends from the seafloor to a maximum depth of 3 km at full growth. At the deformation front the incoming sediment sequence was divided into 470 m of underthrust sediments, 15 m of décollement zone and 173 m of accreted sediments. Values of n_0 (0.7) and b ($8 \times 10^{-4} \text{ m}^{-1}$) for hemipelagic sediments were obtained from Screamton and Ge (1997) while for turbidites ($n_0=0.6$, $b = 7 \times 10^{-4} \text{ m}^{-1}$), the porosity-depth relationship of Bekins and Dreiss (1992) was used. The n_0 and b values used for turbidites were similar to those values used by Screamton and Ge (1997) for Barbados sediments south of Tiburon Rise, as these sediments are rich in turbidites.

Permeability for the hemipelagic units were assigned based on the permeability-porosity relationship used by Bekins et al. (1995) ($\log(k) = -22.0 + 8.44n$). This relationship was based on laboratory permeability measurements of ODP Leg 110 obtained by Taylor and Leonard (1990). Because these permeability measurements only represented samples from less than 500 m of depth, to estimate the permeability-porosity relationship, Bekins et al. (1995) extended the ODP data to depth by visually placing a line, which roughly bisects the outline for argillaceous sediments compiled by Neuzil (1994). Because there were no permeability measurements at lower porosities, the constraints for permeability are limited. Thus, it should be noted that the permeability-porosity relationship predicted by Bekins et al. (1995) might not necessarily represent permeability values at lower porosities. If the true permeability at lower porosities is lower than what is given by the permeability-porosity relationship, then the estimated pore pressure values will be underestimated. For turbidites, permeabilities were assigned based on the permeability-porosity relationship ($\log(k) = -20.0 + 5.25n$) used by Screamton and Ge (1997) and Saffer and Bekins (1998). Permeabilities in the décollement were assigned using the hemipelagic permeability-porosity relationship, unless otherwise noted.

The top boundary of the model was specified to be at hydrostatic pressure ($\lambda^* = 0$) while the landward and bottom boundaries were set at no-flow. The landward boundary was treated as no flow to prevent loss of fluids across the boundary. The bottom boundary was treated also as a no-flow boundary, based on the assumption that the permeability of the oceanic crust is low compared to the sediments above. This assumes that most fractures are filled in the 82 m.y old crust (Bekins et al., 1995). The seaward

boundary was set at hydrostatic constant pressure to accommodate fluid flow through décollement during periods of hydrofracture. The model builds up from the ocean crust above. The ocean crust was assigned a permeability value of 10^{-23} m^2 , a porosity of 0.1 and a matrix compressibility of $1.0 \times 10^{-11} \text{ Pa}^{-1}$.

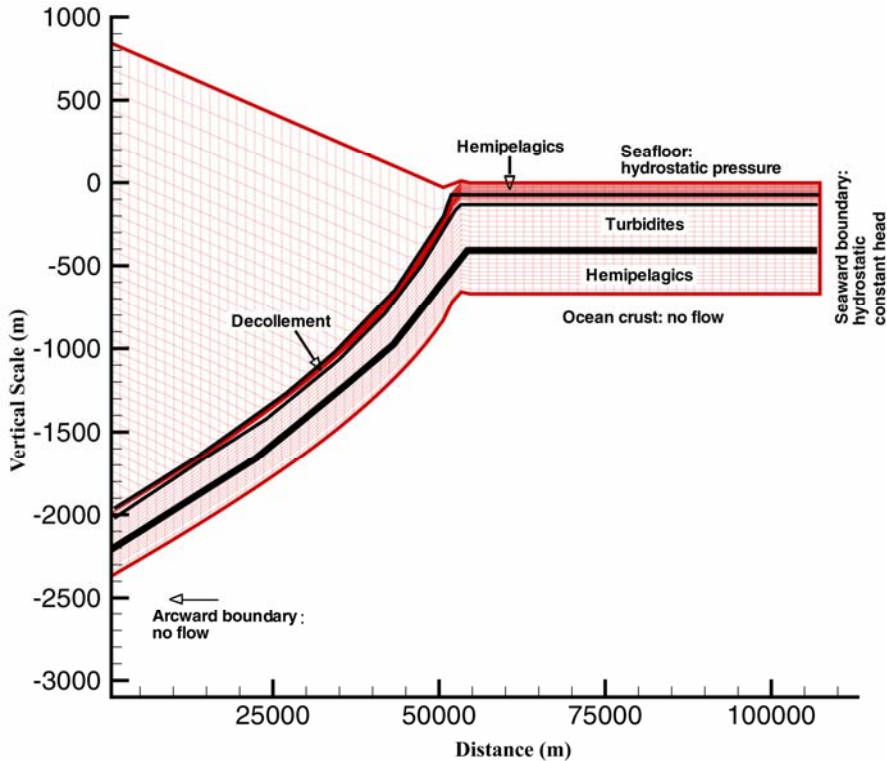


Figure 4-2. Grid and boundary conditions for the prism growth/flow model.

To incorporate the effects of in situ temperature on viscosity, I applied temperature and heat flow boundary conditions, and used SUTRA to calculate temperature distribution. The seafloor boundary was set at of 2° C (Bekins et al., 1994) while the heat flow at the base of the model was assigned as 55 mW m^{-2} (Ferguson et al., 1993) to produce temperatures consistent with those given in Davis and Hussong (1984) and Bekins et al. (1994). The arcward and seaward boundaries were set as no heat flow boundaries. Thermal conductivities and specific heat values for both fluid and solid matrix are given in Table 4-1.

Table 4-1. Fluid and solid matrix properties used for numerical simulations.

Parameter	Value
Fluid compressibility [Pa ⁻¹]	4.40E ⁻¹⁰
Fluid density [kg m ⁻³]	1035
Fluid specific heat [J kg ⁻¹ °C ⁻¹]	4180
Fluid thermal conductivity [J s ⁻¹ m ⁻¹ °C ⁻¹]	0.7
Solid grain density [kg m ⁻³]	2650
Solid grain specific heat [J kg ⁻¹ °C ⁻¹]	1000
Solid grain thermal conductivity [J s ⁻¹ m ⁻¹ °C ⁻¹]	3.0

Sedimentation and Loading Rates

Sedimentation seaward of the deformation front and loading due to the over-riding prism were applied separately in two different phases (Table 4-2). Sedimentation rates for phase one were calculated based on the biostratigraphy of Site 672. During phase one, the incoming sediment column was built using 25 time steps of 2,680,000 years. The average initial sedimentation rate for each unit was based on the initial thickness of that unit and its corresponding deposition time as provided in the biostratigraphy of Site 672. The initial thickness of each unit (i.e., the thickness of the sediment layer prior to consolidation) was calculated based on an initial porosity of 0.70 and 0.60 for hemipelagics and turbidites respectively. Final porosity was estimated based on bulk density data from Leg 171A, Site 1044 (Shipboard Scientific Party, 1998). Porosity was estimated using a solid grain density of 2.65 g/cm³ and a fluid density of 1.035 g/cm³ as used in Screamton and Ge (2000). According to Screamton and Ge (2000) the largest error associated in this conversion is due to the presence of smectite interlayer water, which will overestimate porosity values. During phase two, prism-thickening rates were calculated using prism thickness at Site 671 and a convergence rate of 2 cm/yr. Because the prism was built in segments, the number of loading steps used in phase two varied from 10 to 40 with a constant loading step size of 67,500 years.

Table 4-2. Summary of sedimentation and prism thickening rates calculated from biostratigraphy at Site 672.

Site	Unit	Thickness (m)	Time (Ma)	Vertical loading	
				Initial sedimentation rate (m/yr)	Prism thickening rate (m/yr)
672	Accreted sediments		Present-5	2.60×10^{-3}	3.90×10^{-5}
	Hemipelagics	173	5-18	1.50×10^{-6}	
	Décollement	15	18-25	1.70×10^{-6}	
	Turbidites	285	25-43	1.45×10^{-5}	
	Hemipelagics	187	43-50	1.70×10^{-5}	

According to Bekins et al. (1995), in deeper parts of the accretionary complex, fluid released from clay dehydration becomes important and had been used to explain the observed low-chloride anomalies at the toe of the prism. Moreover, if the rate of fluid released during the dehydration reaction is high enough this mechanism could also contribute to the generation of excess pore pressures. However, studies have not shown that fluids released during smectite dehydration are large enough to affect pore pressures. A fluid flow and budget study by Saffer and Bekins (1998) concluded that dehydration fluid sources are 10-1000 times smaller than fluid released from compaction sources and thus, calculated pore pressures are largely independent of the clay content. Because the model used here only extends to 50 km from the deformation front while based on previous studies (e.g., Bekins et al., 1994) the smectite dehydration is important at distances >50 km from the deformation front, thus fluid sources from dehydration were not included in this study.

Studies based on fluid budget modeling show that prism fluids do not contribute significantly to the décollement flow (Bekins and Screamton, 2006), thus prism fluid reaching the underthrust should be even be smaller. However, elevated pore pressures within the prism due to sources could inhibit upward migration of fluid from the

décollement and underthrust sediment. Because prism sources were not included in this model, low permeabilities were assigned to the prism to compensate. This approach was tested as part of the modeling.

Results and Discussion

In all of the model runs, the absence of prism sources was compensated for by assigning a very low permeability ($1 \times 10^{-26} \text{ m}^2$) to the prism sediments. This assumption creates a barrier between the bottom of the prism and the top of the décollement zone, which inhibits fluid flow in and out of the underthrust and thus predicting the maximum possible λ^* value within the décollement and underthrust sediments. To examine the validity of this approach, I performed a simulation with the same parameters as used by Bekins et al. (1995), except instead of including sources in the prism as they did, a permeability of $1 \times 10^{-26} \text{ m}^2$ was assigned to the prism sediments (Table 4-3). The estimated λ^* values from this simulation at 2.7 million years were in good agreement with those simulated in the underthrust sediments by Bekins et al. (1995). Furthermore, the simulated λ^* values at Site 949C and 948D were consistent to those values obtained from long term monitoring, as were the results from Bekins et al. (1995). Modeled λ^* values along the décollement were 0.31 at Site 949C and 0.48 at Site 948D while λ^* values obtained from long term monitoring were 0.36 at Site 949C and 0.50 at Site 948D. This suggests that assigning a low permeability to the prism is a reasonable compensation for omitting prism sources. The temperature distribution of the accretionary complex in this simulation is also in good agreement with that used by Bekins et al. (1994).

For the base run simulation, there were several significant differences from the parameters used in Bekins et al. (1995). The base run simulation contained both

hemipelagic and turbidite units whereas in Bekins et al. (1995), all sediment units were treated as hemipelagics. In the base run, for hemipelagics, the same permeability-porosity relationship ($\log(k) = -22.0 + 8.45n$) as in Bekins et al. (1995) was used. For turbidites a relationship with higher permeability was used ($\log(k) = -20.0 + 5.25n$). In addition, the décollement was assigned the same permeability-porosity relationship as for the hemipelagic sediments instead of using a higher permeability value as in Bekins et al. (1995) simulation. The results of the base run indicate that maximum λ^* extends from about 4 km arcward from the deformation front and laterally extends arcward with time (Figure 4-3). At all four time periods, the maximum λ^* value is contained in the area directly below the prism. During the first 0.6 million years, the maximum λ^* reached a value of 0.89 in the underthrust sediments and 0.9 in the décollement. Both values increased by 0.03 between 0.6 and 1.3 million years. After reaching a maximum λ^* values of 0.93 in the underthrust and 0.94 in the décollement at the end of 2 million years the maximum λ^* values decreased to 0.90 at 2.7 million years. This decrease in λ^* value with time may have result from the dissipation of pore pressures during the 2.7 million years of subduction. It may be possible that some fluid will flow arcward within the turbidite layer (although it cannot flow out of the arcward boundary) thus, decreasing the peak pore pressures in the décollement and underthrust with time. Calculations by Hanshaw and Bredehoeft (1968) shows that even if a high pore pressure region is surrounded by a low-permeability (10^{-21} m^2) material the pore pressures cannot be maintained above 75 percent of the lithostatic stress for more than 10,000 years. Based on these calculations, the excess pressures bleed off with time because the specific storage, which is a function of the pore volume and the compressibility of water and rock

is so low that only a very small amount of water needs to escape to drastically to lower the pore pressure (Byerlee, 1990). However, it is difficult to confirm flow in the arcward direction based on the results of this study.

The results of the base run has λ^* values lower than the results of Bekins et al. (1995) by 0.1 at the deformation front, while having λ^* values 0.2-0.3 higher 50 km arcward from the deformation front. These differences are caused by the different parameters (permeability-porosity relationships in the décollement and turbidite unit) used in the two simulations.

The λ^* values of the base run provides the upper limit values of λ^* within the décollement and the underthrust sediments because the sediments in the décollement and underthrust would not lose fluid to the prism sediments above. Based on the estimated λ^* values from the base run, the λ^* values does not reach lithostatic during 2.7 million years of prism growth, and thus does not meet the criteria for horizontal hydrofracture in the décollement ($\lambda^* = 1$). However, it should be noted that it may be possible that at greater depths, addition of pressure due to smectite dehydration might be important, and may even increase pore pressures above lithostatic.

Based on the results of the base run it was not possible to reach lithostatic pore pressures resulting in horizontal hydrofracture in the décollement. However, according to the criteria given by Behrmann (1991), the λ^* values needed for vertical hydrofracture is less than 1. Furthermore, vertical focusing of flow has been observed by 3-D seismic images, which shows normal faults extending upward within the turbidite unit (Zhao and Moore, 1998). If vertical hydrofracture could increase pore pressures in the décollement then it is possible for the pressures in the décollement to reach lithostatic. To simulate

this scenario, I used the same parameters as used in the base run, and introduced vertical hydrofractures to the model within the underthrust unit. The model assigned a higher vertical permeability value ($1 \times 10^{-13} \text{ m}^2$) relative to the background bulk permeability, to those elements that have met the vertical hydrofracture criteria of $\lambda^* < 0.8$. Horizontal permeabilities were kept at the background bulk permeability. The hydrofractures were vertically extended to the base of the décollement by assigning higher vertical permeability values to all elements above any element that meets the criteria. This allows fluids to flow towards the décollement through the vertical hydrofractures. The λ^* values at the décollement were examined to see whether it has reached values greater than lithostatic, allowing horizontal hydrofracturing.

The estimated λ^* values in the décollement and in the underthrust sediments were very similar to those predicted from the base run. Results indicate that adding vertical hydrofractures in the underthrust does not increase pore pressures in the décollement to lithostatic, causing horizontal hydrofracture. One possible explanation would be that the amount of fluids entering the vertical hydrofracture is not sufficient to increase pore pressures to lithostatic. The criterion for vertical hydrofracture was met within the turbidite unit, which has been previously suggested as a possible pathway for lateral flow (e.g., Henry, 2000). It may also be possible that pore pressures reach lithostatic pressures and dissipate at smaller time frames than the loading step size used in this study (< 67,500 yrs).

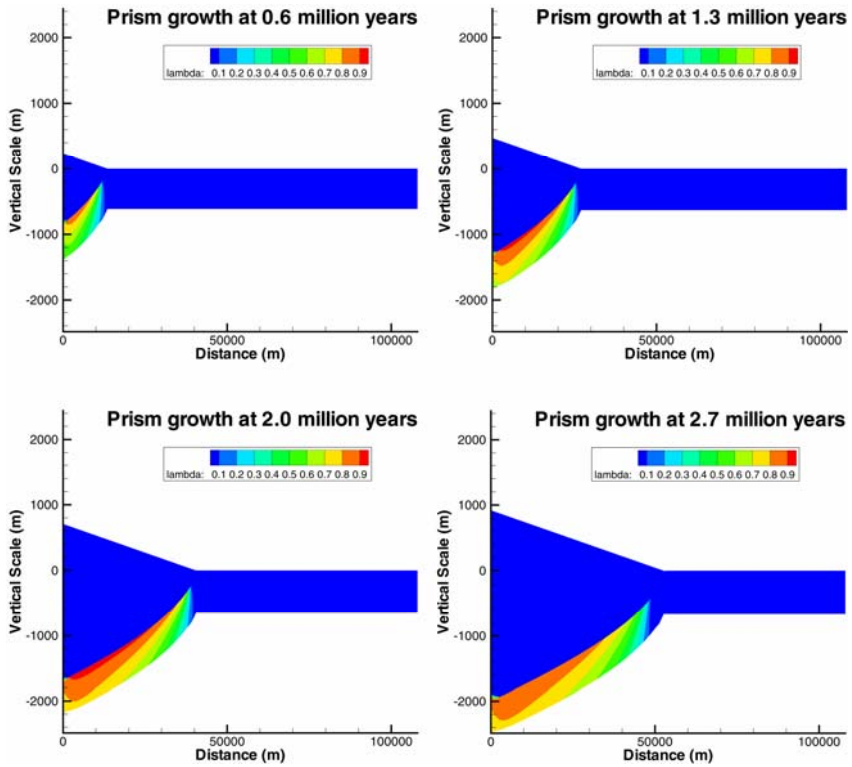


Figure 4-3. Simulated λ^* values for base run at 0.6, 1.3, 2.0, and 2.7 million years.

Because vertical hydrofractures in the underthrust sediments did not increase pore pressures in the décollement to lithostatic, an alternative to hydrofracture was tested in which the décollement was assigned permeabilities based on a bulk permeability-effective stress relationship. The bulk permeability and vertical effective stress relationship was obtained from in-situ bulk permeability measurements that were made at varying effective stress values in a borehole that intersected the décollement zone (Fisher and Zwart, 1996). This scenario tests the possibility of episodic fluid flow in the décollement while maintaining pore pressures that are close to lithostatic pressures at the base of the décollement. The relationship is given by: $\log k_{\text{bulk}} = -12.3 - 1.6\sigma_v$ where σ_v is the vertical effective stress in MPa [$\text{ML}^{-1}\text{T}^{-2}$] (Fisher and Zwart, 1996). Based on this relationship, the upper extreme bulk permeability approaches 10^{-12} m^2 when fluid pressure reaches lithostatic while the lower extreme of 10^{-18} m^2 was predicted at

hydrostatic pressures (Fisher and Zwart, 1996). All other sediment units were assigned permeabilities based on the permeability-porosity relationships for hemipelagics and turbidites. The estimated maximum λ^* value of 0.87 was reached at 2 million years (Figure 4–4). During the first 0.6 million years the maximum λ^* value was 0.69 and λ^* gradually increased to 0.82 at 1.3 million years and to 0.87 at 2 million years. At 2.7 million years the maximum λ^* value decreased to 0.85 from 0.87. The décollement permeability at 4 km arcward of the deformation front (Site 948) is about $1 \times 10^{-15} \text{ m}^2$.

Due to the bulk-permeability-vertical effective stress relationship, the bulk permeability increases with an effective stress decrease. Thus, estimated λ^* at shallow depths closer to the deformation front were lower than those estimated at the arcward end. Because permeability in the décollement is higher at shallow depths, the overpressured fluids will escape through the high permeability décollement at the toe of the prism, reducing pore pressures. At Site 949C the estimated λ^* is 0.28 while the λ^* at Site 948D is 0.48. Compared to the values obtained from the long term monitoring, at Site 948D the λ^* values fairly matched while at Site 949C the λ^* value was underestimated by 0.08. The lower λ^* value at Site 949C can be explained by the higher permeabilities in the décollement (at low effective stress) relative to the décollement permeabilities at Site 948D which is located 4 km arcward of the deformation front. In comparison to the results of the base run, the λ^* values estimated here were only slightly lower. This suggests that assigning a bulk permeability-vertical effective stress relationship into the décollement not only allows fluid to expel at the toe of the complex where effective stress is relatively low and permeability is high, but also maintains

relatively high pore pressures along the base of the prism thus, maintaining its narrow taper.

To investigate the combined effect of both vertical hydrofracture and the décollement with the bulk permeability-effective stress relationship the two parameters were combined. The maximum λ^* (0.87) estimated from the combined simulation is similar to the maximum λ^* estimated from bulk permeability-effective stress relationship in the décollement and in the underthrust (Table 4-3).

Table 4-3. Summary of simulation runs with the estimated values of maximum λ^* (λ_{max}^*) in the underthrust and the décollement. The location of the λ_{max}^* is given seaward from the arcward end of the model during 2.7 million years of prism growth.

Run	Unit	$\log(k_0)$	φ	Vertical Hydro-fracture (m^2)	k_d (m^2)	Underthrust		Décollement	
						λ^*_{max}	location	λ^*_{max}	location
Base Run	Turbidites Hemipelagics	-20 -22	5.25 8.44	NA	NA	0.93	15.0	0.94	10.8
Bekins et al. (1995)	Turbidites Hemipelagics	-22 -22	8.44 8.44	NA	10^{-15}	0.64	39.0	0.64	0.40
Vertical hydrofracture	Turbidites Hemipelagics	-20 -22	5.25 8.44	10^{-13}	NA	0.93	15.0	0.94	10.8
Varying k_d	Turbidites Hemipelagics	-20 -22	5.25 8.44	10^{-13}	$k_{\text{bulk}} - \sigma_v$	0.87	10.0	0.87	12.0
Vertical hydrofracture + varying k_d	Turbidites Hemipelagics	-20 -22	5.25 8.44	10^{-13}	$k_{\text{bulk}} - \sigma_v$	0.87	10.0	0.87	10.8

However, the combined simulation indicate a slight variation in the λ^* profile closer to the deformation front relative to those estimated using only the bulk permeability-effective stress relationship in the décollement (Figure 4-4). The combined simulation predicts slightly higher values (by 0.02) of $\lambda^* \sim 28$ km seaward from the arcward end (Figure 4-4). This slightly high λ^* may represent the minor effect of vertical hydrofracture. The observed sudden increase in the λ^* profiles closer to the deformation of both in the bulk permeability-effective stress simulation and the combined simulation may suggest a possible transient response. However, these transient events probably

occur at smaller time periods than the time step used in this study and thus, examining the pore pressures at smaller time steps may provide insight to possible episodic flow events in the décollement.

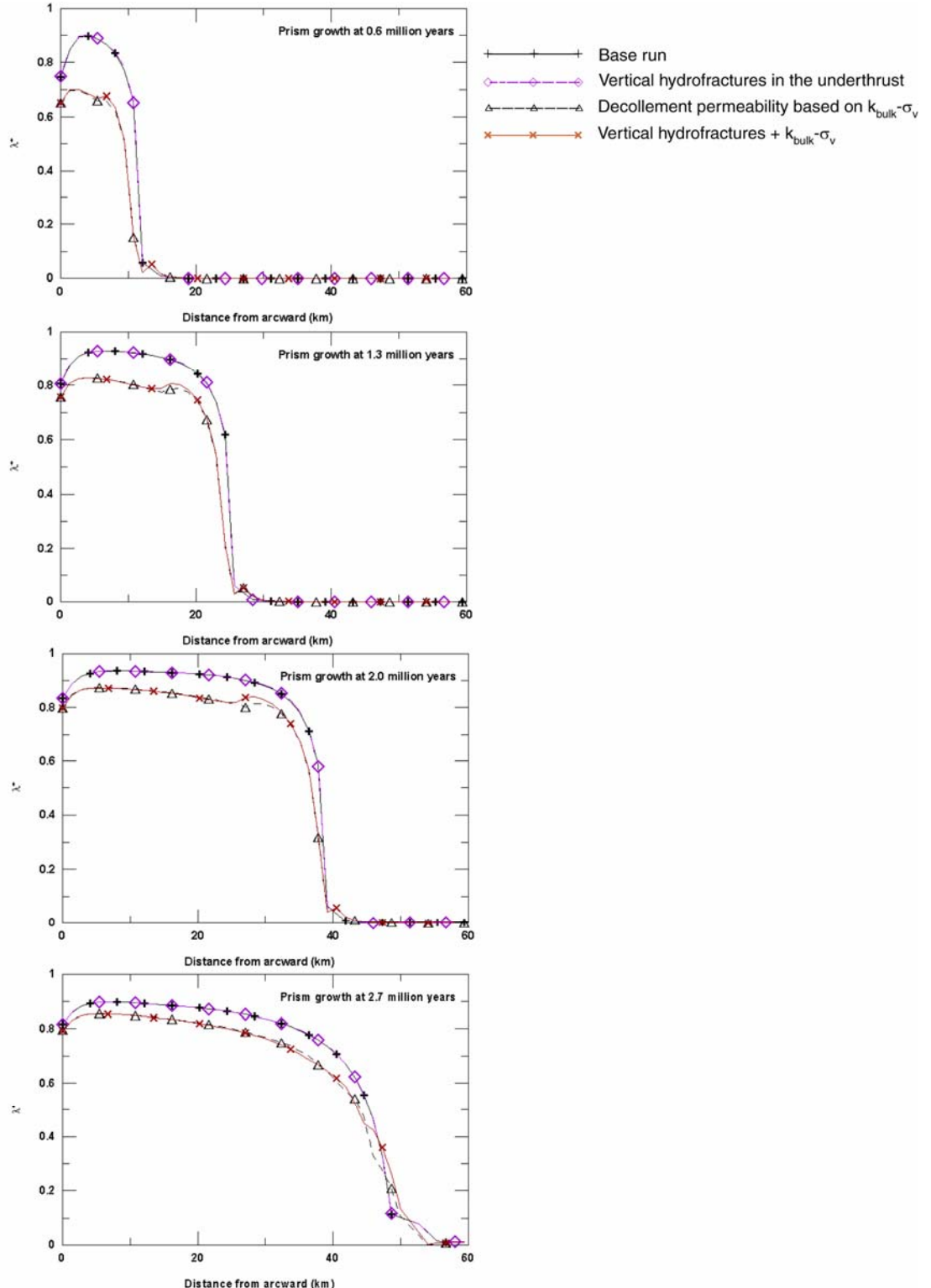


Figure 4-4. Estimated λ^* values in the décollement at 0.6, 1.3, 2.0 and 2.7 million years of prism growth for all simulations.

Conclusions

The prism growth and flow model used in this study allows examination of pore pressure development as sediments subduct beneath the accretionary prism. Simulations with the décollement given the same permeability as surrounding sediments predicted a maximum possible λ^* value of 0.94 in the décollement. Although the predicted λ^* value was close to lithostatic pressures it was unable to reach lithostatic as speculated by previous studies, and thus would not produce horizontal hydrofracture in the décollement zone. To test the effects of vertical hydrofractures on episodic fluid flow, vertical hydrofractures were introduced in the underthrust sediments based on a criteria presented by Behrmann (1991). The results indicate that vertical hydrofractures were unable to increase pore pressures in the décollement, either due to lack of fluids entering the fracture increasing pore pressures or because pore pressures reached lithostatic pressures and were dissipated within a smaller time frame compared to the loading step used in this study.

Another mechanism for episodic fluid flow was tested by assigning a bulk permeability-vertical stress relationship to the décollement. The results of this simulation indicate that excess pore pressures close to lithostatic can be sustained at the base of the prism while fluid is expelled at the toe of the complex. The results suggest that the décollement may not need to hydrofracture to generate transient lateral fluid flow. With the bulk permeability-vertical effective stress relationship the décollement could potentially propagate fluid pulses towards the toe of the complex releasing fluids at the toe. The effects of vertical hydrofracture and assigning the bulk permeability-effective

stress relationship in the décollement should be further investigated at smaller time steps to examine if possible episodic events occur in the décollement.

CHAPTER 5 SUMMARY AND CONCLUSIONS

In fluid flow modeling studies, sediment permeability is the most important factor that controls modeled pore pressures. In such studies, permeability is approximated based on a systematic relationship of permeability and porosity. Marine sediments from Northern Barbados, Costa Rica, Nankai and Peru subduction zones were used in this study to examine permeability-porosity relationships based on depositional environment, grain size distribution and structural domain. Results suggest moderate to high correlation between permeability and porosity for argillaceous sediments and little correlation for carbonate dominant sediments. For argillaceous sediments, the classification based on location and grain size distribution provides greater correlation between permeability and porosity than the depositional environment of the sediment alone. The effects of structural domain on permeability-porosity relationship could not be evaluated due to limited data.

Elevated fluid pore pressures play a critical role in the development of accretionary complexes, including the development of the décollement zone. A one-dimensional loading and fluid flow model was used to simulate excess pore pressures and porosities. Simulated excess pore pressure ratios (as a fraction of lithostatic pressure – hydrostatic pressure) using the best-fit permeability-porosity relationship were lower than predicted from previous studies. The model was also used to test the sensitivity of excess pore pressure ratios in the underthrust sediments to bulk permeability, lateral stress in the prism, and a hypothetical low-permeability barrier at the décollement. Results

demonstrated significant increase in pore pressures below the décollement with lower bulk permeability, such as obtained by using the lower boundary of permeability-porosity data, or when a low-permeability barrier is added at the décollement. In contrast, pore pressures in the underthrust sediments demonstrated less sensitivity to added lateral stresses in the prism, although the profile of the excess pore pressure ratio is affected. Both simulations with lateral stress and a low-permeability barrier at the décollement resulted in sharp increases in porosity at the décollement, similar to that observed in measured porosities. Furthermore, in both scenarios, maximum excess pore pressure ratios were found at the décollement suggesting that either of these factors would contribute to stable sliding along the décollement.

Changes in fluid flow pressures and its distribution regulate the mode of deformation affecting the evolution of the accretionary complex. To fully understand the development of pore pressures and thus, hypothesized episodic fluid flow, one should examine the pore pressure development through both space and time. A two-dimensional prism growth and flow model was used to examine the pore pressure development through the evolution of the accretionary complex and mechanics of episodic fluid flow. Results indicate λ^* values (0.94) close to lithostatic pressures. However, estimated λ^* values were unable to reach lithostatic pressures thus not allowing horizontal hydrofracture in the décollement zone. Vertical hydrofractures were introduced in the underthrust sediments to examine whether they would increase pore pressures in the décollement. The results indicate that vertical hydrofractures were unable to increase pore pressures in the décollement zone, either due to lack of fluids entering the fracture increasing pore pressures or pore pressures reached lithostatic pressures and were

dissipated within a smaller time frame compare to the time step used in this study. To examine another possible mechanism for episodic fluid flow, a bulk permeability-vertical stress relationship was assigned to the décollement. Results indicate that excess pore pressures close to lithostatic can be sustained at the base of the prism while fluid is expelled at the toe of the complex. This further suggest that décollement may not need to hydrofracture initiating transient lateral fluid flow because the bulk permeability-vertical effective stress relationship could propagate fluid pulses towards the toe of the complex releasing fluids at the toe of the prism. However, the effects of vertical hydrofracture and assigning the bulk permeability-effective stress relationship in the décollement should be further investigated at smaller time steps to examine if episodic events occur in the décollement.

APPENDIX
**LISTING OF PERMEABILITY, POROSITY, GRAIN SIZE DATA WITH
REFERENCES USED IN THIS STUDY**

Table A-1. Listing of permeability, porosity, grain size data with references used in this study. † Grain size and carbonate data were assigned based on the grain size data available for similar samples from Screamont et al. (2005) for Costa Rica

Location	Permeability Reference	Depth (mbsf)	Permeability		Porosity	Structural domain	Lithology	Grain Size (wt %)			Carbonate (wt%)	Grain Size and Carbonate (wt%) Reference
			log k	(m ²)				Sand (>63 µm)	Silt (63-4 µm)	Clay (<4 µm)		
Barbados												
156-948C-13X-3*	Vrolijk et al. in Zwart et al. (1997)	530.4	-18.3098	4.9000E-19	0.55	Underthrust	Gray claystone	0	8	92		Meyer and Fisher (1997)
156-949C-2X-1*	Maltman et al. in Zwart et al. (1997)	254.08	-17.3279	4.7000E-18	0.62	Prism	Gray claystone	0	9	91		Meyer and Fisher (1997)
			-17.3468	4.5000E-18	0.61							
			-17.7799	1.6600E-18	0.59							
			-17.7852	1.6400E-18	0.59							
			-17.8386	1.4500E-18	0.59							
			-17.8861	1.3000E-18	0.58							
			-17.8665	1.3600E-18	0.57							
			-18.0000	1.0000E-18	0.57							
			-18.5229	3.0000E-19	0.56							
156-949C-15X-5*	Bruckmann et al. (1997)	366.23	-15.0937	8.0600E-16	0.70	Prism	Light olive-gray claystone	0	9	91		Meyer and Fisher (1997)
			-16.3788	4.1800E-17	0.69							
			-17.4855	3.2700E-18	0.69							
156-949C-19X-1*		399.2	-16.9508	1.1200E-17	0.62	Decollement	Yellowish brown claystone	3	12	85		Meyer and Fisher (1997)
			-17.4855	3.2700E-18	0.62							
			-17.7878	1.6300E-18	0.61							
156-949C-22X-1*		428.75	-17.1046	7.8600E-18	0.55	Decollement	Light brownish gray claystone	1	7	92		Meyer and Fisher (1997)
			-17.4353	3.6700E-18	0.55							

Table A-1. Continued

Location	Permeability Reference	Depth (mbsf)	Permeability		Porosity	Structural domain	Lithology	Grain Size (wt %)			Carbonate (wt%)	Grain Size and Carbonate (wt%) Reference
			-17.9508	1.1200E-18	0.54							
110-671B-9H-2*	Taylor and Leonard (1990)	76.8	-16.0836	8.2492E-17	0.57	Prism	Marl	7	18	76	29.7	Taylor and Leonard (1990)
110-672A-2H-3		7.7	-14.5933	2.5508E-15	0.67	Reference site (incoming sediments)	Calcareous Mud	20	35	44	35	Taylor and Leonard (1990)
110-672A-19X-3*		165.8	-15.6186	2.4064E-16	0.67	Reference site (incoming sediments)	Calcareous Mud	0	33	67	0	Taylor and Leonard (1990)
110-672A-19X-3*		165.9	-16.2622	5.4674E-17	0.67	Reference site (incoming sediments)	Calcareous Mud	0	33	67	0	Taylor and Leonard (1990)
110-676A-9H-3*		77.2	-15.7134	1.9348E-16	0.56	Prism	Calcareous Mud	13	44	43	38.01	Taylor and Leonard (1990)
110-676A-12X-3*		105.6	-15.8234	1.5016E-16	0.49	Prism	Calcareous Mud	2	23	75	22.23	Taylor and Leonard (1990)
Nankai												
190-1173A-22H-2*	Gamage and Screateon (2003)	199.9	-16.2857	5.1793E-17	0.57	Reference site (incoming sediments)	Silty clay	1	48	51		Steurer and Underwood (2003)
			-16.3924	4.0516E-17	0.56							
			-16.4064	3.9227E-17	0.55							
190-1173A-31X-1*		284.59	-16.7012	1.9896E-17	0.62	Reference site (incoming sediments)	Silty claystone to clayey siltstone	2	39	59		Steurer and Underwood (2003)
			-16.8898	1.2888E-17	0.60							

Table A-1. Continued

Location	Permeability Reference	Depth (mbsf)	Permeability		Porosity	Structural domain	Lithology	Grain Size (wt %)			Carbonate (wt%)	Grain Size and Carbonate (wt%) Reference
190-1173A-39X-5*		367.07	-17.6054	2.4809E-18	0.41	Reference site (incoming sediments)	Silty claystone, moderate bioturbation	1	55	44		Steurer and Underwood (2003)
			-17.6594	2.1909E-18	0.36							
			-17.8175	1.5224E-18	0.33							
190-1173A-41X-CC*		388.75	-17.6026	2.4970E-18	0.45	Reference site (incoming sediments)	Silty claystone, mottled due to moderate bioturbation	1	51	48		Steurer and Underwood (2003)
			-17.7780	1.6674E-18	0.43							
			-17.9266	1.1841E-18	0.43							
190-1173A-46X-1*		428.59	-17.7192	1.9090E-18	0.45	Reference site (incoming sediments)	Silty claystone	0	31	69		Steurer and Underwood (2003)
			-17.8152	1.5304E-18	0.43							
			-17.9036	1.2485E-18	0.41							
190-1174B-42R-3*		538.23	-17.1027	7.8938E-18	0.37	Prism	Silty claystone, altered ash	1	44	56		Steurer and Underwood (2003)
			-17.6960	2.0137E-18	0.34							
			-17.8152	1.5304E-18	0.32							
190-1174B-59R-5*		704.95	-18.2824	5.2196E-19	0.32	Prism	Silty claystone	1	32	68		Steurer and Underwood (2003)
			-18.4495	3.5522E-19	0.30							

Table A-1. Continued

Table A-1. Continued

Location	Permeability Reference	Depth (mbsf)	Permeability		Porosity	Structural domain	Lithology	Grain Size (wt %)			Carbonate (wt%)	Grain Size and Carbonate (wt%) Reference
170-1039B-10H-2	Saffer et al. (2000)	80.85	-16.4000	3.9811E-17	0.62	Reference site (incoming sediments)	Upper hemipelagic sec: diatom ooze with ash					
			-16.4000	3.9811E-17	0.68							
			-16.0000	1.0000E-16	0.75							
			-15.9000	1.2589E-16	0.75							
170-1039B-16X-8		141.54	-17.6000	2.5119E-18	0.67	Reference site (incoming sediments)	Upper hemipelagic section: calcareous clay					
			-17.1000	7.9433E-18	0.68							
			-16.4000	3.9811E-17	0.76							
			-15.5000	3.1623E-16	0.79							
			-14.8000	1.5849E-15	0.80							
170-1039B-26X-6		237.25	-15.5000	3.1623E-16	0.53	Reference site (incoming sediments)	Pelagic section: siliceous nannofossil ooze					

Table A-1. Continued

Location	Permeability Reference	Depth (mbsf)	Permeability		Porosity	Structural domain	Lithology	Grain Size (wt %)			Carbonate (wt%)	Grain Size and Carbonate (wt%) Reference
170-1040C-30R-4			-15.1000	7.9433E-16	0.79	Underthrust	Upper hemipelagic section: silty clay stone with ash layers					
			-15.8000	1.5849E-16	0.78							
			-16.8000	1.5849E-17	0.69							
			-16.9000	1.2589E-17	0.72							
205-1253-2R-4*	McKiernan and Saffer (2005)	380.07	-15.9889	1.0260E-16	0.46	Reference site (incoming sediments)	Calcareous mudstones	†1	49	50	57.41	Screaton et al. (2005)
205-1253-3R-2*		386.83	-16.2952	5.0680E-17	0.50	Reference site (incoming sediments)	Calcareous mudstones	†2	43	55	47.41	Screaton et al. (2005)
205-1253-4R-1*		394.91	-16.9024	1.2520E-17	0.47	Reference site (incoming sediments)	Calcareous mudstones	†8	50	42		Screaton et al. (2005)
205-1254-16R-4		366.74	-18.5810	2.6240E-19	0.39	Decollement	Hemipelagic mudstones	†6	39	55	1.43	Screaton et al. (2005)
205-1255-2R-CC*		134.89	-19.0337	9.2540E-20	0.32	Underthrust	Hemipelagic mudstones	†3	46	51	4.67	Screaton et al. (2005)
			-15.3177	4.8120E-16	0.50							
			-17.1045	7.8620E-18	0.47							
			-17.8170	1.5240E-18	0.44							
			-18.3405	4.5660E-19	0.39							
			-18.8283	1.4850E-19	0.32							

Table A-1. Continued

Table A-1. Continued

Location	Permeability Reference	Depth (mbsf)	Permeability		Porosity	Structural domain	Lithology	Grain Size (wt %)			Carbonate (wt%)	Grain Size and Carbonate (wt%) Reference
205-1253A-03R-1*		386	-15.0177	9.6000E-16	0.71	Reference site (incoming sediments)	Pelagic section: nannofossil chalk with diatom	2	43	55	47.41	Screaton et al. (2005)
			-15.2652	5.4300E-16	0.69							
			-15.3872	4.1000E-16	0.67							
205-1255A-02R-CC*		135	-17.5129	3.0700E-18	0.57	Underthrust	Lower hemipelagic section	3	46	51	4.67	Screaton et al. (2005)
			-17.6216	2.3900E-18	0.56							
			-17.7721	1.6900E-18	0.53							
205-1255A-03R-CC*		147	-17.7570	1.7500E-18	0.49	Underthrust	Lower hemipelagic section	1	34	65	1.59	Screaton et al. (2005)
			-17.7595	1.7400E-18	0.47							
			-17.7852	1.6400E-18	0.46							
205-1255A-04R-CC*		152	-17.4425	3.6100E-18	0.66	Underthrust	Lower hemipelagic section	1	34	65	1.77	Screaton et al. (2005)
			-17.5229	3.0000E-18	0.64							
			-17.6421	2.2800E-18	0.59							
Peru												
201-1231B-3H*	Gamage et al. (2005)	17.1	-16.5031	3.1400E-17	0.89	Peru Basin	Diatom rich clay and Diatom ooze	22	67	11		Aiello (unpubl. data)
			-16.9914	1.0200E-17	0.87							
			-17.1694	6.7700E-18	0.86							

Table A-1. Continued

Location	Permeability Reference	Depth (mbsf)	Permeability		Porosity	Structural domain	Lithology	Grain Size (wt %)			Carbonate (wt%)	Grain Size and Carbonate (wt%) Reference
			-17.4634	3.4400E-18	0.85							
201-1231B-6H*		44.1	-15.8268	1.4900E-16	0.85	Peru Basin	Silt with some volcanic glass	11	46	43		Aiello (unpubl. data)
			-16.2708	5.3600E-17	0.83							
			-16.6038	2.4900E-17	0.82							
			-16.8210	1.5100E-17	0.80							
201-1231B-9H		75.7	-15.1107	7.7500E-16	0.59	Peru Basin	Nannofossil ooze	54	46	0		Aiello (unpubl. data)
			-15.2472	5.6600E-16	0.58							
			-15.3420	4.5500E-16	0.57							
			-15.3706	4.2600E-16	0.56							
201-1231B-13H		112.1	-15.3344	4.6300E-16	0.66	Peru Basin	Nannofossil ooze	38	62	0		Aiello (unpubl. data)
			-15.3883	4.0900E-16	0.65							
			-15.4225	3.7800E-16	0.64							
			-15.4365	3.6600E-16	0.63							
201-1230A-4H		31	-16.7328	1.8500E-17	0.68	Lower slope of Peru trench	Diatom ooze with some clay and silt					
			-16.7696	1.7000E-17	0.67							
			-16.8861	1.3000E-17	0.66							
			-16.9393	1.1500E-17	0.64							
201-1230A-9H		70.7	-16.2403	5.7500E-17	0.68	Lower slope of Peru trench	Diatom ooze with some clay and silt					

Table A-1. Continued

Location	Permeability Reference	Depth (mbsf)	Permeability		Porosity	Structural domain	Lithology	Grain Size (wt %)			Carbonate (wt%)	Grain Size and Carbonate (wt%) Reference
			-16.3726	4.2400E-17	0.68							
			-16.4698	3.3900E-17	0.67							
			-16.5100	3.0900E-17	0.67							
201-1230A-31X*		230.8	-16.4789	3.3200E-17	0.53	Lower slope of Peru trench	Diatom ooze with some clay and silt	13.74	59.41	17.86		Aiello (unpubl. data)
			-16.7122	1.9400E-17	0.49							
			-16.7878	1.6300E-17	0.48							
			-16.8327	1.4700E-17	0.45							
201-1230A-35X*		252.1	-16.6946	2.0200E-17	0.58	Lower slope of Peru trench	Diatom ooze with some clay and silt	0.01	80.97	19.02		Aiello (unpubl. data)
			-16.7471	1.7900E-17	0.55							
			-16.8508	1.4100E-17	0.53							
			-16.9031	1.2500E-17	0.51							
201-1227A-3H		19.3	-15.6216	2.3900E-16	0.71	Shallow Peru trench	Silt					
			-15.7471	1.7900E-16	0.69							
			-15.8125	1.5400E-16	0.67							
			-15.9469	1.1300E-16	0.64							
201-1227A-12H		101.9	-15.6091	2.4600E-16	0.70	Shallow Peru trench	Diatom ooze/nannofossil/silt					
			-15.7447	1.8000E-16	0.68							
			-15.7959	1.6000E-16	0.67							
			-15.9788	1.0500E-16	0.66							

Table A-1. Continued

Location	Permeability Reference	Depth (mbsf)	Permeability		Porosity	Structural domain	Lithology	Grain Size (wt %)			Carbonate (wt%)	Grain Size and Carbonate (wt%) Reference
201-1226B-4H		24.8	-15.1694	6.7700E-16	0.76	Equatorial pacific	Nannofossil oozes and diatom oozes	18	64	18		Aiello and Kellett (unpubl. data)
			-15.2708	5.3600E-16	0.74							
			-15.3288	4.6900E-16	0.73							
			-15.3726	4.2400E-16	0.73							
201-1226B-26H		239.6	-15.5171	3.0400E-16	0.67	Equatorial pacific	Nannofossil oozes and diatom oozes	33	57	10		Aiello and Kellett (unpubl. data)
			-15.5143	3.0600E-16	0.67							
			-15.5346	2.9200E-16	0.66							
			-15.5436	2.8600E-16	0.65							
201-1226B-43X		381.2	-16.8041	1.5700E-17	0.62	Equatorial pacific	Nannofossil oozes and diatom oozes	14	67	19		Aiello and Kellett (unpubl. data)
			-16.8539	1.4000E-17	0.58							
			-16.9066	1.2400E-17	0.57							
			-16.9914	1.0200E-17	0.56							
201-1226B-46X		409.4	-17.7328	1.8500E-18	0.58	Equatorial pacific	Nannofossil oozes and diatom oozes	13	71	16		Aiello and Kellett (unpubl. data)
			-17.8508	1.4100E-18	0.56							
			-17.8761	1.3300E-18	0.53							
			-17.9031	1.2500E-18	0.52							

Table A-1. Continued

Location	Permeability Reference	Depth (mbsf)	Permeability		Porosity	Structural domain	Lithology	Grain Size (wt %)			Carbonate (wt%)	Grain Size and Carbonate (wt%) Reference
201-1225A-4H		24.7	-15.4425	3.6100E-16	0.78	Equatorial pacific	Nannofossil ooze and some diatom, radiolarian and foram oozes	26	62	12	Aiello and Kellett (unpubl. data)	
			-15.5498	2.8200E-16	0.75							
			-15.7878	1.6300E-16	0.73							
			-15.7011	1.9900E-16	0.71							
201-1225A-10H		83.2	-15.6180	2.4100E-16	0.68	Equatorial pacific	Nannofossil and some diatom oozes	31	58	11	Aiello and Kellett (unpubl. data)	
			-15.6757	2.1100E-16	0.66							
			-15.7721	1.6900E-16	0.65							
			-15.8447	1.4300E-16	0.64							
201-1225A-26H		242.7	-15.1688	6.7800E-16	0.68	Equatorial pacific	Nannofossil and diatom oozes	21	79	0	Aiello and Kellett (unpubl. data)	
			-15.2211	6.0100E-16	0.66							
			-15.2807	5.2400E-16	0.65							
			-15.3478	4.4900E-16	0.64							
201-1225A-34H		309.7	-15.6253	2.3700E-16	0.64	Equatorial pacific	Nannofossil and diatom oozes	17	73	10	Aiello and Kellett (unpubl. data)	
			-15.6596	2.1900E-16	0.63							
			-15.7212	1.9000E-16	0.62							
			-15.7423	1.8100E-16	0.61							

Table A-1. Continued

Location	Permeability Reference	Depth (mbsf)	Permeability		Porosity	Structural domain	Lithology	Grain Size (wt %)			Grain Size and Carbonate (wt%) Reference
			Sand (>75 µm)	Silt (75-5 µm)				Sand (>75 µm)	Silt (75-5 µm)	Clay (<5 µm)	
112-679C-8H-2	Masters and Christian (1990)	68.9	-16.5394	2.8880E-17	0.69	Peru shelf	Diatomaceous silty soils	9	65	26	Masters and Christian, 1990
			-16.2384	5.7756E-17	0.69						
			-16.3176	4.8128E-17	0.69						
			-15.9791	1.0493E-16	0.74						
			-16.1135	7.7002E-17	0.74						
			-16.1189	7.6050E-17	0.74						
			-15.5394	2.8880E-16	0.79						
			-15.5852	2.5990E-16	0.79						
			-15.2384	5.7756E-16	0.81						
			-15.4725	3.3690E-16	0.81						
			-15.5394	2.8880E-16	0.81						
			-15.6943	2.0216E-16	0.81						
			-15.7378	1.8289E-16	0.81						
			-15.9026	1.2514E-16	0.81						
112-681C-2H-3		10.3	-16.5694	2.6953E-17	0.57	Peru upper slope	Diatomaceous silty soils	35	61	4	Masters and Christian, 1990
			-16.4145	3.8503E-17	0.57						
			-16.3538	4.4279E-17	0.57						
			-16.6364	2.3099E-17	0.59						
			-16.3831	4.1390E-17	0.59						
			-16.3176	4.8128E-17	0.59						
			-16.2457	5.6794E-17	0.64						
			-16.1777	6.6420E-17	0.64						
			-16.1028	7.8922E-17	0.64						

LIST OF REFERENCES

- Adatia, R. H., and A. J. Maltman (2004), Data report: Initial permeability determinations on sediments from the Nankai Trough accretionary prism, ODP Sites 1173 and 1174. In Mikada, H., Moore, G.F., Taira, A., Becker, K., Moore, J.C., and Klaus, A. (Eds.), *Proc. ODP, Sci. Results*, 190/196, 1-12 [Online]. Available from World Wide Web<<http://www-odp.tamu.edu/publications/190196SR/VOLUME/CHAPTERS/214.PDF>>. [Accessed 2004-12-10]
- Anderson, M. P. and W. W. Woessner (1992), Applied groundwater modeling, Simulation of flow and advective transport, Academic Press, San Diego, CA.
- Athy, L. F. (1930), Density, porosity, and compaction of sedimentary rocks, *Am. Assoc. Pet. Geol. Bull.*, 14, 1-23.
- Aubouin, J., and R. von Huene (1985), Summary; Leg 84, Middle America Trench transect off Guatemala and Costa Rica, *Proc. Deep Sea Drill. Project Init. Rep.*, 84, 939-957.
- Bangs, N. L.B., and S. P.S. Gulick (2005), Physical properties along the developing decollement in the Nankai Trough: inferences from 3-D seismic reflection data inversion and Leg 190 and 196 drilling data. In Mikada, H., Moore, G.F., Taira, A., Becker, K., Moore, J.C., and Klaus, A. (Eds.), *Proc. ODP, Sci. Results*, 190/196, 1-18 [Online]. Available from World Wide Web<<http://www-odp.tamu.edu/publications/190196SR/VOLUME/CHAPTERS/354.PDF>>. [Accessed 2005-06-25]
- Bangs, N. L.B., and G. K. Westbrook (1991), Seismic modeling of the decollement zone at the base of the Barbados Ridge accretionary complex, *J. Geophys. Res.*, 96, 3853-3866.
- Bear, J. and A. Verruijt (1987), Modeling Groundwater Flow and Pollution, D. Reidel Publishing Company, Dordrecht, Holland.
- Becker, K., A. T. Fisher, and E. E. Davis (1997), The CORK experiment in Hole 949C: Long-term observations of pressure and temperature in the Barbados accretionary prism, *Proc. Ocean Drill. Program Sci. Results*, 156, 247-252.
- Behrmann, J. H. (1991), Conditions for hydrofracture and the fluid permeability of accretionary wedges, *Earth Planet. Sci. Lett.*, 107, 550-558.

- Behrmann, J. H. (1992), Conditions for hydrofracture and the fluid permeability of accretionary prisms, *Earth Planet. Sci. Lett.*, 107, 550-558.
- Bekins, B. A., and S. J. Dreiss (1992), A simplified analysis of parameters controlling dewatering in accretionary prisms, *Earth Planet. Sci. Lett.*, 109, 275-287.
- Bekins, B. A., A. M. McCaffrey and S. J. Dreiss (1994), The influence of kinetics on the smectite to illite transition in the Barbados accretionary prism, *J. Geophys. Res.*, 99, 18,147-18,158.
- Bekins, B. A., A. M. McCaffrey and S. J. Dreiss (1995), Episodic and constant flow models for the origin of low-chloride waters in a modern accretionary complex, *W. Resour. Res.*, 31, 3205-3215.
- Bekins, B. A. and E. Screamton (in press), Pore pressures and fluid flow in the Northern Barbados Accretionary Complex, In Tim Dixon (Ed.), Proceedings from the Seismogenic Zone Theoretical Institute, Snowbird, Utah, march 2003, Columbia University Press.
- Bernstein-Taylor, B. L., K. S. Kirchoff-Stein, E. A. Silver and D. A. Reed (1992), Large-scale duplexes within the New Britain accretionary wedge: a possible example of accreted ophiolitic slivers, *Tectonics*, 11, 732-752.
- Biju-Duval, B., and team (1984), *Initial Reports Deep Sea Drilling Project*, vol. 78A, U.S. Government Printing Office, Washington.
- Bird, R. B., W. E. Stewart, and E. N. Lightfoot (1960), *Transport Phenomena*, John Wiley and Sons, Inc. Madison, WI.
- Boggs, S., (2001), Principles of sedimentology and stratigraphy, pp. 378-416, New Jersey, Prentice-Hall, Inc.
- Bourlange, S., L. Jouniaux, P. Henry (2004), Data report: Permeability, compressibility, and friction coefficient measurements under confining pressure and strain, Leg 190, Nankai Trough. In Mikada, H., Moore, G.F., Taira, A., Becker, K., Moore, J.C., and Klaus, A. (Eds.), *Proc. ODP, Sci. Results*, 190/196, 1-16 [Online]. Available from World Wide Web<<http://www-odp.tamu.edu/publications/190196SR/VOLUME/CHAPTERS/215.PDF>>. [Accessed 2004-12-10]
- Brown, K. M., B. A. Bekins, B. Clennell, D. Dewhurst, and G. Westbrook (1994), Heterogeneous hydrofracture development and accretionary fault dynamics, *Geology*, 22, 259-262.
- Brown, K.M., D. Saffer, and B.A. Bekins (2001), Smectite diagenesis, pore-water freshening, and fluid flow at the toe of the Nankai wedge, *Earth Planet. Sci. Lett.*, 194, 97-109.

- Brown, K. and G. K. Westbrook (1988), Mud diapirism and subcretion in the Barbados ridge accretionary complex: The role of fluid in accretionary processes, *Tectonics*, 7, 613-640.
- Bruckmann, W., K. Moran, and A. Mackillop (1997), Permeability and consolidation characteristics from Hole 949B, northern Barbados Ridge. *Proc. Ocean Drill. Program Sci. Results*, 156, 109-114.
- Bryant, W. R. (2002), Permeability of clays, silty-clays and clayey-silts, *Gulf Coast Assoc. Geol. Soci. Trans.*, 52, 1069-1077.
- Bryant, W. R., R. Bennett, and C. Katherman (1981), Shear strength, consolidation, porosity, and permeability of oceanic sediments. In Emiliani, C. (Ed.), *The Sea* (Vol. 7): New York (Wiley), 1555-1616.
- Bryant, W. R., W. Hottman, and P. Trabant (1975), Permeability of unconsolidated and consolidated marine sediments, Gulf of Mexico, *Marine Geotechnol.*, 1, 1-14.
- Byerlee, J. (1990), Friction, overpressure, and fault normal compression, *Geophys. Res. Lett.*, 17, 2109-2112.
- Byrne, T., A. Maltman, E. Stephenson, W. Soh and R. Knipe (1993), Deformation structures and fluid flow in the toe region of the Nankai accretionary prism, *Proc. Ocean Drill. Program Sci. Results*, 131, 83-95.
- Charlton, T. R. (1988), Tectonic erosion and accretion in steady-state trenches, *Tectonophysics*, 149, 233-23.
- COMPLEX (1999), Conference on Multiple Platform Exploration of the Ocean, Vancouver, British Columbia, edited by N. G. Pisias and M. L. Delaney, May.
- Coulbourn, W. T. (1982), Stratigraphy and structures of the Middle America Trench, Deep Sea Drilling Project Leg 67 transect off Guatemala, *Proc. Deep Sea Drill. Project Init. Rep.*, 67, 691-706.
- Cutillo, P.A., E. J. Screamton, and S. Ge (2003), Three-dimensional numerical simulation of fluid flow and heat transport within the Barbados accretionary complex, *J. Geophys. Res.*, 108, B12, 2555
- Dahlen, F. A. (1984), Noncohesive critical Coulomb wedges: an exact solution, *J. Geophys. Res.*, 89, 10,125-10,133.
- Davis, D. M., and D. M. Hussong (1984), Geothermal observations during Deep Sea Drilling Project Leg 78A, *Initial rep. Deep Sea Drill. Program*, 78A, 593-598.
- Davis, E. E., and R. D. Hyndman (1989), Accretion and recent deformation of sediment along the northern Cascadia subduction zone, *Geol. Soc. Am. Bull.*, 101, 1465-1480.

- Davis, D. M., J. Suppe, and F. A. Dahlen (1983), Mechanics of fold and thrust belts and accretionary wedges, *J. Geophys. Res.*, 88, 949-963.
- DeMets, C., R. G. Gordon, D. F. Argus, and S. Stein (1990), Current plate motions, *Geophys. J. Int.*, 101, 425-478.
- Domenico, P.A. and F. W. Schwartz (1998), Physical and Chemical Hydrogeology, 2nd ed., pp. 178-179, John Wiley and Sons, Inc., New York.
- Elliott, W. C., J. L. Aronson, G. Matisoff, and J. L. Gautier (1991), Kinetics of the smectite to illite transformation in the Denver Basin: Clay mineral, K-Ar data, and mathematical model results, *Am. Assoc. Pet. Geol. Bull.*, 75, 436-462.
- Ferguson, I.J., Westbrook, G.K., Langseth, M.G., Thomas, G.P. (1993), Heat flow and thermal models of the Barbados ridge accretionary complex, *J. Geophys. Res.*, 98, B3, 4121-4142
- Fetter, C. W. (1994), Applied Hydrogeology, Prentice Hall, New Jersey.
- Fisher, D., and T. Byrne (1987), Structural evolution of underthrusted sediments, Kodiak Islands, Alaska, *Tectonics*, 6, 775-793.
- Fisher, D., and T. Byrne (1990), The character and distribution of mineralized fractures in the Kodiak Formation, Alaska: implications for fluid flow in an underthrust sequence, *J. Geophys. Res.*, 95, 9069-9080.
- Fisher, A. T., and M. W. Hounslow (1990), Transient fluid flow through the toe of the Barbados accretionary complex: Constraints from Ocean Drilling Program Leg 110 heat flow studies and simple models, *J. Geophys. Res.*, 95, 8845-8858.
- Fisher, A. T., and G. Zwart (1996), Relation between permeability and effective stress along a plate boundary fault, Barbados accretionary complex, *Geology*, 24, 307-310.
- Fitts, T. G., and K. M. Brown (1999), Stress-induced smectite dehydration: ramifications for patterns of freshening and fluid expulsion in the N. Barbados accretionary wedge, *Earth Planet. Sci. Lett.*, 172, 179-197.
- Foucher, J. P., X. Le Pichon, S. Lallement, M. A. Hobart, P. Henry, M. Benedetti, G. K. Westbrook, and M. G. Langseth (1990), Heat flow, tectonics and fluid circulation at the toe of the Barbados Ridge accretionary prism, *J. Geophys. Res.*, 95, 8859-8867.
- Foucher, J. P., P. Henry, and F. Harmegnies (1997), Long-term observations of pressure and temperature in ODP Hole 948D, Barbados accretionary prism, *Proc. Ocean Drilling Program Sci. Results*, 156, 229-238.

- Fryer P., J. Pearce, L. Stokking, J. Ali, R. Arculus, D. Ballotti, M. Burke, G. Ciampo, J. Haggerty, R. Haston, D. Heling, M. Hobert, T. Ishii, L. Johnson, Y. Lagabrielle, H. Maekawa, M. Marlow, F. McCoy, G. Milner, M. Mottl, B. Murton, S. Phipps, C. Rigsby, K. Saboda, B. Stabell, S. Van Der Laan, and Y. Xu (1990), *Proceedings of the Ocean Drilling Program, Initial Reports*, 125. ODP Leg 125 Shipboard Scientific Party, College Station, TX.
- Gamage, K., B. Bekins, and E. Screamton (2005), Data report: Permeabilities of eastern equatorial Pacific and Peru margin sediments. In Jørgensen, B.B., D'Hondt, S.L., Miller, D.J., et al. (Eds.), *Proc. ODP, Sci. Results*, 201 [Online]. Available from World Wide Web: <http://www-odp.tamu.edu/publications/201_SR/103/103.htm>. [Accessed 2005-07-11]
- Gamage, K., and E. Screamton (2003), Data report: Permeabilities of Nankai accretionary prism sediments. In Mikada, H., Moore, G.F., Taira, A., Becker, K., Moore, J.C., and Klaus, A. (Eds.), *Proc. ODP, Sci. Results*, 190/196, 1-22 [Online]. Available from World Wide Web <<http://www-odp.tamu.edu/publications/190196SR/VOLUME/CHAPTERS/213.PDF>>. [Accessed 2004-06-10]
- Gamage, K., and E. Screamton (in press), Characterization of excess pore pressures at the toe of the Nankai accretionary complex, ocean drilling program sites 1173, 1174, and 808: results of one-dimensional modeling. *J. Geophys. Res.*
- Gieskes, J. M., T. Gamo, and M. Kastner (1993), Major and minor element geochemistry of interstitial waters of Site 808, Nankai Trough: An overview, *Proc. Ocean Drill. Program Sci. Results*, 131, 387-395.
- Gretener, P. E. (1976), Pore pressure: Fundamentals of general ramifications and implications for structural geology in AAPG Continuing Education Course Note Series #4, American Association of Petroleum Geologists, Tulsa, Okla., 87.
- Hampel, A. (2002), The migration history of the Nazca Ridge along the Peruvian active margin: a re-evaluation, *Earth Planet. Sci. Lett.* 203, 665-679.
- Hanshaw, B. B., and J. D. Bredehoeft (1968), On the maintenance of anomalous fluid pressures: II Source layer at depth, *Geol. Soc. Am. Bull.*, 79, 1107-1122.
- Hatcher, R. D. (1995), *Structural Geology*, pp. 224, Prentice Hall, New Jersey.
- Henry, P. (2000), Fluid flow at the toe of the Barbados accretionary wedge constrained by thermal, chemical, and hydrologic observations and models, *J. Geophys. Res.*, 105, 25,855-25,872.
- Henry, P., L. Jouniaux, E. Screamton, S. Hunze and D. Saffer (2003), Anisotropy of electrical conductivity record of initial strain at the toe of the Nankai accretionary wedge, *J. Geophys. Res.*, 108, doi:10.1029/2002JB002287.

- Henry, P., and C.-Y. Wang (1991), Modeling of fluid flow and pore pressure at the toe of Oregon and Barbados accretionary wedges, *J. Geophys. Res.*, 96, 20,109-20,130.
- Hovland, M. (1990), Do carbonate reefs form due to fluid seepage, *Terra Nova*, 2, 8-18.
- Hubbert, M. K., and W. W. Rubey, (1959), Role of fluid pressure in the mechanics of overthrust faulting, I, Mechanics of fluid-filled porous solids and its application to overthrust faulting, *Geol. Soc. Am. Bull.*, 70, 115-166.
- Jaeger, J. C., and N. G. W. Cook, (1969), Fundamentals of Rock Mechanics, pp. 87-91, Methuen, London.
- Kastner, M., and H. Elderfield, W. J. Jenkins, J. M. Gieskes and T. Gamo (1993), Geochemical and isotopic evidence for fluid flow in the western Nankai subduction zone, Japan, *Proc. Ocean Drill. Program Sci. Results*, 131, 397-413.
- Kastner, M., H. Elderfield, and J. B. Martin (1991), Fluids in convergent margins: What do we know about their composition, origin, role in diagenesis and importance for oceanic chemical fluxes, *Philos. Trans. R. Soc. London, Ser. A*, 335, 275-288.
- Kemerer, A., Screamton, E. (2001), Permeabilities of sediments from Woodlark Basin: implications for pore pressures. In Huchon, P., Taylor, B., Klaus, A. (Eds.), *Proc. ODP, Sci. Results*, 180, 1-14 [Online]. Available from World Wide Web<http://www-odp.tamu.edu/publications/180_SR/VOLUME/CHAPTERS/169.PDF>.
- Kirkup, L (2002), Data Analysis with Excel: An Introduction for Physical Scientists, pp. 213-360, Cambridge University Press.
- Knipe, R. J., S. M. Agar, and, D. J. Prior (1991), The microstructural evolution of fluid flow paths in semiolithified sediments from subduction complexes, *Philos. Trans. R. Soc. London, Ser. A*, 335, 261-273.
- Koltermann, C., and M. Gorelick (1995), Fractional packing model for hydraulic conductivity derived from sediment mixtures, *Water Resour. Res.*, 31(12), 3283-3297.
- Labaume, P., M. Kastner, A. Trave, and P. Henry (1997), Carbonate veins from the decollement zone at the toe of the N. Barbados accretionary prism: Microstructure, mineralogy, geochemistry, and relations with prism structures and fluid regime, *Proc. Ocean Drill. Program Sci. Results*, 156, 79-96.
- Langseth, M. G., and E. A. Silver (1996), The Nicoya convergent margin-A region of exceptionally low heat flow, *Geophys. Res. Lett.*, 23, 891-894.
- Langseth, M. G., G. K. Westbrook, and M. Hobart (1990), Contrasting geothermal regimes of the Barbados Ridge accretionary complex, *J. Geophys. Res.*, 95, 8829-8844.

- Le Pichon, X., T. Iiyama, J. Boulgue, J. Charvet, M. Faure, K. Kano, S. Lallement, H. Okada, C. Rangin, A. Taira, T. Urabe, and S. Uyeda (1987), Nankai Trough and Zenisu Ridge: a deep-sea submersible survey, *Earth Planet. Sci. Letters*, 83, 285-299.
- Le Pichon, X., and P. Henry (1992), Erosion and accretion along subduction zones: a model of evolution, *Koninklijke Nederlandse Akademie van Wetenschappen Proceedings*, 95, 297-310.
- Lide, D. R. (Ed.) (2000), Handbook of Chemistry and Physics, Chemical Rubber Publishing Company, pp. 12-13, Boca Raton, Florida.
- Lowe, J., P. Zacheo, H. Feldman (1964), Consolidation testing with backpressure, *J. Geotech. Eng. Div., Am. Soc. Civ. Eng.*, 90, 69-86.
- Maltman, A., T. Byrne, D. Karig and S. Lallement (1992), Structural geological evidence from ODP Leg 131 regarding fluid flow in the Nankai prism, Japan, *Earth Planet. Sci. Lett.*, 109, 463-468.
- Mascle, A., Moore, J. C., and Shipboard Scientific Party (1988), *Proc. ODP, Init. Repts. (Pt. A)*, 110: College Station, TX (Ocean Drilling Program).
- Masters, J. C., and H. Christian, (1990), Hydraulic conductivity of diatomaceous sediment from the Peru continental margin obtained during ODP Leg 112. In Suess, E., von Huene, R., et al., *Proc. Ocean Drill. Program Sci. Results*, 112, 633-638.
- McKiernan, A.W., and D. M. Saffer (in press), Permeability and consolidation properties of subducting sediments off Costa Rica, ODP Leg 205. In Morris, J.M., Villinger, H.W., and Klaus, A. (Eds.), *Proc. ODP, Sci. Results*, 205, 1-## [Online]. Available from World Wide Web: <http://www-odp.tamu.edu/publications/205_SR/VOLUME/CHAPTERS/203.PDF>. [Accessed 2005-05-30].
- Meyer, A. and A. Fisher (1997), *Proc. Ocean Drill. Program Sci. Results*, 156, 337-341.
- Moore, J. C. (1989), Tectonics and hydrogeology of accretionary prisms: Role of the decollement horizon, *J. Struct. Geol.*, 11, 95-106.
- Moore, J. C., B. Biju-Duval and team (1982), Offscraping and underthrusting of sediment at the deformation front of the Barbados Ridge: Deep Sea Drilling Project Leg 78A, *Geol. Soc. Am. Bull.*, 93, 1065-1077.
- Moore, J. C., A. Klaus, and Shipboard Scientific Party (1998), *Proceedings of the Ocean Drilling Program, Initial Reports*, vol. 171A, Ocean Drill. Program, College Station, Tex.

- Moore, J.C., G. F. Moore, G. R. Cochrane, and H. J. Tobin (1995), Negative-polarity seismic reflections along faults of the Oregon accretionary prism: Indicators of overpressuring, *J. Geophys. Res.*, 100, 12,895-12,906.
- Moore, J.C. and Saffer, D. (2001), Updip limit of the seismogenic zone beneath the accretionary prism of southwest Japan: An effect of diagenetic to low-grade metamorphic processes and increasing effective stress, *Geology*, 29, 183-186.
- Moore, J. C. and E. Silver (2004), Fluid flow in accreting and eroding convergent margins, In K. Becker et al. (Eds.), *Achievements and Opportunities of Scientific Ocean Drilling, Joides Journal*, 28, 91-96.
- Moore, G.F., A. Taira, N. L. Bangs, S. Kuramoto, T. H. Shipley, C. M. Alex, S. S. Gulick, D. J. Hills, T. Ike, S. Ito, S. C. Leslie, A. J. McCutcheon, K. Mochizuki, S. Morita, Y. Nakamura, J. O. Park, B. L. Taylor, G. Toyama, H. Yagi, and Z. Zhao (2001), Data report: Structural setting of the Leg 190 Muroto transect. In Moore, G.F., Taira, A., Klaus, A., et al., *Proc. ODP, Init. Repts.*, 190 [Online]. Available from World Wide Web: <http://www-odp.tamu.edu/publications/190_IR/chap_02/chap_02.htm>. [Accessed 2005-06-15]
- Moore, J. C., and P. Vrolijk (1992), Fluids in accretionary prisms, *Rev. Geophys.*, 30, 113-135.
- Muller, R. D. and W. H. F. Smith (1993), Deformation of the oceanic crust between the north American and South American plates, *J. Geophys. Res.*, 98, 8275-8291.
- Neuzil, C. E. (1986), Groundwater flow in low-permeability environments, *Water Resour. Res.*, 22, 1163-1195.
- Neuzil, C. E. (1994), How permeable are clays and shale?, *Water Resour. Res.*, 30, 145-150.
- Olsen, H. W., R. W. Nichols and, T. L. Rice (1985), Low gradient permeability measurements in a triaxial system, *Geotechnique*, 35, 145-157.
- Peacock, S. M. (1990), Fluid processes in subduction zones, *Science*, 248, 329-337.
- Perry, E., and J. Hower (1970), Burial diagenesis in Gulf Coast pelitic sediments, *Clays Clay Miner.*, 18, 165-177.
- Price, R. (1988), The mechanical paradox of large overthrusts, *Geol. Soc. Am. Bull.*, 100, 1898-1908.
- Robertson, E. C. (1967), Laboratory consolidation of carbonate sediments. In Richards, A.F. (Ed.), *Marine Geotechnique*: Urbana (Univ. Illinois Press), 118-127.

- Saffer, D. M. (2003), Pore pressure development and progressive dewatering in underthrust sediments at the Costa Rican subduction margin: comparison with northern Barbados and Nanaki, *J. Geophys. Res.*, 108, doi:10.1029/2002JB001787.
- Saffer, D., and B. A. Bekins (1998), Episodic fluid flow in the Nankai accretionary complex: Timescale, geochemistry, flow rates and fluid budget, *J. Geophys. Res.*, 103, 30,351-30,370.
- Saffer, D., and B. A. Bekins (1999), Fluid budgets at convergent plate margins: Implications for the extent and duration of fault-zone dilation, *Geology*, 27, 1095-1098.
- Saffer, D., and B. A. Bekins (2002), Hydrologic controls on the morphology and mechanics of accretionary wedges, *Geology*, 30(3), 271-274.
- Saffer, D., and A. McKiernan (2005), Permeability of underthrust sediments at the Costa Rican subduction zone: Scale dependence and implications for dewatering, *Geophys. Res. Lett.*, 32, doi:10.1029/2004GL021388.
- Saffer, D., E. Silver, A. Fisher, H. Tobin, and K. Moran, (2000), Inferred pore pressures at the Costa Rica subduction zone: implications for dewatering processes. *Earth Planet. Sci. Lett.*, 177, 193-207.
- Scholz, C. H. (1998), Earthquakes and friction laws, *Nature*, 391, 37-42.
- Screaton, E. J., B. Carson, and G. P. Lennon (1995), Hydrogeological properties of a thrust fault within the Oregon accretionary prism: *J. Geophys. Res.*, 100, 20,025-20,035.
- Screaton, E. J., A. T. Fisher, B. Carson, and K. Becker (1997), Barbados Ridge hydrogeologic tests: Implications for fluid migration along an active decollement, *Geology*, 25, 239-242.
- Screaton, E. J., and S. Ge (1997), An assessment of along-strike fluid and heat transport within the Barbados ridge accretionary complex: Results of preliminary modeling, *Geophys. Res. Lett.*, 24, 3085-3088.
- Screaton, E. J., and S. Ge (2000), Anomalously high porosity in the proto-decollement zone of the Barbados accretionary complex: Do they indicate overpressures?, *Geophys. Res. Lett.*, 27, 1993-1996.
- Screaton, E. J., T. Hays, K. Gamage and J. Martin (in press), Data report: Permeabilities of Costa Rica subduction zone sediments. In Morris, J.M., Villinger, H.W., and Klaus, A. (Eds.), *Proc. ODP, Sci. Results*, 205, 1-## [Online]. Available from World Wide Web: <http://www-odp.tamu.edu/publications/205_SR/VOLUME/CHAPTERS/203.PDF>. [Accessed 2005-05-30].

- Screaton, E. J., D. Saffer, P. Henry, S. Hunze and Leg 190 Shipboard Scientific Party (2002), Porosity loss within the underthrust sediments of the Nankai accretionary complex: Implications for overpressures, *Geology*, 30, 19-22.
- Seno, T., S. Stein, and A. E. Gripp (1993), A model for the motion of the Philippine Sea Plate consistent with NUVEL-1 and geological data, *J. Geophys. Res.*, 98, 17,941-17, 948.
- Shi, Y., and C.-Y. Wang (1985), Pore pressure generation in front of the Barbados Ridge Complex, *Geophys. Res. Lett.*, 12, 773-776.
- Shi, Y., and C.-Y. Wang (1988), Generation of high pore pressures in accretionary prisms: Inferences from the Barbados subduction complex, *J. Geophys. Res.*, 93, 8893-8910.
- Shi, Y., and C.-Y. Wang (1994), Models study of advective heat flow associated with compaction and dehydration in accretionary prisms, *J. Geophys. Res.*, 99, 9319-9325.
- Shipboard Scientific Party (1991), Site 808, In Taira, A., I. Hill, J. V. Firth, *Initial Reports, Ocean Drilling Program Leg 131*, College Station, Texas, Ocean Drilling Program, pp. 71-269.
- Shipboard Scientific Party (1998), Introduction to logging-while-drilling investigations of faulting, fluid flow, and seismic images of the northern Barbados subduction zone. In Moore, J.C., Klaus, A., et al., *Proc. ODP, Init. Repts.*, 171A: College Station, TX (Ocean Drilling Program), 5-10.
- Shipboard Scientific Party (2001), Leg 190 Preliminary Report: Deformation and fluid flow processes in the Nankai Trough accretionary prism, [Online] <http://www.odp.tamu.edu/publications/prelim/190_prel/190PREL.PDF>.
- Shipboard Scientific Party, (2003), Leg 201 summary. In D'Hondt, S.L., Jørgensen, B.B., Miller, D.J., et al., *Proc. ODP Init. Repts.*, 201 [Online]. Available from World Wide Web: http://www-odp.tamu.edu/publications/201_IR/chap_01/chap_01.htm. [Accessed 2004-12-15]
- Shipley, T. H., G. F. Moore, N. L. Bangs, J. C. Moore, and P. L. Stoffa (1994), Seismically inferred dilatancy distribution, northern Barbados Ridge decollement: Implications for fluid migration and fault strength, *Geology*, 22, 411-414.
- Shipley, T.H., Y. Ogawa, P. Blum, and J. M. Bahr (Eds.), (1997), *Proc. ODP, Sci. Results*, 156 [Online]. Available from World Wide Web: http://www-odp.tamu.edu/publications/156_SR/156TOC.HTM. [Accessed 2004-12-15]

- Sibuet, M., A. Fiala, J. P. Foucher, and S. Otha (1990), Spatial distribution of clams colonies at the toe of the Nanakai accretionary prism near 138° E, International Conference of Fluids in Subduction Zones, Abstracts Volume, Center National de la Recherche Scientifique, Paris.
- Silver, E.A., G. Kimura, P. Blum, and T. H. Shipley (Eds.), (2000), *Proc. ODP, Sci. Results*, 170 [Online]. Available from World Wide Web: http://www-odp.tamu.edu/publications/170_SR/170sr.htm. [Accessed 2005-02-15]
- Spivack, A. J., M. Kastner and B. Ransom (2002), Elemental and isotopic chloride geochemistry and fluid flow in the Nankai Trough, *Geophys. Res. Lett.*, 29, 10.1029/2001GL014122.
- Stauffer, P. and B. A. Bekins (2001), Modeling consolidation and dewatering near the toe of the northern Barbados accretionary complex, *J. Geophys. Res.*, 106, 6369-6383.
- Steurer, J. F., and M. Underwood (2003), Data report: The relation between physical properties and grain-size variations in hemipelagic sediments from Nankai Trough. In Mikada, H., Moore, G.F., Taira, A., Becker, K., Moore, J.C., and Klaus, A. (Eds.), *Proc. ODP, Sci. Results*, 190/196, 1-25 [Online]. Available from World Wide Web<<http://www-odp.tamu.edu/publications/190196SR/VOLUME/CHAPTERS/210.PDF>>. [Accessed 2004-12-10]
- Stow, D. A. V., and D. J. W. Piper (1984), Deep-water fine-grained sediments: Facies models, in Fine-grained sediments: Deepwater processes and facies, edited by D. A. V. Stow and D. J. W. Piper, pp. 611-646, The geological Society, Blackwell, Oxford.
- Taylor, E., and A. Fisher (1993), Sediment permeability at the Nankai accretionary prism, Site 808, *Proc. Ocean Drill. Program Sci. Results*, 131, 235-245.
- Taylor, E., and J. Leonard (1990), Sediment consolidation and permeability at the Barbados forearc, *In Proc. Ocean Drill. Program Sci. Results*, 110, 289-308.
- Terzaghi, K and R. B. Peck (1940), Soil Mechanics in Engineering Practice, 2nd ed. John Wiley and Sons, New York, 729.
- Ujiie, K., T. Hisamitsu and A. Taira (2003), Deformation and fluid pressure variation during initiation and evolution of the plate boundary decollement zone in the Nankai accretionary prism, *J. Geophys. Res.*, 108, doi:10.1029/2002JB002314.
- Underwood, M. B., and X. Deng (1997), Clay mineralogy and clay geochemistry in the vicinity of the decollement zone, northern Barbados ridge, *Proc. Ocean Drill. Program, Sci. Results*, 156, 3-30.

- Underwood, M. B., K. Pickering, J. M. Gieskes, M. Kastner, and R. Orr (1993), Sediment geochemistry, clay mineralogy and diagenesis: A synthesis of data from Leg 131, Nankai Trough, *Proc. Ocean Drill. Program Sci. Results*, 131, 343-363.
- Von Huene, R., and D. W. Scholl (1991), Observations at convergent margins concerning sediment subduction, subduction erosion, and the growth of continental crust, *Rev. Geophys.*, 29, 279-316.
- Voss, C. I. (1984), A finite element simulation model for saturated-unsaturated, fluid density-dependent groundwater flow with energy transport or chemically-reactive single species solute transport, *U.S. Geol. Surv. Water Resour. Invest.*, 84-4369.
- Vrolijk, P. J. (1987), Tectonically-driven fluid flow in the Kodiak accretionary complex, Alaska, *Geology*, 15, 466-469.
- Vrolijk, P. J., G. Myers, and J. C. Moore ((1988), Warm fluid migration along tectonic mélanges in the Kodiak accretionary complex, Alaska, *J. Geophys. Res.*, 93, 10,313-10,324.
- Westbrook, G. K., J. W. Ladd, P. Buhl, N. Bangs, and G. J. Tiley (1988), Cross section of an accretionary wedge: Barbados Ridge Complex, *Geology*, 16, 631-635.
- Westbrook, G. K. and M. J. Smith (1983), Long decollement and mud volcanoes; evidence from the Barbados Ridge complex for the role of high pore-fluid pressure in the development of an accretionary complex, *Geology*, 11, 279-283.
- Yeung, K., C. Chakrabarty, and X. Zhang (1993), An approximate analytical study of aquifers with pressure-sensitive formation permeability: *Water Resour. Res.*, 29, 3495-3501.
- Zwart, G., W. Bruckmann, K. Moran, A. MacKillop, A. Maltman, A. Bolton, P. Vrolijk, T. Miller, M. Gooch and A. Fisher (1997), Evaluation of hydrogeologic properties of the Barbados accretionary prism: a synthesis of Leg 156 results. In Shipley, T. H., Ogawa, Y., Blum, P., and Bahr, J.M. (Eds.), *Proc. Ocean Drill. Program Sci. Results* 156, 303-310.

BIOGRAPHICAL SKETCH

Kusali Gamage was born in April 27, 1974, in Colombo, Sri Lanka. She earned her Bachelor of Science (1997) and Master of Science (1999) degrees from Bowling Green State University of Ohio. She continued her education at the University of Florida, where she received her PhD in December of 2005.